2015

SURFO Technical Report No. 15-01

SURFO

Papers from the

SUMMER UNDERGRADUATE RESEARCH FELLOWSHIP PROGRAM IN OCEANOGRAPHY

at

THE UNIVERSITY OF RHODE ISLAND GRADUATE SCHOOL OF OCEANOGRAPHY

Narragansett, Rhode Island

June – August 2015

This program was supported by The National Science Foundation REU Program (OCE-1460819)

GSO Technical Report No. 15-01

TABLE OF CONTENTS

2015 PROGRAM PARTICIPANTS
SUMMER UNDERGRADUATE RESEARCH FELLOWSHIP IN OCEANOGRAPHY

FELLOWS

Hyunyung Boo, McGill University (Biology)
Keaton Brenneman, Rutgers University (Physical Oceanography)
Blake Cross, Colorado School of Mines (Geophysical Engineering)
Julia Hogan, University of South Carolina (Marine Science)
Connor Jones, State University of New York at Binghamton (Biology)
Brittany Kerr, Adrian College (Chemistry)
Joshua Port, Tufts University (Physics)
Kyle C. Rennell, Lock Haven University of Pennsylvania (Engineering Geology)
Felicia Rodier, Salem State University (Marine Biology)
Nicole Statler, University of Portland (Mathematics)
Emma Thomas, University of Massachusetts, Amherst (Physics / Geology)
Amanda Van Buskirk, Monmouth University (Mathematics / Statistics)

ADVISORS

Amanda Babson
David Borkman
Jeremy Collie
Jason Dahl
Kathleen Donohue
Tetsu Hara
Rainer Lohman
Melissa Omand
Anton Post
Rebecca Robinson
Thomas Rossby
Theodore Smayda
Matt Wei

PROGRAM ASSISTANTS

Amin Mihvechi, URI Graduate Student Liaison (Ocan Engineering)
Kim Carey, Program Coordinator

PREFACE

This report presents the papers written by the 12 participants in the ten weeks of the 2015 Summer Undergraduate Research Fellowships in Oceanography (SURFO) program at the Graduate School of Oceanography (GSO), University of Rhode Island (URI). The papers are introduced in alphabetical order of the participants. This past summer represented the 31st year in which the program has been coordinated and extended through the several disciplines in oceanography and ocean engineering at URI's Narragansett Bay Campus. The 2015 activities will continue excellence beyond the official duration of the program with presentations at national and regional conferences: two projects planned for presentation at the ASLO 2016 meeting, another one at a regional fisheries meeting, one at an engineering meeting, and one at a coastal research meeting. One manuscript is nearly ready for a peer-reviewed publication.

The 2015 SURFO participants are grateful to the National Science Foundation REU program for their support through grant OCE-1460819.

The SURFO program would like to thank advisors and graduate student mentors at URI who contributed to the program's success including those who gave SURFO seminar presentations and/or participated in educational activities. In addition, our thanks go to Kim Carey for her timely assistance covering administrative, financial, and recruitment tasks. Finally, we would like to acknowledge Amin Mihvechi who served as a graduate student coordinator for the program.

Lucie Maranda October 2015
Kathleen A. Donohue
David C. Smith
SURFO Site Directors

Developing a Novel Method for Marine Particle Imaging In Situ Using Holographic Microscopy

Hyunyung Boo, Melissa Omand
Graduate School of Oceanography, University of Rhode Island, Narragansett, RI 02882

Abstract

Plankton form the base of the ocean food web and are found in diverse shapes and sizes. These various morphologies reflect different adaptations for survival and affect their interactions with the environment. At URI's Graduate School of Oceanography, an ongoing 60-year survey of plankton in Narragansett Bay represents a large and comprehensive data set. As part of the survey, we imaged particles ranging in size from 10 to 500 μm with an in situ holographic microscope. To evaluate the microscope's capabilities for plankton identification, the camera was set in-line with a FlowCam® particle analyzer to image laboratory cultures of several dinoflagellate species. Comparison between the species identified from the phytoplankton collection and FlowCam® to those seen with holography can inform us about the future utility of the microscope. However, because the holographic microscope records at a rate up to 5 gigabytes per minute, a majority of this project was devoted to addressing the significant data management challenges. To make these data accessible, several steps in the analysis were automated, such as the saving of reconstructed images, background subtraction, and the selection of a frame of interest in each hologram. This function's performance was validated against results from a manual selection. We conclude that despite some challenges for automation and image quality, the holographic microscope's large imaging volume (2 cm^3) and ability to record video in situ will bring a new perspective to studying microplankton and detrital particles.

Marine phytoplankton are responsible for a significant amount of the global net primary production (NPP) amounting to $50x10^{15}$ grams of carbon per year, rivaling the NPP on land (Chavez, 2011). This primary production feeds the bulk of the marine food web and produces significant amounts of oxygen. On the other hand, sudden blooms of phytoplankton can cause regions of hypoxia and fish kills while certain bloom forming species are toxic to humans and other organisms. Because of the impact of phytoplankton on the fisheries industry as well as potentially being hazardous to human health, it is in our interest to study the behaviors and life cycles of phytoplankton.

The structure of phytoplankton results from their interactions with a fluid environment and their need to acquire light and nutrients while avoiding predation and sinking. Because phytoplankton have limited motility, the fluid flow around them influences their distribution in the water column. For example, the interplay between cell motility and vertical shear causes phenomena called thin layers, where phytoplankton biomass is concentrated in a layer of ocean a few centimeters to a meter thick (Durham et al., 2009). To study these interactions, observations should be made of phytoplankton in situ in the context of ocean circulation and turbulence.

Ongoing efforts such as a phytoplankton survey in Narragansett Bay conducted by the Graduate School of Oceanography at the

University of Rhode Island have been studying the local plankton population since 1956. One of the parameters measured is chlorophyll fluorescence, an indirect proxy for phytoplankton productivity and biomass. However, direct study and identification of plankton in the field involves time intensive tasks such as preparing samples and observing them under a microscope in the laboratory.

A submersible digital in-line holographic microscope (DIHM) is being developed to make phytoplankton observations in the field. Due to the properties of holography, this microscope has a much greater depth of field than achieved with optical microscopy and can image a larger sample volume with high resolution (Jericho et al., 2006). The DIHM is able to resolve particles from 10 to 2000 μm and has the potential to be useful in studying the movement of microorganisms in situ as well as assist in characterizing plankton community structure. DIHM is ideal to study fragile particles such as marine snow which are often destroyed by net tows or Niskin bottle collection. It can also be used to image fecal pellets and measure their sinking rates (Bochdansky et al., 2013).

Before the start of this project, a test recording of 3000 holograms was taken with the DIHM at Dingle Dock in Halifax, Nova Scotia which were used to develop parts of this methodology. Then, as part of the weekly phytoplankton survey, the microscope was deployed on June 30, July 13, July 20, and July 27. The sampling site was located at Fox Island (41◦34.5' N, 71◦24.3' W) in Narragansett Bay, with a depth of 6-8m at low tide. The microscope was lowered until just submerged, with the camera opening at about 50-cm depth. Samples were recorded for intervals of 2-3 minutes with pulse duration of 1 to 10 μs. Most holograms used were recorded with pulse duration of 3 or 4 μm. A speed of 16 frames per second was used throughout.

At a rate of 16 frames per second, the DIHM will record over a terabyte of raw hologram images per day. Although samples were recorded only for 2-3 minutes for the purpose of this project, the goal is to eventually deploy the DIHM autonomously as part of an AUV or CTD rosette. Therefore, part or all of the image processing must be automated to make the data useful.

This report describes and assesses the steps developed to (a) remotely carry out hologram reconstruction, (b) subtract an appropriate background to create a contrast hologram, (c) use skewness as a metric for finding in-focus images, and (d) test the use of the DIHM in the laboratory.

MATERIALS

The submersible digital holographic microscope used was the model produced by the company 4-Deep with a depth rating of up to 6000 m. It was deployed on the R/V Cap'n Bert using a 100-m cable. The DIHM software, named Octopus, was installed and run on a Lenovo Y50 laptop with 8GB RAM and a NVIDIA GeForce GTX 960M graphics card.

For laboratory studies, a flow-through chamber attachment from 4-Deep was used to image laboratory cultures of *Akashiwo sanguinea*, *Gyrodinium spirale*, *Heterocapsa triquetra*, *Oxyrrhis marina, Isochrysis galbana*, and *Prorocentrum micans*.

The code was developed in Matlab R2014b using the image processing and instrument control toolboxes.

PROCEDURES AND ASSESSMENT

Establishing a remote connection – The software Octopus performs reconstructions when a hologram, reconstruction location,

and optionally a background image are supplied. A Matlab script to remotely connect to and control Octopus was developed to automate this process. The connection is established through a TCP/IP server socket which allows commands to be sent remotely to Octopus. Matlab must be open to the directory containing the saved raw holograms and the hologram of interest and background are remotely set using their relative path names. Octopus must also be open in the correct directory of holograms and the lower right corner must display ”Hologram: -- Background: --” before the script is run. The options for including scale bars in Octopus should be unchecked.

Commands to Octopus behave asynchronously and a necessary pause of at least 0.8 s between the command RECONSTRUCTION POSITION, which sets the reconstruction position, and RECONSTRUCT HOLOGRAM, which performs the reconstruction sets a lower bound on run time. Before running the remote command, averaged backgrounds are first saved at the beginning of the same directory as the hologram bitmaps.

The script remotely processes a single directory of raw holograms. Each raw hologram is reconstructed in intervals of 215 μm from 500 to 2200 μm, resulting in 100 reconstructed images per hologram which are saved in a unique directory. Saving in intervals of 21 μm was tested for one set of 30 holograms to compare whether this higher resolution produces better in-focus reconstructed images than an interval of 215 μm.

Background picking problem – Procedure – A background is subtracted from the hologram to create what is called a contrast hologram. This removes persistent noise such as what is caused by a dirty camera lens and also reduces the uneven lighting caused by the spherical laser. The two default options available in Octopus are subtracting pairs of holograms and setting an arbitrary background to use for an entire directory.

The pair-by-pair method subtracts consecutive pairs of holograms from each other during reconstruction. For choosing an arbitrary background, a hologram can manually be selected from the directory. When reconstructing remotely, the arbitrary background can be specified in the Matlab script using its filename. Using a background which was 3, 200, and 3000 holograms away from the hologram of interest, examples of the results from arbitrary subtraction were saved.

Another option for a background can be created in Matlab by averaging a set of holograms together to create a smooth background. When Octopus records raw holograms from the 4-Deep microscope, they are each saved with a customized color map. The color maps vary in size and value from hologram to hologram and must be standardized before their corresponding holograms are averaged. The union of the color maps of all the holograms to be averaged is found and set as a new standard color map. Then, each of the original 2060-by-2056 holograms are remapped from their own color map to the new standard color map, pixel by pixel. The backgrounds are then averaged and saved as a bitmap file.

To test background saving and reconstruction on a sequence of 240 holograms, the directory was divided up into 6 sections of 40 holograms. In each section, the middle 10 holograms were averaged to form the background and this background was subtracted from each hologram in the section of 40.

To test the effect of the location of an averaged set of holograms on the reconstruction, the first 120 holograms from this directory were averaged in sets of 10. The images resulting from reconstruction

with a background averaged from a set containing the hologram of interest versus a background averaged from a set 100 holograms away were compared.

Background picking problem – Assessment – When using Octopus, the quickest way to look through the contents of a hologram directory by hand is to use the pair-by-pair feature. Octopus reconstructs the holograms two by two, using two consecutive holograms as a hologram of interest and a background. The disadvantage is that ghost images are produced when particles move too slowly to completely leave the sampling volume before the next hologram is captured. This creates a doubling effect in the reconstructed hologram, where each particle appears twice (Fig. 1a).

It is possible to make an educated selection by hand that will remove the most noise without creating ghost images. The optimal choice is to pick the background that is as near as possible to the hologram which does not also contain the particle of interest. However, when looking through a directory which contains 500 holograms per minute of recording, it is not feasible to carry out this careful manual selection for every reconstruction. When using the remote commands to specify a background hologram to be used, the selection becomes arbitrary because there is no easy way for software to tell whether the chosen background is a good fit for the hologram reconstruction. An arbitrarily chosen background might, for example, contain a large particle which obscures other particles in reconstructed holograms and introduces noise. When selecting an arbitrary background, the reconstruction using a background 3 frames (Fig. 1b) away from the hologram of interest looks similar to that produced using a background 210 frames (Fig. 1c) away. However, using a background 3000 frames away results in a significantly noisier reconstruction (Fig. 1d).

To reduce the contribution of any one arbitrary background hologram on the reconstruction, a set of holograms are averaged together to a smooth background.

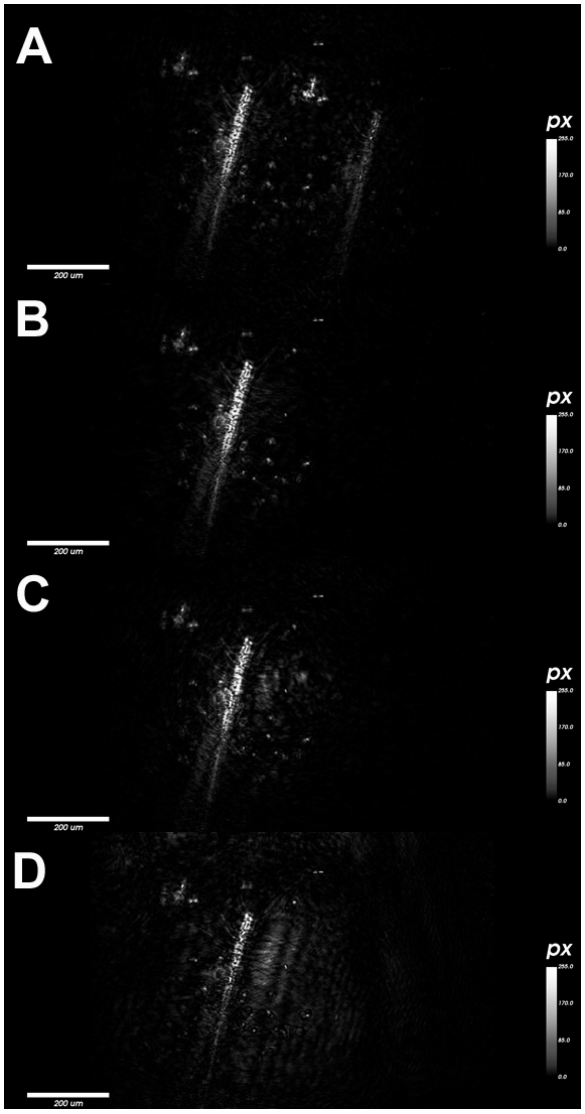

Fig. 1: (a) Hologram reconstruction pair by pair showing a ghost image of the diatom chain. (b) Reconstruction with background chosen 3 holograms away contains the least noise. (c) Reconstruction with background chosen 200 holograms away shows more noise. (d) Reconstruction with background chosen 3000 holograms away contains the most noise. An interference pattern is visible to the right of the diatom chain.

This choice appears to be optimal because it preserves the persistent noise characteristics of the holograms in that location, while any incidental particles are insignificant. A background averaged from a set containing the hologram of interest can even be used. In contrast, if the same hologram is used as both the background and hologram of interest without averaging, the pixel-by-pixel subtraction results in an empty black image.

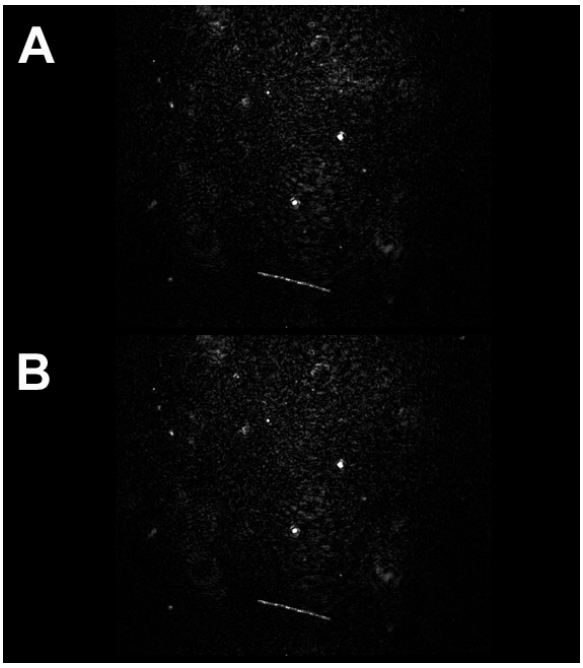

Fig. 2: (a) Hologram reconstructed with background averaged from a set of 10 holograms containing hologram of interest. (b) Reconstruction with background averaged from a set of 10 holograms 100 frames away. The two reconstructions are similar and one averaged background could be used to reconstruct 200 holograms.

The effect of the choice of the set of 10 holograms averaged for the background on the hologram reconstruction was evaluated. The difference between subtraction with an averaged background of a set of 10 holograms where one hologram is the hologram of interest (Fig. 2a), vs. subtraction with a background consisting of a set 100 holograms away from the hologram of interest (Fig. 2b) appears minimal. The reconstruction using the background 100 holograms away produces a slightly noisier image but reduces run-time by tenfold.

Despite the challenges to selecting an appropriate background, subtraction is necessary because it evens out the distribution of light in the hologram and makes particles at the edges of the hologram visible. In Fig. 3, a rod like colony of diatoms that is present on the edges of the hologram which is visible in Fig. 2 cannot be seen without background subtraction.

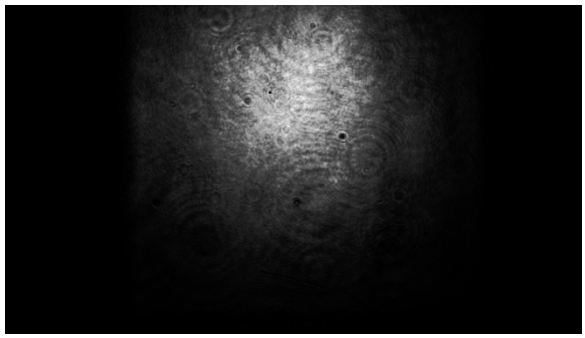

Fig. 3: Hologram reconstructed at the same location as Fig. 2a and 2b but without background subtraction. Rod-like diatom chain is not visible without subtraction because of uneven illumination.

Using skewness as a measure of focus – Procedure and assessment – To determine which of the reconstructed images of a hologram are in focus and therefore of interest, the skewness of pixel intensity distribution for each reconstruction position of a hologram was analyzed. A script was written which calculates the skewness value for each image in a hologram's reconstructed directory and outputs the image with the highest skewness. Using a function called findpeaks, which finds local maxima, the top 3 or 4 peaks in skewness are found and the corresponding reconstruction images and positions output.

Skewness was used as a measure of whether or not a reconstructed image may be in focus. Focused images appear crisper and brighter and less in-focus images are blurry with lower intensity brightness. This leads to an in-focus, distinct frame having a more skewed distribution of pixel intensities than its less in-focus neighbors, because it contains more of the brightest pixel values. Local maxima in skewness should also represent an object in focus if there are multiple particles of interest represented in a hologram (Fig. 4).

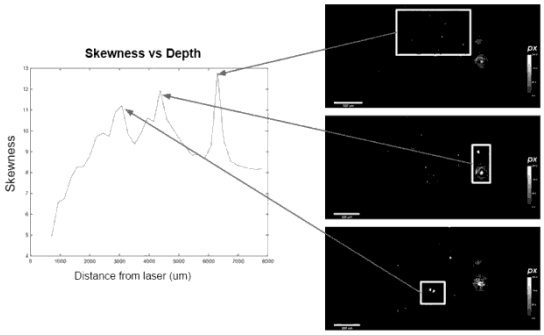

Fig. 4: Example of skewness versus reconstruction position (distance from laser). The locations of the three peaks in skewness correspond to reconstruction locations where different particles come into focus (boxes).

Although an interval of 21 µm was used in one trial to test whether a better-focused image was produced, 215 µm was sufficient for our purposes. The range of reconstruction locations where a particle comes into focus is generally on the order of 215 µm.

240 holograms recorded from the R/V Cap'n Bert in Narraganset Bay were reconstructed and saved in intervals of 215 µm using background averaging method with chunks of 40 described above. The findpeaks function was used to output 3 peaks in skewness, and 3 manually selected reconstructed frames of interest were independently found.

A subsample of 30 holograms was chosen to represent a mix of distinct zooplankton and diatom colonies as well as noisier holograms. For the subsample, the location of the highest peak in skewness was plotted against the closest manually selected location (Fig. 5). Excluding the outlier 31-510, the data fitted the line $y = 1.015x - 0.1315$ with an R^2 value of 0.979 and $p < 0.0001$.

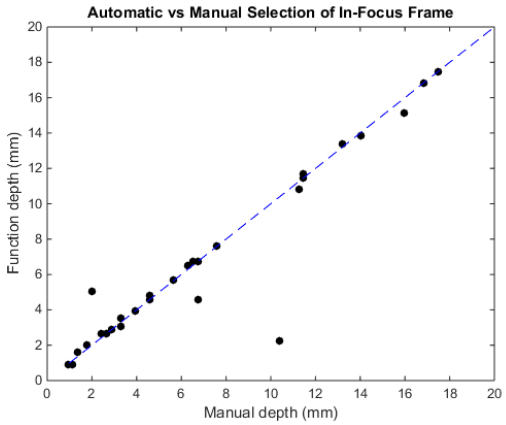

Fig. 5: The highest peak in skewness is plotted against the closest corresponding manually selected location.

Out of the same subsample of 30, all peaks in skewness which appeared significant were located manually for each hologram. All reconstructed frames which appeared significant were also independently found (Table 1). Each hologram has 1 to 5 "significant peaks" in skewness and the location of the manually selected peaks and the reconstruction locations of images in focus agree for all except in three instances.

Holograms 29-986, 30-924, and 31-510 demonstrate significant peaks in skewness which do not correspond to an in-focus reconstruction at that depth. Out of 58 peaks selected in the subsample of 30 holograms, 55 represented the location of an in-focus reconstruction. Conversely, 56 images were chosen manually to be in focus. 55 of these correspond to the peaks in skewness and the one which was not represented (7 in skewness) was an in-focus reconstruction of a small "stick" among scattered particles.

Table 1: Comparison of reconstruction locations found manually by looking at peaks of skewness to reconstruction positions where particles of interest were in focus. The Findpeaks function does not always agree with the manual selection of peaks.

Hologram ID	Skewness peak location	Manually selected location
27-799	3510	3295
28-112	2650, 8025	2435, 8025
28-299	6520	6305
28-424	4155, 6090	3940, 5875
29-799	4585	6735
29-986	2650, 7165*	2650
30-362	3080, 16410	3295, 16840
30-924	3940*, 6735	6735
31-510	2220*, 11035	10605
31-962	2650, 4800, 17270	2650, 4585, 17270
32-404	1575, 2865, 14045	1575, 2865, 14045
32-561	2865, 15550	2865, 15550
32-703	3725, 7380, 10820	3510, 7165, 11250, 14690**
33-205	930	930
34-060	1145, 7165	1145, 7165
34-156	6735	6520
34-443	2435, 4585, 17485	2435, 4585, 17485
35-068	1575, 6305, 15120	1145, 5875, 15980
35-523	2865	2865
35-889	16840	16840
36-301	1575	1575
36-685	2005, 5015	2005, 5015
37-487	2005	2005
38-303	4800	4800
39-037	7595	7595
40-524	2425, 4800, 11135, 11680	2425, 4585, 11135, 11465
42-277	13400	13400
42-985	3080, 3940	3080, 3940
43-801	2640, 4585	2640, 4585
44-565	2435, 5230, 8025, 9100, 11465	2435, 5230, 8025, 9100, 11465

* Position of a peak in skewness without an in-focus reconstruction

** Reconstructed image chosen manually to be in focus not represented by a peak in skewness

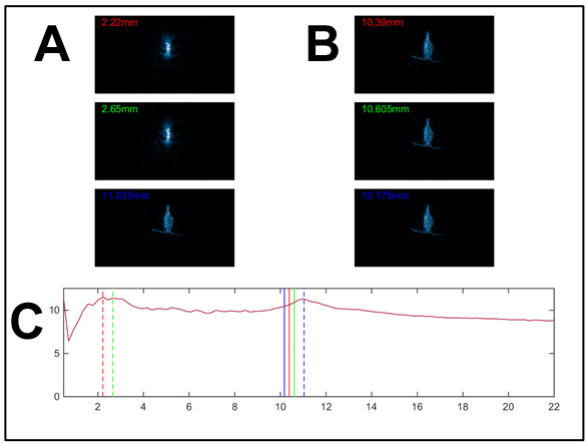

Fig. 6: (a) Reconstructions at locations where the Findpeaks function selects for top-3 skewness peaks. The top two "in-focus" reconstructions indicated by skewness are the brightest images but do not show the copepod. Although the copepod is distinct and has sharp edges, it is dimmer than the first two reconstructions chosen. (b) Manual selection for top-3 in-focus images in hologram directory. (c) Plot of skewness versus reconstruction location. Dotted lines indicate where each of the reconstructed images was positioned; solid lines indicate manually selected reconstructions.

From this analysis, significant peaks in skewness are a good indicator for which reconstructed images in a hologram contain particles in focus. Hologram 31-510, one of the three holograms containing skewness peaks which did not represent an object in focus, contains a single large particle - a copepod (Fig. 6). The particle is distinct and has sharp edges but is comprised of pixels with a relatively low intensity. The skewness peak represents this particle in focus at the depth 11035, but shows a larger peak at 2220, where the hologram is reconstructed into a smaller dot of bright pixels. One of the disadvantages of the skewness method is that particles distinct to the eye but not bright may be looked over. Fig. 7, a reconstructed image of a chain of *Chaetoceros* sp. from Halifax, Nova Scotia

demonstrates another case of this phenomenon. In this example, the reconstruction location is not represented by a peak in skewness.

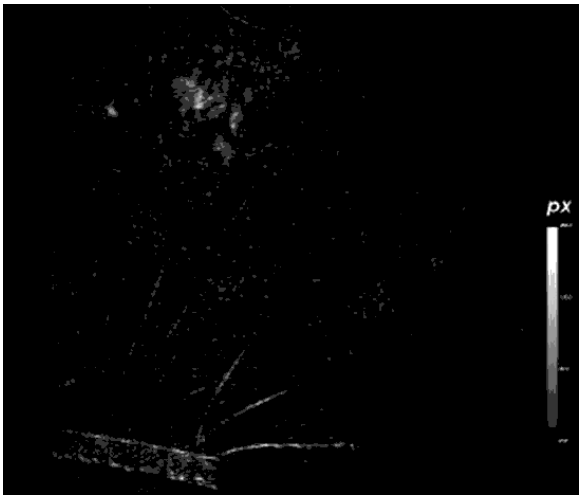

Fig. 7: Another example of a hologram where a particle is distinct to the eye but has low intensity pixels. The reconstruction position of the *Chaetoceros* chain to the lower left is not indicated by any peaks in skewness.

Recording in the laboratory and comparison with the FlowCam® - Procedure and assessment – The microscope was tested for laboratory use by inserting a flow-through chamber into the microscope opening. To image small volumes, the outflow tubing was clipped and the chamber filled with 12 mL of sample. The samples were recorded for 2-3 minutes using a 3-µs pulse duration. Several laboratory cultures were imaged using this method including *A. sanguinea, G. spirale*, *H. triquetra*, *O. marina*, *I. galbana*, and *P. micans*. The flow-through attachment was set up in-line to the FlowCam® by connecting the waste outflow of the FlowCam® to the inflow of the flow-through chamber. A 12-mL sample was injected at once with a syringe into the flow-through chamber of the FlowCam®. The sample tested was a mixture of *Thalassiosira*, *Fragilariopsis*, and *Eucampia*. Copepods isolated from Narragansett Bay were imaged as well

Out of the five laboratory cultures imaged with the holographic microscope, the best images came from *A. sanguinea*. The shape of the dinoflagellate is clear, and in some instances the longitudinal flagellum of the organism is visible (Fig. 8a). Several videos were created using 20-40 reconstructed holograms of *A. sanguinea* where the helical swimming motion of the dinoflagellate can be observed. *Prorocentrum* was also imaged but with less detail. Images from the other three dinoflagellate cultures were not distinct and particles only resolved as small dots.

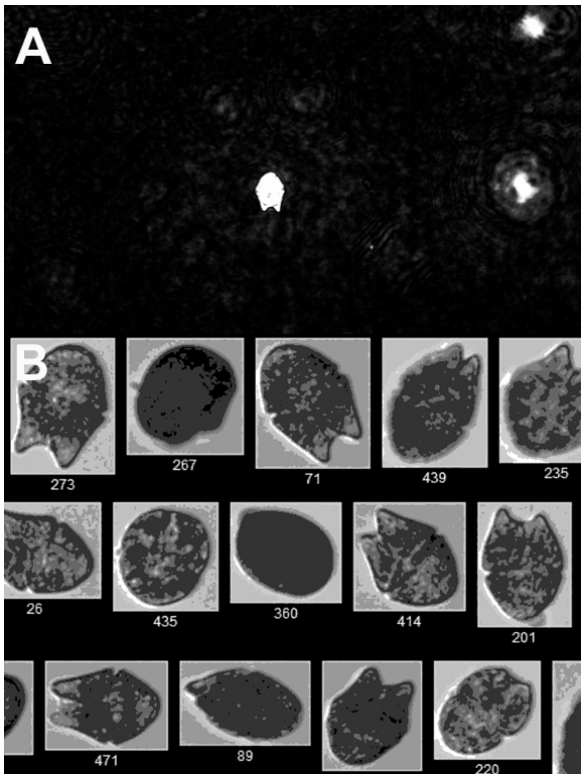

Fig. 8: (a) Image of *Akashiwo sanguinea* from DHIM. Several of these frames can be pieced together to create a video of the dinoflagellate's swimming behavior. (b) Images of *A. sanguinea* from FlowCam® where pigmentation inside is visible.

The FlowCam® was able to resolve details indicating pigmentation inside

dinoflagellate cells (Fig. 8b). The FlowCam® also captures color whereas the holographic microscope produces false color images. The FlowCam® was able to detect and image all dinoflagellates with the exception of *H. triquetra*.

In the in-line experiment with the FlowCam®, an assemblage of centric and pennate diatom frustules from a sediment core sample was imaged. In the hologram reconstructions, the diatoms were represented by simple circular or stick-like particles whereas the FlowCam® imaged details such as patterns on diatom frustules.

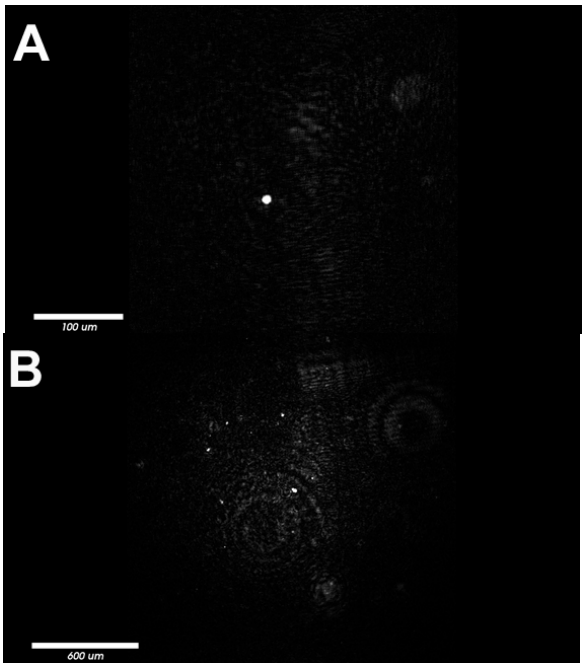

Fig. 9: (a) At low reconstruction positions, the DIHM uses a higher magnification. (b) At higher reconstruction positions, particles are imaged with lower magnification - compare the size of the two scale bars in (a) and (b).

Microscope bias – A characteristic of the holographic microscope is that its imaging volume resembles a cone, with the smallest cross-sectional area where the laser is emitted and the largest area near the camera. When Octopus reconstructs a hologram, it produces an image with a dimension of 1022 by 570 pixels regardless of its position in the imaging cone. Therefore, particles in the smallest part of the cone look much larger than particles of the same size located at a higher reconstruction position. While this size discrepancy is represented by Octopus as a variable scale bar, the skewness analysis does not take into account this size misrepresentation. Small particles close to the laser will be picked up as significant particles although thousands of these same particles occur throughout the imaging volume (Fig. 9).

The size of particles within the imaging volume strongly influences the reconstruction quality. Less noise and small particles are visible in holograms containing a large particle such as a zooplankton or a colony of phytoplankton even at reconstruction locations where the large particle is not in focus.

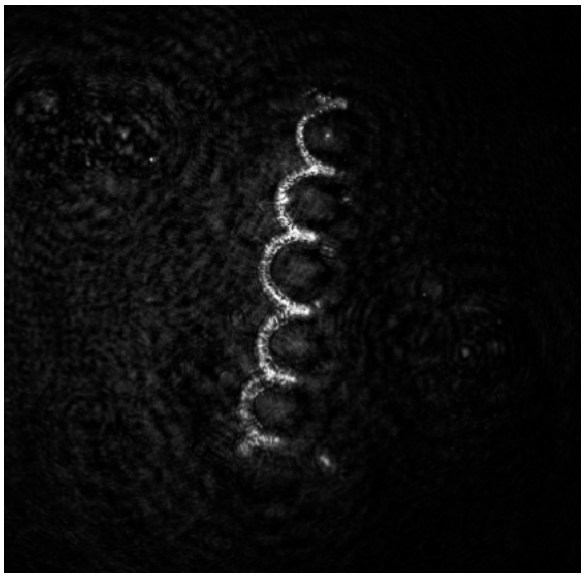

Fig. 10: Spiral-shaped diatom chains such as this are characteristic of holograms from Halifax, Nova Scotia.

Evaluating differences in community structure – The main identifying features of the holograms taken in Halifax are large colonies of *Chaetoceros*. In particular, spiral shaped colonies resembling *C. debilis* are

abundant (Fig. 10), as well as large colonies of *C. socialis*. Many rod shaped diatom colonies are also identifiable.

In contrast, the holograms taken in Narragansett Bay are lacking in large colonies and the most prevalent phytoplankton are the rod like diatom chains, likely *Skeletonema* spp. Another major difference between the two locations is that holograms from Narragansett Bay are abundant in zooplankton, including some which resemble copepods, crab zoea, and ciliates. In contrast, no large zooplankton were found in the Halifax holograms.

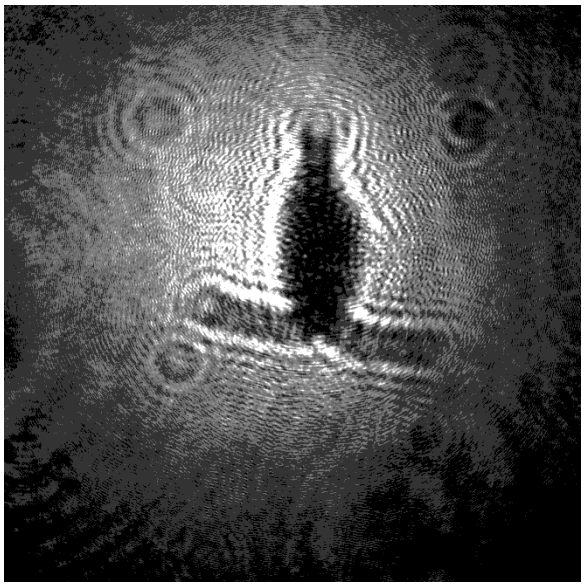

Fig. 11: The shape of the copepod is visible in this raw hologram bitmap before processing. Large discrete particles are easy to locate.

Zooplankton from Narragansett Bay were imaged. Copepods and other zooplankton are easily identified in the holograms and often, the shape of a zooplankton is identifiable in the raw hologram bitmap even before it is reconstructed (Fig. 11). However, no gelatinous zooplankton were identified because the refractive index of gelatinous organisms similar to water makes them hard to image with holography. Although single-celled protists are on the smaller end of what can be imaged with the DIHM, a ciliate (cf. *Myrionecta* sp.) was identified in a hologram taken in Halifax (Fig. 12).

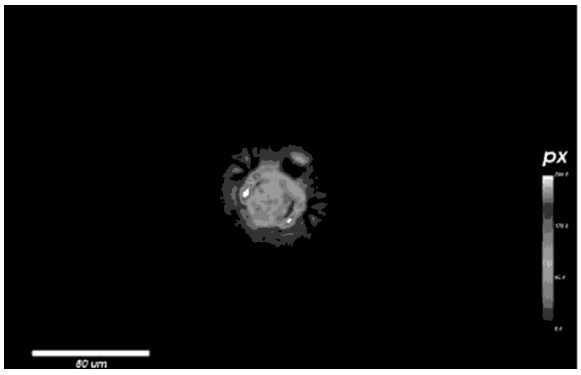

Fig. 12: Reconstruction of a ciliate, possibly *Myrionecta*, imaged in Halifax, Nova Scotia.

Other attempts – Another method tested for processing reconstructed holograms involved projecting the brightest pixel among all the reconstructions in a given (x,y) location onto a single plane (Fig. 13a). The advantage was that it allowed for easy counts of total particles and measurements of surface area. However, it also amplified noise. With noise filtering, this method may be useful in holograms where there are only a few scattered particles, or one or two larger, discrete particles. In a hologram we used to test this method, containing a large colony of *Chaetoceros socialis* (Fig. 13b), this projection erased all of the information contained in the original reconstructions except a general idea of the size of the particle.

Preliminary efforts also included attempts to create 3D visualizations. A reconstructed image was cropped around a particle and divided into 3 by 3 sections to find the ”front” and ”back” locations of the object of interest. Alternatively, the brightest pixel in a given (x,y) location was plotted in a 3D scatter plot against its corresponding reconstruction position (or z value).

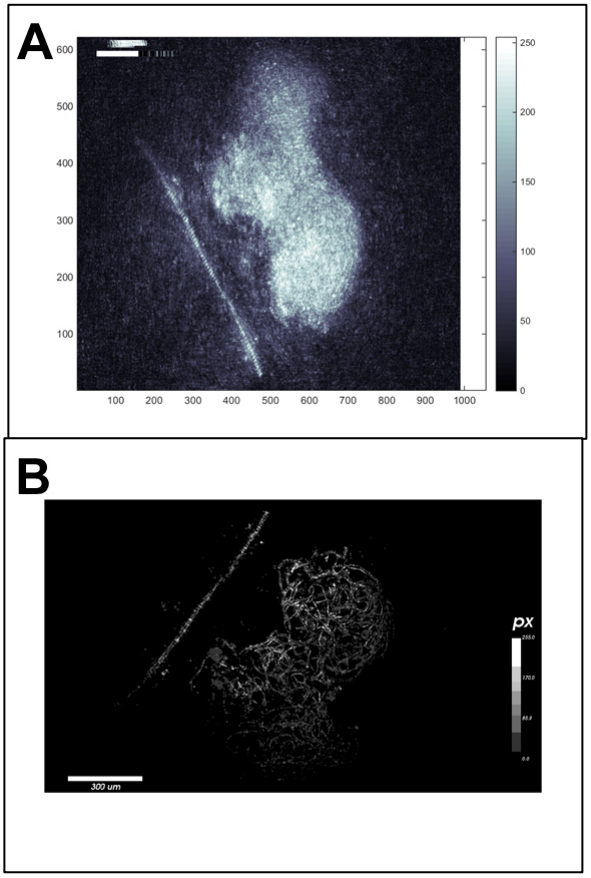

Fig. 13: (a) Projection method, which projects the brightest pixels at an (x, y) location to a 2D plane, greatly amplifies the noise in the image. (b) Single reconstruction image from skewness analysis shows more details than is shown by the projection method.

The results from the 3D visualization methods are crude and do not appear to accurately represent the z-depth of a particle. The resulting 3D scatterplots showed little coherent structure along the z-axis. The resolution of particles in a hologram along the z-axis is much less than in the x and y and makes it difficult to form a picture of the 3D particle structure.

DISCUSSION

The DIHM has the ability to record over a terabyte of raw data per day. When a raw hologram is reconstructed, a single bitmap file is translated into a hundred or more reconstructions, quickly multiplying the number of files to manage. The methods developed for remote control of Octopus for hologram reconstruction and the use of skewness as a measure of how in focus a reconstruction are the first steps towards automating the process of extracting useful information from these data. A partly or fully automated data processing technique is necessary take advantage of the full potential of the DIHM to record in situ images.

Because the DIHM is not limited to a single focal depth as are traditional microscopes, it has the ability to record the behavior of phytoplankton and characterize the sinking rate of marine snow and other particles in the field. In situ data, such as those provided by the DIHM, is necessary to concurrently quantify physical and biological parameters and study the vertical stratification of phytoplankton and harmful algal bloom formation (Berdalet et al., 2014).

It could also be used in the future to contribute to long term studies such as the weekly phytoplankton trawl in Narragansett Bay. As part of the survey, water samples are taken back to the lab to make counts of phytoplankton and zooplankton species by hand. Currently this is the only way to resolve details about species composition but the DHIM could be used in the future to aid any studies which would benefit from characterization of the plankton population.

COMMENTS and RECOMMENDATIONS

Currently, all holograms are reconstructed. However, reconstructing a raw hologram bitmap is time intensive and a preliminary filtering of the holograms before reconstruction to discard holograms without particles would be a simple step to

implement. Also, the current Findpeaks function used does not always agree with the manual choice of what is a peak in skewness. Developing a more optimal function to choose peaks in skewness will make the automated process of choosing in-focus images more accurate.

Despite background subtraction, many images remain noisy. Applying different noise filters such as a high pass filter could result in higher quality images. The possibility of imaging particles in 3D should also be further explored. An alternative reconstruction setting in Octopus allows for a reconstructed image to represent the phase information of a hologram. This has potential to better resolve information about the z-axis.

ACKNOWLEDGEMENTS

We acknowledge the National Science Foundation, the University of Rhode Island Graduate School of Oceanography, and 4-Deep. We thank Sarah Flickinger, Captain Tom Puckett, Neil Redmond, Malcolm McFarland, Amanda Montalbano, Ted Durbin, and Mary Kane for their help.

REFERENCES

Berdalet, E., et al. "Understanding Harmful Algae in Stratified Systems: Review of Progress and Future Directions." Deep-Sea Research Part Ii-Topical Studies in Oceanography 101 (2014): 4-20.

Bochdansky, Alexander B., Manfred H. Jericho, and Gerhard J. Herndl. "Development and Deployment of a Point-Source Digital Inline Holographic Microscope for the Study of Plankton and Particles to a Depth of 6000 m." Limnology and Oceanography-Methods 11 (2013): 28-40.

Chavez FP, Messie M,Pennington JT,. "Marine Primary Production in Relation to Climate Variability and Change." Annual review of marine science 3 (2011): 227-60. /z-wcorg/.

Durham, William M., John O. Kessler, and Roman Stocker. "Disruption of Vertical Motility by Shear Triggers Formation of Thin Phytoplankton Layers." Science 323.5917 (2009): 1067-70.

Jericho, SK, et al. "Submersible Digital in-Line Holographic Microscope." Review of Scientific Instruments 77.4 (2006): 043706.

H. Boo is at McGill University, Montreal, QC, Canada (hyunyungboo@gmail.com)
M. Omand (momand@uri.edu)

Comparing Modeled Gulf Stream Strength and Variability to Observations

Keaton Brenneman[1], Kathleen Donohue[1], Kellen Rosburg[1], John Lillibridge[2], Thomas Rossby[1]

[1]Graduate School of Oceanography, University of Rhode Island, Kingston, RI
[2]NOAA Laboratory for Satellite Altimetry, College Park, MD

ABSTRACT

The Real Time Ocean Forecasting System (RTOFS) is a 1/12° resolution global ocean model, based on the HYbrid Coordinate Ocean Model (HYCOM), produced by NOAA National Centers for Environmental Prediction. RTOFS is utilized by various departments within NOAA for hurricane and climate prediction, and is used to set boundary conditions for regional models. A quantitative assessment of model strengths and weaknesses is essential to understanding the accuracy of its predictions. The Oleander Program collects high-resolution (1.5 km) velocity profiles to 600-m depth using a shipboard acoustic Doppler current profiler aboard the CMV Oleander during weekly voyages between New Jersey and Bermuda. With over 20 years of data, the Oleander dataset offers a unique opportunity to validate the model. RTOFS velocity data are resampled along the Oleander track and rotated into down-stream and cross-stream components to allow comparisons of Gulf Stream structure including core strength, width, shear and transport to the most recent ten years of Oleander data. The Gulf-Stream's lateral structure differs greatly between model and observations and Gulf Stream transports for RTOFS and the Oleander are within ~13%: 48.6 Sv and 54.8 Sv (1 Sv = 10^6 m^3s^{-1}) respectively. RTOFS underestimates the narrow near-surface Gulf Stream peak velocity by 35–40% and the Gulf Stream width is 30% wider than observed. As a consequence, both cyclonic and anticyclonic shears are underestimated in RTOFS. Cyclonic and anticyclonic shears are about 50% weaker. The wider, weaker Gulf Stream displayed by RTOFS is likely due to the model's coarse horizontal resolution.

For the past 20 years, the Oleander Program has been collecting weekly high-resolution velocity profiles during transits between New Jersey and Bermuda. These profiles have enabled intense study of the velocity structure of the continental shelf, continental slope, Gulf Stream (GS), and Sargasso Sea. The GS is the most important of these regions: it is the North Atlantic Ocean's subtropical western boundary current and a northward return branch of the meridional overturning circulation. Hence, it plays a major role in global distribution of heat and affects climate and weather. The Oleander Project has helped quantify many aspects of the GS such as mean velocity, temperature flux and energetics (Rossby and Gottlieb 1998), potential vorticity structure (Rossby and Zhang 2001), and interannual transport variations (Rossby *et al*. 2010).

The Oleander Project dataset offers a unique opportunity to validate numerical simulations of ocean circulation. In particular, a model's ability to reproduce the GS speed and structure is not only important in accurately portraying dynamics in the North Atlantic, but also demonstrates its ability in resolving western boundary currents around the world. The focus of this project is NOAA's Real Time Ocean Forecast System (RTOFS). This 1/12° resolution global ocean model is based on the HYbrid Coordinate Ocean Model (HYCOM), and produced by NOAA

National Centers for Environmental Prediction (NCEP). RTOFS is utilized by various departments within NOAA for hurricane and climate prediction, and is used to set boundary conditions for regional models. The specific goal of this project is to conduct a quantitative comparison between the RTOFS GS and the observed GS through measures of velocity, vorticity, and location.

DATA

Model – The global Real Time Ocean Forecast System (RTOFS) is evaluated in this study. RTOFS is an assimilated ocean model based on the 1/12° global HYbrid Coordinate Ocean Model (HYCOM; Chassignet et al. 2009). It has 32 vertical levels in a hybrid coordinate system that uses isopycnal layers in the stratified ocean, bottom-following σ-coordinates in coastal areas, and fixed-thickness z-coordinates in the mixed layer (Bleck 2002). Two-day nowcasts and six-day forecasts are produced by NCEP. Daily initialization comes from the Navy Coupled Ocean Data Assimilation system (NCODA) using real-time satellite SST and altimetry data, ARGO float profiles, and XBT data (Cummings 2005; Cummings and Smedstad 2013). Forecasts are forced by Global Forecast System (GFS) 3-hour precipitation, momentum, and radiation fluxes. This study utilizes one year of RTOFS daily nowcasts spanning July 2014 – July 2015.

Observations – The Oleander Project has been collecting velocity profiles during weekly transits between Port Elizabeth, NJ and Hamilton, Bermuda for over 20 years. During the most recent 10 years, the CMV *Oleander* has been outfitted with a 75 KHz Acoustic Doppler Current Profiler (ADCP), which profiles to 600 m -every 5 minutes (~1.5 km). Along with velocity profiles, ADCP temperature measurements are used to observe the temperature at 4-m depth. Oleander data from 2005-2015 were used because of the limited number of quality crossings during the RTOFS timeframe. Bubble drawdown significantly degrades ADCP measurement quality, especially in rough crossings (Flagg *et al.* 1997). During the past year, only 28 near-complete GS crossings were available. Since GS structure and transport over the 20-year Oleander Project has been remarkably stable (Rossby *et al.* 2014), an assumption is made that the average structure over the past 10 years would be comparable to the average structure for the past year.

METHODS

A direct comparison of the GS between RTOFS and Oleander velocity data was achieved using a mean stream coordinate transformation. This process closely followed the methodology of Halkin and Rossby (1986). Each crossing was transformed into a stream coordinate system aligned with the GS. Prior to this transformation, RTOFS velocity fields were interpolated to a nominal Oleander track line to mimic the rotation process performed on Oleander data. First, the GS core was identified: the core was defined as the maximum speed at 50-m depth with a positive meridional component. The coordinate system was defined such that the down-stream axis pointed in the direction of the core velocity vector. The cross-stream axis is perpendicular to the down-stream direction. This aligned the coordinate system with the GS flow. Positive cross-stream direction is southeast, toward Bermuda. The zonal and meridional velocity components were then rotated into the cross and downstream coordinate system. Note that because the cross-stream coordinate and the Oleander track were not necessarily co-located, measured and modeled positions were projected onto the new coordinate

system. Figure 1 is a visualization of this transformation directly from Halkin and Rossby (1986).

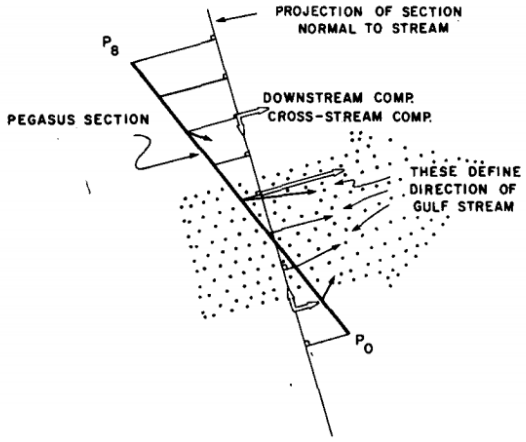

Fig. 1: Visual of stream-coordinate transformation from Halkin and Rossby (1986). The 'Pegasus Section' is comparable to Oleander/RTOFS transects.

GS position was determined from temperature using ADCP measurements at ~4 m depth on the Oleander and the corresponding near-surface RTOFS temperatures. Temperature was used instead of velocity because it provided more data for comparison. First, maximum temperature west of 69° W was identified. The GS core is then defined as the location at which temperature decreased by 2° C from the maximum. We required that this location occurred west of 69° W.

RESULTS AND DISCUSSION

Mean Velocity and Transport – Mean near-surface downstream velocity shows peak velocities at ~2.1 m/s and ~1.3 m/s for Oleander and ROTFS, respectively (Fig. 2). On average, RTOFS-modeled GS core velocity is 35-40% weaker than observations. GS boundaries were defined by the first zero crossing on either side of the core. The Oleander's GS is about 200 km wide whereas RTOFS models the GS is

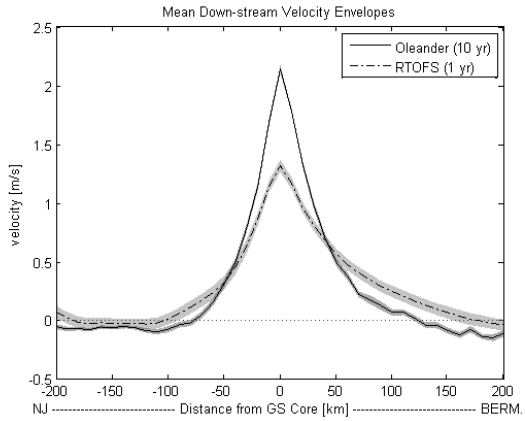

Fig. 2: Mean downstream Gulf Stream velocity at 50 m depth in m/s, with mean standard error envelopes (one week = 1 degree of freedom).

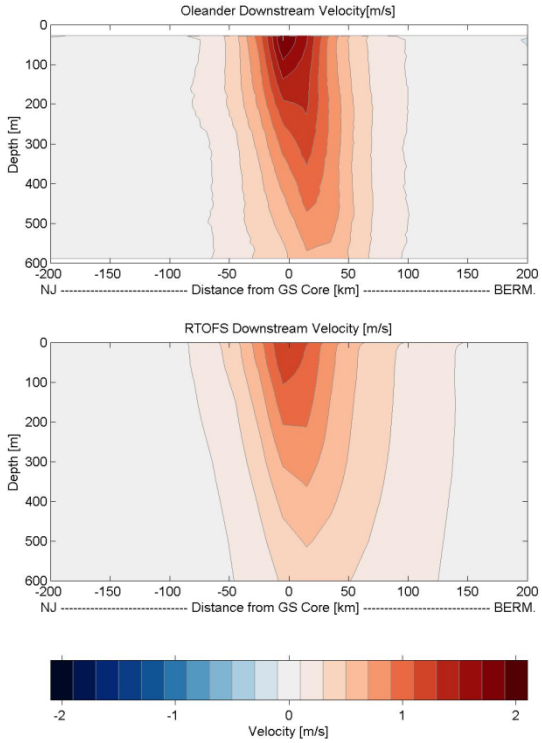

Fig. 3: Mean Gulf Stream velocity in m/s contoured as a function of depth and distance from the core. The contour interval is 0.2 m/s.

about 280 km wide (~30% wider). The weaker, wider GS displayed in RTOFS could be attributed to coarser model resolution, which may smear out the GS, diminish peak velocity, and widen the

current. At depth, RTOFS' GS is consistently wider and weaker than the Oleander representation (Fig. 3). GS transport is determined from mean GS downstream coordinate velocity structure (Fig. 2), integrated between zero velocity crossings down to 600 meters depth. RTOFS transport of 48.6 Sv is nearly 6 Sv less (13%) than Oleander transport of 54.8 Sv. At 50 meters depth, transport of a 1 m deep slice across the GS is 0.1224 Sv in the Oleander data and 0.1157 Sv in the model. Down to 2000 m RTOFS shows 87 Sv of transport. A scale factor of 700 was used in the past to determine transport to 2000 m depth from transport of a 1 m section at 50 m depth, which would put Oleander transport to 2000 m depth at 85.7 Sv (. *et al* 2014). Using transport from RTOFS, the scale factor in the model is 752.5, meaning the 700 scale factor would underestimate transport.

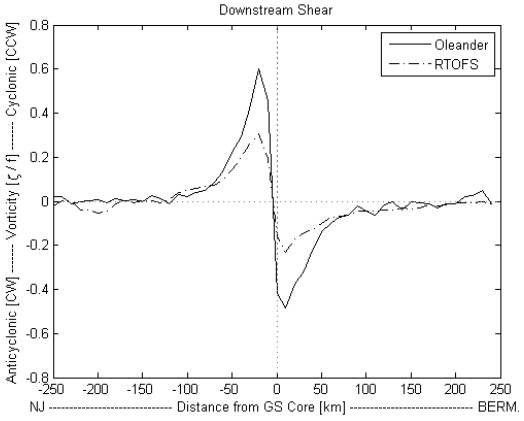

Fig. 4: Gulf Stream shear structure normalized by local value of the Coriolis parameter at 50-m depth.

Vorticity – Relative vorticity is defined as

$$\zeta = (dv\_d)/(dx\_c) - (dv\_c)/(dx\_d)$$

where v is velocity, x is distance, and subscript c signifies the cross-stream direction and subscript d signifies the downstream direction Here, only contributions from $(dv\_d)/(dx\_c)$ are considered. We assume cross-stream velocity components are an order of magnitude less than downstream velocities. The f-plane approximation is made, and shear normalized by the Coriolis parameter f (Fig. 3). Anticyclonic shear on the seaward side of the RTOFS modeled GS is -0.23 and cyclonic shear is 0.30 on opposite side. Cyclonic and anticyclonic GS shear in Oleander was measured at 0.60 (ζ / f) and -0.48 (ζ / f), respectively (Fig. 4). These numbers are expected due to the weaker and wider modeled GS.

Variance – RTOFS' variance is weaker than measured variance near the GS (Fig. 5). In addition, measured variance ellipses are slightly elongated in the along-stream (and along-isobath direction) in contrast to RTOFS' variance ellipses which point mainly to the north in the GS. The reason for this difference is unclear at this time.

Position – Observed and modeled GS position are similar over the past year (Fig. 6) at 37.97 °N vs 37.91 °N and 70.79 °W vs 70.65 °W for RTOFS and Oleander, respectively. Standard deviations are also nearly identical. Position tracks relatively well over time, with a root-mean-squared difference of 46.94 km. Differences between RTOFS and Oleander can be attributed to several sources. RTOFS was interpolated to a nominal Oleander track and occasionally the Oleander deviated by more than 50 km from its nominal course (~25% of crossings). Second, noting that both time series are noisy, the technique to find the GS may need refinement. Note, for example, that the Oleander time series can change by 150 km over one week. Future refinements should spatially low-pass the temperature records before finding the 2 °C drop point, or collect more data and compare velocity core location.

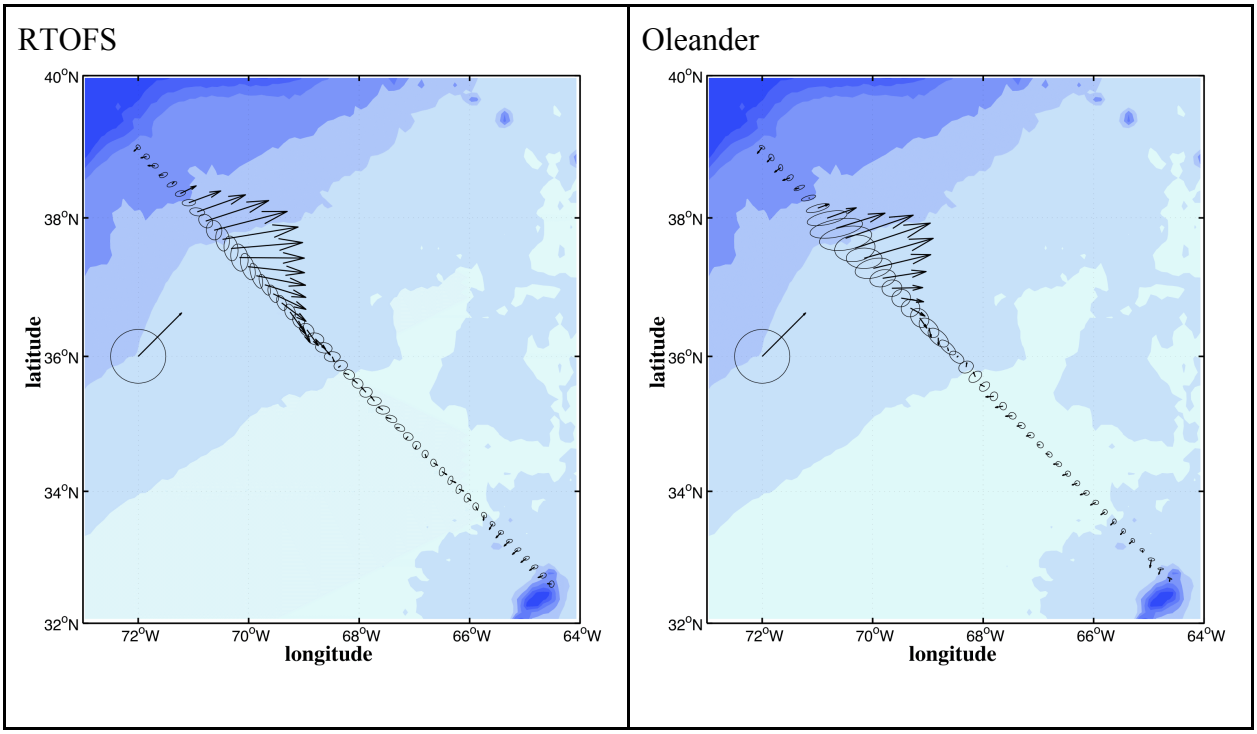

Fig. 5: RTOFS and Oleander mean velocity vectors and direction variance ellipses.

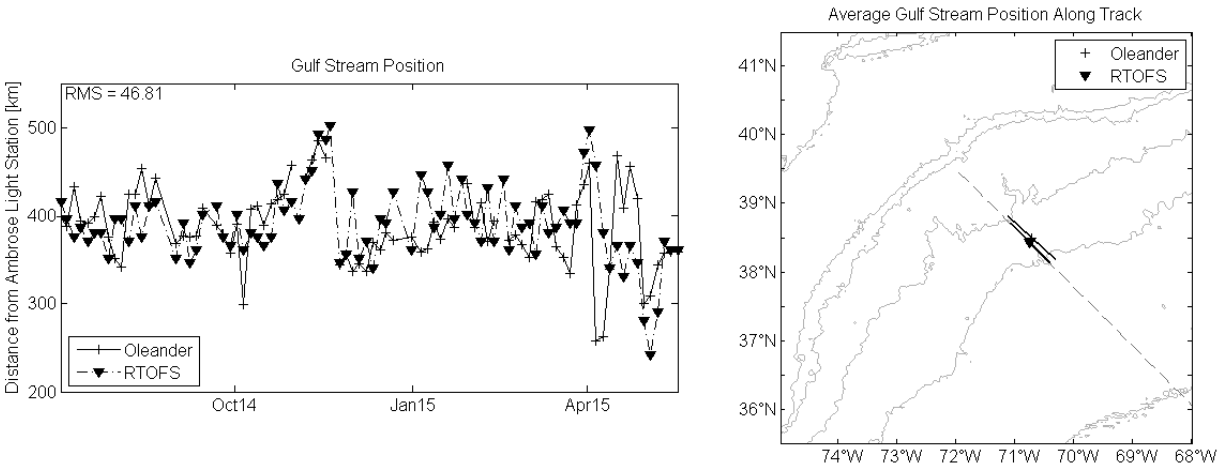

Fig. 6: Position of the Gulf Stream over time in km from Ambrose Light Station (left) and mean position with standard error bars (right).

CONCLUSION

RTOFS displays a weaker, wider GS than measured by the CMV Oleander. A likely candidate for this difference is model resolution. The 1/12° resolution in RTOFS could smear out the GS and cause weaker core speeds and a wider structure. A second candidate would be the assimilation scheme. In particular, the modeled GS may be sensitive to the smoothing of altimetry data over a satellite's ~10-day repeat cycle. Future efforts could determine the source of errors. The impact of a weaker and wider GS depends upon the how RTOFS model fields are used. For example, a regional

model that relies on the RTOFS for a boundary condition may have weaker eddy variability. The Oleander dataset provides a unique opportunity to test a model's ability to emulate the complex dynamical processes that form the GS. Future efforts could compare other models at a variety of resolutions to assess the effect of resolution on smearing, as well as compare the performance of models to each other.

ACKNOWLEDGEMENTS

The Oleander Program has been possible only through the extraordinary help and collaboration from Bermuda Container Line, The Neptune Group, and the captains, engineers and electronics officers of the ship. Kathleen Donohue was supported by NSF grant OCE-825418. Keaton Brenneman was supported by NSF grant OCE-1460819.

REFERENCES

Chassignet, E.P., and co-authors: 2009. US GODAE: Global Ocean Prediction with the HYbrid Coordinate Ocean Model (HYCOM). Oceanography, **22** (2), 64-75

Cummings, J. A.: 2005. Operational multivariate ocean data assimilation. Q.J.R. Meteorol. Soc., **131**, 3583–3604.

Cummings, J. A. and O. M. Smedstad: 2013. Variational data assimilation for the global ocean. In: Park, S. K., Xu, L. (Eds.), Data Assimilation for Atmospheric, Oceanic and Hydrologic Applications (Vol. II). Springer Berlin Heidelberg, pp. 303–343.

Flagg, C.N., G. Schwartze, E. Gottlieb, and T. Rossby: 1997. Operating an acoustic Doppler current profiler (ADCP) aboard a container vessel. Journal of Atmospheric and Oceanic Technology, **15**, 257–271.

Halkin, D., T. Rossby: 1985. The Structure and Transport of the Gulf Stream at 73° W. Journal of Physical Oceanography, **15**, 1439-1452.

Rossby, T., C.N. Flagg, K. Donohue, A. Sanchez-Franks, J. Lillibridge: 2014. On the long-term stability of Gulf Stream transport based on 20 years of direct measurements. Geophysical Research Letters, **41** (1), 114-120.

Rossby, T., C.N. Flagg, K. Donohue: 2010. On the variability of Gulf Stream transport from seasonal to decadal timescales. Journal of Marine Research, **68**, 503-522.

Rossby, T., E. Gottlieb: 1998. The *Oleander* Project: Monitoring the Variability of the Gulf Stream and Adjacent Waters between New Jersey and Bermuda. Bulletin of the American Meteorological Society, **79** (1), 5-18.

Rossby, T., H.-M. Zhang: 2001. The near-surface velocity and potential vorticity structure of the Gulf Stream. Journal of Marine Research, **59**, 949-975.

K. Breneman is in the School of Environmental and Biological Sciences, Rutgers University, New Brunswick, NJ (kbrenneman3@gmail.com)
K. Donohue (kdonohue@uri.edu)
K. Rosburg (rosburk@my.uri.edu)
J. Lillibridge (john.lillibridge@noaa.gov)
T. Rossby (trossby@uri.edu)

Episodic Tremor and Slip in South Central Alaska

Blake Cross and Meng Wei
Graduate School of Oceanography, University of Rhode Island, Narragansett, RI 02882

Abstract

The episodic tremor and slip (ETS) in subduction zones is one of the most exciting discoveries of the last decade. ETS in south central Alaska is understudied despite its potential for prediction and understanding of seismic activity in subduction zones. A slow slip event between 2009 and 2013 has been recorded in GPS data, but it is not known if coinciding tremors occurred. We searched for tremor signals in south central Alaska from 2010 to present using seismic data from a local seismic network. The data were filtered using a band-pass filter between 1-6 Hz, which was chosen based on previous research. Potential tremors were detected using a waveform envelope method and were then visually inspected under several general criteria for validation. The observed tremors were recorded in a time series portraying frequency of occurrence. There was a decreasing trend in tremor activity from 2010 to 2013 that leveled off in 2014. This shows that tremor activity did intensify during the slip event and returned to normal after the conclusion of the event. Seasonal variations in tremor activity with a peak in summer have also been observed. The tremors were located using a 1D seismic velocity model and they are within the region of slow slip event. The depth of tremors was not well resolved due to the limited number of seismic stations in this region. We conclude that tremors associated with the 2009-2013 slow slip events did occur in south central Alaska.

Episodic tremor and slip (ETS) was first reported in Cascadia (Rogers and Dragert, 2003). Since then, ETS has been observed in almost all young subduction zones including southwest Japan, Costa Rica, Mexico, and New Zealand (Peng and Gomberg, 2010). Through detailed analysis of these events, our understanding of the variety of slip events has been improved significantly. In most cases, ETS occur near the downdip end of the mega-earthquake rupture area and are likely caused by high pore pressure. ETS might affect the magnitude and timing of future earthquakes (Dixon et al., 2014).

ETS studies in Alaska are quite limited. Only one event between 1998-2001 has been reported (Ohta et al., 2006; Peterson and Christensen, 2009). This is partly due to the long interval between, and duration of, ETS events in Alaska. Between 2009-2013, another slow slip event has been observed on the newly established Plate Boundary Observatory (PBO) GPS network (Wei et al., 2012; Fu and Freyuxxx, 2013; Fu et al., 2015). Enhanced seismic activity has also been observed with the slow slip event (Wei et al., 2012; Fu et al., 2015). However, it is unknown whether tremors occur with this slow slip event.

In this paper we searched and located tremors since 2010 using seismic data in the Incorporated Research Institutions for Seismology (IRIS) Data Management Center (DMC) database. All the tremors discussed in this paper are non-volcanic, which means that they are not related to any volcanic processes. The methodology is adopted from many previous studies (Obara, 2002; Rogers and Dragert, 2003; Wech and Creager, 2008; Peterson and Christensen, 2009). Due to the large amount of data, we picked eight stations with the longest record

and near the previous non-volcanic tremor locations to monitor temporal changes of tremor activities. Then we used additional stations to locate several well-recorded tremors. Our results show that tremor activity has decreased since 2010 and leveled off in 2014, which shows a similar pattern as slow slip event. The tremor locations are within but near the deeper end of the slow slip area. The temporal and spatial results together show that the tremor activities are closely related to the slow slip event. We are not able to resolve depth well as the station coverage is limited.

DATA

All the data used in this study were downloaded from the IRIS DMC database. The Alaska Regional Network provided most of the seismic data that were used for identifying tremor. The Alaska Regional Network (AK network in the IRIS DMC database) currently has 121 stations that predominately cover the area of south central and south eastern Alaska. The data were recorded at a rate of 50 data points per second. Out of the 121 stations, we chose eight stations to monitor the tremor activity changes since 2010. These eight stations cover the northern part of the area of the 2009-2013 slow slip event and a previous identified ETS event (Fig. 1), and had the best chance to identify tremor activities. For locating tremors, we added several more stations including station PMR, which is part of the National Tsunami Warning System seismic network (AT in IRIS data set).

METHODS

Identifying non-volcanic tremors – Non-volcanic tremors (NVT) are seismic signals with low frequency (1-6 Hz) and long duration (several minutes). We adopted an envelope detection method used by many previous studies (Obara, 2002; Rogers and Dragert, 2003; Wech and Creager, 2008; Peterson and Christensen, 2009). Seismic data from eight AK stations were downloaded to a local computer from the IRIS database using the Matlab script irisFetch.m. Due to the limited memory of the computer, we processed four months of data at a time. The waveform data were filtered through a bandpass filter for a frequency range of 1-6 Hz (Peterson and Christensen, 2009). Signals from local earthquakes were masked out based on ratio of peak amplitude and background noise. Once earthquakes were removed an envelope was created to overlay the waveform. The data were then run in hour sections and automatically screened to produce a list of possible tremor events. Only events that last longer than a few minutes were listed. In the meantime, figures with hourly waveforms were produced and were used to visually inspect the tremors.

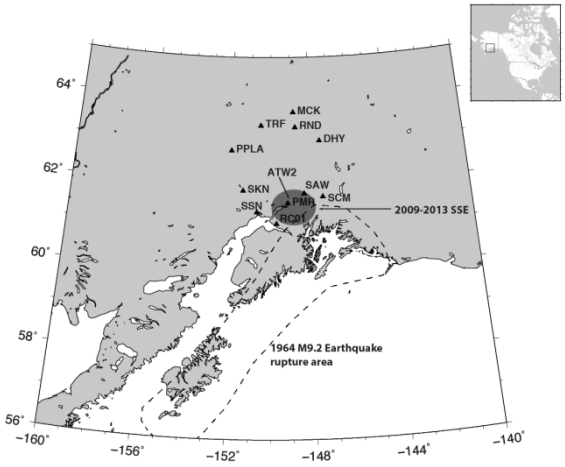

Fig. 1. Map of south central Alaska. The triangles are the eight AK network station locations and one AT station. The darker circle is the region of the slow slip event that occurred from 2009-2013. The dashed line highlights the rupture area of the 1964 M9.2 earthquake. GPS station ATW2 is very close to seismic station PMR.

With the created list of possible tremor hours, the remainder of the identification process was visual. The figures of waveforms with envelopes were visually inspected under the following criteria: (1) the tremors would last for several minutes, (2) they lacked evident P and S waves that would suggest an earthquake, and (3) the times of increased seismic activity were closely aligned and the shapes look alike. From this visual inspection a list of determined tremors was created and usable to show tremor activity per month since 2010. An example is shown in Fig. 2. This tremor event occurred in September 19, 2010. The signal lasted about 10 minutes and showed up in eleven stations. The similarity of the signal and the timing suggested that the signals are from the same event.

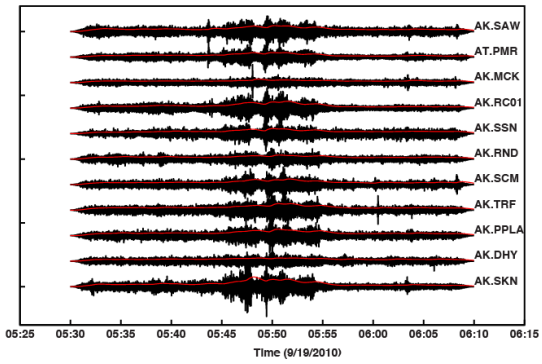

Fig. 2. Waveforms of a well recorded tremor. The black lines are the band-pass filtered waveform and the red lines are the smoothed envelopes. Stations are seven of the eight from the network used for finding times of tremor, with one AT station.

Locating NVT – We locate tremors to understand the spatial relationship between the slow slip event and tremors. Due to large amounts of background noise in many of the figures, there were only several tremor events that were chosen to be located. In order to help with tremor location, additional stations from the AK and AT array were included given the small amount of tremors chosen. The first step in the location process was determining when the tremor arrived at the different stations. The lag time was determined by cross correlating the smoothed envelopes of different stations (Fig. 2). The second step was to forward model the arrival time using a 1D velocity model, a two-layer velocity model based on CRUST 1.0. Then we performed a grid search including location (x,y), depth (z) and origin time (dT). For each grid, a misfit was calculated between the modeled and observed arrival times. The grid that generated the smallest misfit was considered as the most likely location of tremors. We have very good constrains on the horizontal location of the tremor. Resolving the depth was less successful, with the smallest misfit point being usually the largest depth in the search grid.

RESULTS

A total of 171 tremors was determined based on the eight stations between January 2010 and May of 2015. Of these 171, there were 71 in 2010, 36 in 2011, 28 in 2012, 14 in 2013, 16 in 2014, and 6 in the first five months of 2015. The tremor activity per month was plotted on the same figure as the slow slip event displacement recorded in a nearby GPS station (ATW2) (Fig. 3). The GPS data show about 3 cm southward slip over the course of 2010 to the start of 2013, with no significant change in displacement afterward. During the time of the slow slip event, there was an average of 45 tremors per year in contrast to the years with no slow slip event that had an average of 15 tremors per year.

The tremor activity shows a seasonal variation that peaks in the summer. The months for each year of peak tremor activity on average for the eight stations are, in order starting from 2010 and not including 2015, September, July, June, August, and May,

showing a tendency for tremor activity to peak in or around the summer months (Table 1).

We located one tremor that occurred on September 19, 2010. The waveforms are shown in Fig. 2, and the tremor and the slow slip event locations in Fig. 3. We could not accurately resolve the depth of the tremor. The misfit between modeled and observed arrival time tended to decrease with depth. However, it is hard to imagine physically how a tremor can occur at 100-km depth. Therefore, we showed three locations in the depth range from 20-30, 40-50, and 60-70 km (Fig. 4). In all three cases, the tremor occurs near the downdip end of the slow slip event, which shows a possible link between the two phenomena.

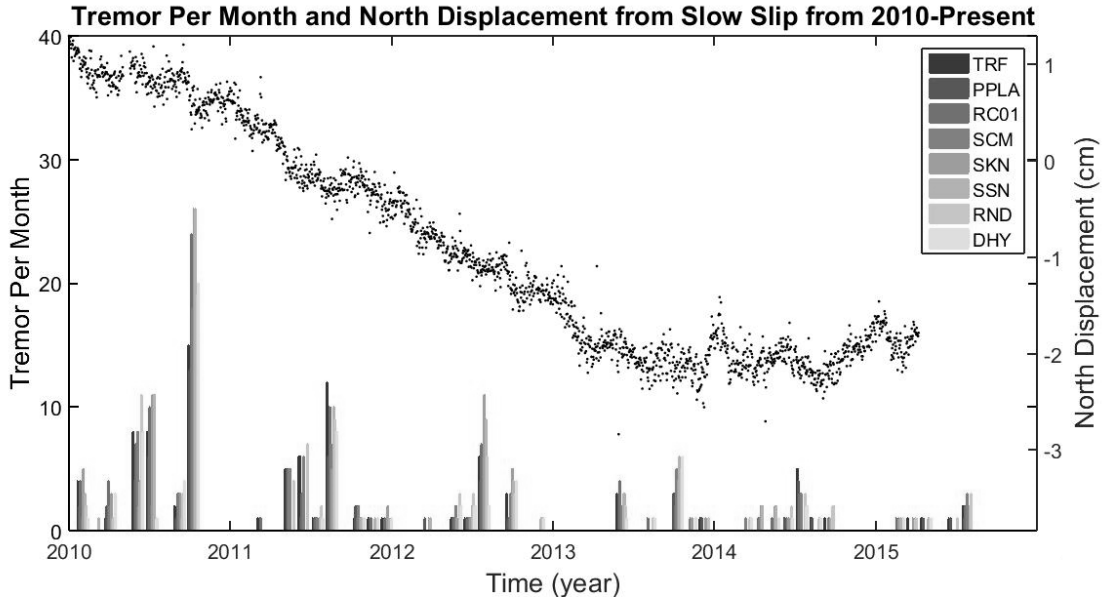

Fig. 3. Surface displacement and tremor activities since 2010. The left Y-axis refers to the number of tremors per month (bar graphs). The right Y-axis is the slow slip event displacement (symbols) for station ATW2. The increase of tremor activity in the months that the slow slip occurred over shows the existence of a temporal relationship between the slow slip event and the NVT activity.

DISCUSSION

Several factors affect the robustness of identifying tremors. One factor is times of high noise levels that would prevent a tremor from showing up in the waveform. The second factor occurs during the subjective visual inspection of the figures to confirm or deny the existence of tremors. Though the visual inspection follows a set of rough guidelines for identifying tremors, there are often cases where it is not possible to clearly distinguish a tremor from an earthquake or string of earthquakes. This issue is diluted by the large number of possible tremors that arise and the consistency with identification; it is not significant to the point of incorrectly skewing results. However, more precise results could be obtained if better managed. Despite these reservations, the temporal data clearly show the connection through the observation of the tremor activity before and after 2013. With the tremor activity before 2013 three times larger than that after 2013 and the slow slip event ending at the start of 2013, the temporal relationship between the two appears very evident.

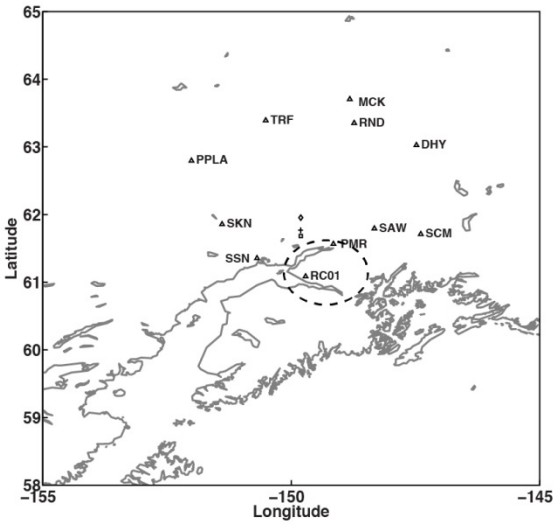

Fig. 4. Seismic stations and tremor locations. The triangles are the stations used to locate the tremor in 9/19/2010. The dashed line indicates the area in which the slow slip event occurred between 2009 and 2013. The diamond, plus sign, and square indicate the determined location of the tremor based on depth of 20-30 km, 40-50 km and 60-70 km respectively.

The location of an NVT in terms of latitude and longitude plotted in Fig. 4 shows a spatial relationship between the slow slip and NVT, where the NVT occurs just downdip of the slow slip event, a result consistent with that found in an earlier slow slip in the same area (Peterson and Christensen, 2009). Unlike with our results, Peterson and Christensen were able to estimate depth likely because they had many more stations due to the existence of a temporal seismic array.

CONCLUSIONS

For the slow slip event that occurred in south central Alaska from 2009 to 2013, available waveform data were used to identify and locate NVT. There was a decreasing trend in tremor activity from 2010 to 2013 that leveled off in 2014. This shows that tremor activity did intensify during the slip event and returned to normal after the conclusion of the event. Seasonal variations in tremor activity with a peak in summer have also been observed. The tremors were located using a 1D seismic velocity model and they are within the region of slow slip event. The depth of tremors was not well resolved due to the limited number of seismic stations in this region. We conclude that tremors associated with the 2009-2013 slow slip events did occur in south central Alaska.

ACKNOWLEDGMENTS

Special thanks to Lucie Maranda, Kathleen Donahue, David Smith, and Kim Carey for organizing the 2015 SURFO program and for all guidance along the way. We thank NSF for providing the funding for the SURFO program. Thanks are also due to my advisor Meng Wei for his support and involvement in my first research experience.

REFERENCES

Brown, J. R., S. G. Prejean, G. C. Beroza, J. S. Gomberg, and P. J. Haeussler (2013), Deep low-frequency earthquakes in tectonic tremor along the Alaska-Aleutian subduction zone, J. Geophys. Res. Solid Earth, 118, 1079–1090, doi:10.1029/2012JB009459.

Dixon, T. H., Y. Jiang, R. Malerservisi, R. McCaffrey, N. Voss, M. Protti, and V. Gonzalez (2014), Eartqhauke and tsunami forecasts: relation of slow slip events to subsequent earthquake rupture, PNAS, 111,17039-17044, doi:10.1073/pnas.1412299111

Fu, Y., and J. T. Freymueller (2013), Repeated large slow slip events at the south central Alaska Subduction zone, Earth Planet. Sci. Lett., **375**, 303–311, doi:10.1016/j.epsl.2013.05.049.

Fu, Y. and Z. Liu (2015), Spatiotemporal variations of the slow slip event between 2008 and 2013 in the southcentral Alaska subduction zone, Geochem. Geophys. Geosyst.,1525-2027, doi:10.1002/2015GC005904

Ghosh, A., J. E. Vidale, and K. C. Creager (2012), Tremor asperities in the transition zone control evolution of slow earthquakes, J. Geophys. Res., 117, B10301, doi:10.1029/2012JB009249.

Gomberg, J., and S. Prejean (2013), Triggered tremor sweet spots in Alaska, J. Geophys. Res. Solid Earth, 118, 6203–6218, doi:10.1002/2013JB010273.

Obara, K. (2002), Nonvolcanic deep tremor associated with subduction in southwest Japan, Science, 296, 1679 – 1681, doi:10.1126/science. 1070378.

Ohta, Y., J. T. Freymueller, S. Hreinsdottir, and H. Suito (2006), A large slow slip event and the depth of the seismogenic zone in the south central Alaska subduction zone, Earth Planet. Sci. Lett., 247, 108–116.

Peng, Z., and J. Gomberg (2010), An integrated perspective of the continuum between earthquakes and slow-slip phenomena, Nat. Geosci., 22, doi:10.1038/NGEO940.

Peterson, C. L., and D. H. Christensen (2009), Possible relationship between nonvolcanic tremor and the 1998–2001 slow slip event, south central Alaska, J. Geophys. Res., 114, B06302, doi:10.1029/2008JB006096.

Rogers, G., and H. Dragert (2003), Episodic tremor and slip on the Cascadia subduction zone: The chatter of silent slip, Science, 300, 1942– 1943, doi:10.1126/science.1084783.

Wech, A. G., and K. C. Creager (2008), Automated detection and location of Cascadia tremor, Geophys. Res. Lett., 35, L20302, doi:10.1029/2008GL035458.

Wei, M., J. J. McGuire, E. Richardson (2012), A slow slip event in the south central Alaska Subduction Zone and related seismicity anomaly, Geophys. Res. Lett., 39, 15, 1944-8007, doi: 10.1029/2012GL052351

B. Cross is at the Colorado School of Mines, Golden, CO (bcross@mymail.mines.edu)
M. Wei (matt-wei@uri.edu)

Table 1. Tremors per month at each station from January 2010 through May 2015

	TRF	PPLA	RC01	SCM	SKN	SSN	RND	DHY
Jan-10	4	2	4	1	5	3	2	1
Feb-10	0	0	0	0	0	1	0	0
Mar-10	1	2	4	2	3	1	1	3
Apr-10	0	0	0	0	0	0	0	0
May-10	8	4	7	8	2	4	11	8
Jun-10	8	6	10	2	11	11	0	1
Jul-10	0	0	0	0	0	0	0	0
Aug-10	2	1	3	3	3	1	3	4
Sep-10	15	13	24	18	26	26	19	20
Oct-10	0	0	0	0	0	0	0	0
Nov-10	0	0	0	0	0	0	0	0
Dec-10	0	0	0	0	0	0	0	0
Jan-11	0	0	0	0	0	0	0	0
Feb-11	1	0	1	0	0	0	0	0
Mar-11	0	0	0	0	0	0	0	0
Apr-11	5	5	5	5	0	0	4	0
May-11	6	1	3	6	0	0	7	0
Jun-11	1	1	1	1	0	1	2	1
Jul-11	12	6	10	7	5	10	9	8
Aug-11	0	0	0	0	0	0	0	0
Sep-11	1	2	1	2	1	1	1	1
Oct-11	1	1	1	0	0	1	0	1
Nov-11	1	0	1	0	2	1	0	1
Dec-11	0	0	0	0	0	0	0	0
Jan-12	0	0	0	0	0	0	0	0
Feb-12	0	1	0	0	1	1	0	0
Mar-12	0	0	0	0	0	0	0	0
Apr-12	1	1	1	2	1	0	3	2
May-12	1	1	1	1	1	2	3	2
Jun-12	6	4	7	6	11	9	6	2
Jul-12	0	0	0	0	0	0	0	0
Aug-12	3	1	1	3	5	4	3	4
Sep-12	0	0	0	0	0	0	0	0
Oct-12	0	0	0	0	0	1	1	1
Nov-12	0	0	0	0	0	0	0	0
Dec-12	0	0	0	0	0	0	0	0
Jan-13	0	0	0	0	0	0	0	0
Feb-13	0	0	0	0	0	0	0	0
Mar-13	0	0	0	0	0	0	0	0
Apr-13	3	3	4	2	0	3	2	1
May-13	0	0	0	0	0	0	0	0

Jun-13	0	0	1	0	0	0	1	1
Jul-13	0	0	0	0	0	0	0	0
Aug-13	0	3	2	5	4	6	5	6
Sep-13	0	0	0	1	1	0	0	1
Oct-13	1	1	0	0	1	0	1	0
Nov-13	0	0	0	0	0	0	0	0
Dec-13	0	0	0	0	0	0	0	0
Jan-14	0	0	0	1	0	0	1	1
Feb-14	0	0	1	1	2	2	0	0
Mar-14	0	0	1	0	2	2	0	1
Apr-14	0	1	0	1	1	0	2	1
May-14	5	4	3	3	0	0	3	2
Jun-14	1	1	0	0	0	0	1	1
Jul-14	1	0	0	1	1	1	2	0
Aug-14	0	0	0	0	0	0	0	0
Sep-14	0	0	0	0	0	0	0	0
Oct-14	0	0	0	0	0	0	0	0
Nov-14	0	0	0	0	0	0	0	0
Dec-14	0	0	1	0	1	1	0	1
Jan-15	1	0	0	0	1	0	1	0
Feb-15	1	1	0	0	0	1	1	1
Mar-15	0	0	0	0	0	0	0	0
Apr-15	1	1	0	0	0	0	1	0
May-15	2	1	2	3	0	2	3	0

Eastern oyster shell reintroduction and dissolution as a coastal acidification mitigator in Narragansett Bay, RI

Julia Hogan, Sabrina Miller, Anton Post
Graduate School of Oceanography, University of Rhode Island, Narragansett RI, 02882

Abstract

At lower pH, carbonate supply becomes a limiting factor for important shell-building organisms, such as quahogs (*Mercenaria mercenaria*) and eastern oysters (*Crassostrea virginica*). Carbonate, the major constituent of oyster shells, equilibrates with CO_2 and HCO_3^- in a pH-dependent manner and so acts as a pH buffer in seawater. Therefore, recycling of oyster shells may help to stabilize or restore pH to more alkaline values. This research tested the effectiveness of shell reintroduction on estuarine acidification in Narragansett Bay samples with different water quality, sediment presence and shell surface area (through fragmentation). We further analyzed historical pH data for Narragansett Bay, compared effects of shell introduction on pH in controlled experiments, and created the foundations of a mathematical model that forecasts pH change under different scenarios. Model simulations showed that, as pH increases, dissolution rates decrease. Within the model, oyster shell additions significantly raised water pH (from 7.75 to 8.08) over time intervals determined by initial pH and the amount of oyster shells introduced. Within the controlled experiments, there was a significant loss (~3%) of shell material, with an average of 7.78 g per 253 g introduced. Shell loss was less pronounced in tanks that contain sediment than in the control tanks. Surprisingly, seeding environments with crushed shells resulted in a lower loss of total shell weight than environments seeded with whole shells. These results promote a better understanding of the factors that govern oyster shell dissolution, and will inform procedures for mitigation of estuarine acidification via oyster shell recycling.

Estuarine acidification is a complex phenomenon caused by nutrient loading from rivers, as well as by interactions with atmospheric carbon dioxide. Coupled with the stressor of acidification, estuaries are complex areas with daily and seasonal fluctuations in temperature, salinity, and pH. Because of these fluctuations, the changes caused by acidification are exacerbated in the level of stress they cause to estuarine organisms (Ringwood Keppler 2002). Because of these multiple components, organisms that live in estuaries have greater exposure to acidification and thus can expect to see impacts on their physiology and ecology sooner than organisms that live in other marine environments (Waldbusser et al. 2010).

Estuarine pH, like in marine waters, is controlled by seawater carbonate chemistry through a series of reactions:

$$CO_{2(atmos)} \leftrightarrow CO_{2(aq)} + H_2O \leftrightarrow$$
$$H_2CO_3 \leftrightarrow H^+ + HCO_3^- \leftrightarrow 2H^+ + CO_3^{2-}$$

As more carbon dioxide is absorbed from the atmosphere by the ocean, carbonic acid forms and pH values decline. As a result, fewer carbonate molecules are available for calcium carbonate shell incorporation in economically and ecologically vital species, specifically shellfish, such as quahogs (*Mercenaria mercenaria*) and

eastern oysters (*Crassostrea virginica*) (Doney et al. 2009).

Shellfish aquaculture represents a six-million dollar industry in Rhode Island (Cygler, 2014). Shellfish are also filter feeders, therefore remove nutrients and pollutants from the water, helping to deter eutrophication (Dame 2012). Acidification in estuarine waters disproportionately affects shellfish larvae, as the under saturation of aragonite and calcite in acidic waters makes it difficult for larvae to successfully incorporate aragonite or calcite into their shells, leaving them more vulnerable to predation (Salisbury 2008).

A number of scientific institutions but also grassroots organizations have taken initiatives to battle estuarine acidification with oyster shell reintroduction in Narragansett Bay and adjacent salt marshes. Through this process, oyster shells from restaurants and other resources are taken and recycled into these water bodies. The effects are thought to be three-fold: the reintroduced shells provide a localized buffering effect, hard substrate for larval oysters to bed down on, and the rehabilitation of oyster reefs (Waldbusser, et al. 2011). However, though this process is ecologically important, the relationship of shell dissolution and pH is not well understood. For example, how fast do shells dissolve under certain pH conditions? How many shells are needed to see a pH change? How are dissolution rates affected by certain factors, such as sediment introduction, surface area, water flow, and water quality or hypoxia?

MATERIALS AND METHODS

For this project, we implemented a three-pronged approach:

1. We studied effects of sample manipulation on environmental pH in a controlled, laboratory setting,
2. We gathered and analyzed historical pH data from across Narragansett Bay with special attention for Greenwich Bay and water near the Graduate School of Oceanography (GSO),
3. And we created building blocks of a mathematical model that simulates effects of nutrient loading on aquatic productivity along with pH effects on benthic food web (shellfish) ecology.

Experimental Setup – We studied the effects of relative water quality on pH in experimental setups with and without the addition of oyster shells, with the aim to assess effects of shell recycling on acidification mitigation in estuarine waters. Water and sediment samples were collected from Greenwich Bay. Eleven 15-L tanks were filled with 13.5 L of water. In the first pair of tanks, water was mixed at a gradient of 33% Greenwich Bay water and 66% raw seawater from off the GSO dock. In the second two tanks, water was mixed at 66% and 33%, and in the third two tanks, 100% of the water was from Greenwich Bay. In tanks seven and eight, 100% of the water was from off the GSO dock. In tank nine, 100% Greenwich Bay water was mixed with sediment collected from the bottom of Greenwich Bay using a box corer. In tank ten, 100% GSO water was mixed with sediment collected from the bay near the GSO campus. Tank eleven also had 100% GSO water, for the addition of crushed oyster shells.

Spent oyster shells were rinsed with deionized water, photographed using a Nikon d3100 DSLR camera, and weighed on a Scout Pro scale. Each photograph was analyzed for surface area using ImageJ software. Because the shells were very young and relatively flat, the surface area was approximated from the two-dimensional images.

Roughly 253 g of whole oyster shells were placed in every other tank, and in both of the tanks with sediment (tanks nine and ten). Tank eleven received 253 g of crushed oyster shell tied inside a panty hose to permit unimpaired flow through of water. Separately, 253 g of crushed shell and 253 g of whole shell were placed in tanks with flowing seawater. Raw seawater pumped from off the GSO dock flowed over these shells at a rate of 1395 $\pm$ 50 mL/minute, $\pm$ 50 mL.

Salinity and temperature (YSI ± 0.01 unit) were recorded twice a day in each of the eleven tanks. In the tank with flowing seawater, a profiling YSI probe recorded temperature and salinity every hour. In the eleven standing tanks, samples were taken for pH testing, and tested using an Orion Star A211 pH meter equipped with an Orion 9156BNWP pH electrode. The pH readings were calculated against filtered seawater, which was found to having a (standing pH of 8.08 ± 0.05).

Historical Data – Historical data were collected along a time series from 2004 to 2012, only for the "summer" time period, or from June 27th to October 1st. We took the pH, temperature, salinity, and depth for the Greenwich Bay surface location. We coupled these data with historical quahog density data in Greenwich Bay for the years 2004, 2005, 2006, 2007, 2010, and 2012. We used the average quahog weight (g/m^2) as an approximate total weight in Greenwich Bay for the entire time series. Using a formula from Lee et al. (2006) and an experimental Total Alkalinity value from Turner (2015), we were able to approximate the Total Alkalinity within Narragansett Bay based on Temperature and Salinity. We ran these variables through a program called CO2SYS (Lewis, Wallace 2011) to calculate the rest of the Ocean Acidification Equation variables based on the input of two variables, in our case, pH and Total Alkalinity.

With the output from CO2SYS, we found calcite and aragonite saturation states and solubility coefficients. These numbers, along with the surface area of available calcium carbonate, were used in the following equation from Morse et al. (2007):

$$r = K'sp\frac{A}{V}(1-\Omega)^n$$

where r is the dissolution rate, K'_{sp} is the calcium carbonate solubility coefficient, A is surface area of available calcium carbonate (in moles/L), V is volume, Ω is the saturation state of aragonite or calcite, and n is the order of the overall reaction. For this equation, we used overall reaction numbers of n = 4.5 for calcite, and n = 4.2 for aragonite (Schulz and Zabel 2013). This equation allowed us to find the dissolution rate as it changed with the changing pH over the time period of 2004-2012.

Model Components – The above equations were used to create the components of a model that simulates how dissolution rate changes with varying pH, depth, salinity, and temperature. Once the dissolution rate is reached, the model calculates the number of years it will take for the given shell material to dissolve. As the shell dissolves, the model uses the changing ratios of dissolved bicarbonate molecules to find the changing pH. With increasing pH, it calculates the changing K'_{sp}, Ω, and the changing dissolution rate. We were also able to calculate the amount of pH change a dissolving shell would cause, as well as the number of years it would take to see this change.

All historical data analysis and modeling were done using Matlab version R2015a.

RESULTS

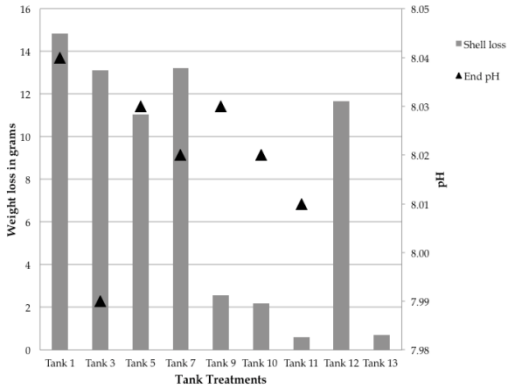

Fig. 1. Shell loss (gray bars) and final pH (triangles) after the 30-day period.

Mitigation of estuarine acidification via reintroduction of spent oyster and clam shells is largely based on an untested hypothesis that calcite addition would act to elevate water column pH levels. The actual success of such an addition is likely impacted by a number of variables, e.g., water quality, nutrient loading, degree of water column turbulence, retention times, physico-chemical characteristics, biological processes at sediment-water interface, rates of calcium removal. Here we initiated a study that addresses these variables in a more quantitative manner by estimating aragonite and calcite dissolution rates in both natural and experimental systems, and analyze how dissolution rates and ambient pH values might change as a function of these variables. Within the experimental treatments, high weight loss (on average 7.8±1.54 g per tank) did not necessarily equate to a large shift in pH (Fig. 1). In terms of individual variables, the most shell weight loss was seen in systems with whole oyster shells and no sediment, which lost, on average, 12.78 g per tank. Shells in tanks with sediment lost very little weight, only 2.38 g per tank (Fig. 1), which is outside the range of weight loss observed in tanks that contained water only. Surprisingly, weight loss was lowest in treatments with crushed oyster shells, only 0.65 g per tank. There was no noticeable difference in weight loss with the addition of flow. Interestingly, pH increased in all tanks, regardless of the presence or absence of oyster shells (Fig. 2 and 3). This begs the question of why the variables had little to no influence on the dissolution rate, and as to why a relatively high dissolution rate did not have a similar effect on pH.

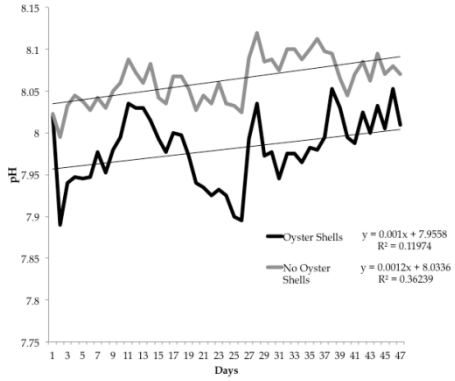

Fig. 2. pH change over time with (gray line) and without (black line) the addition of oyster shells.

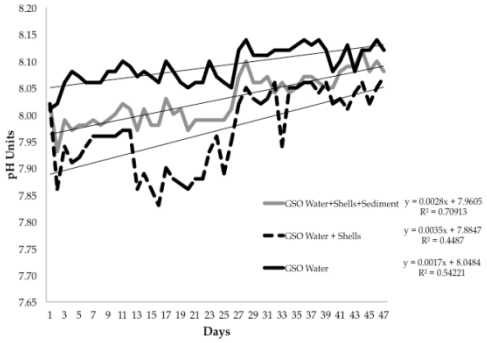

Fig. 3. pH change over time with the addition of sediment and shells (gray line). The gray dotted line is pH change in water only, the black dotted line is change in water with shells.

Using historical data, pH values above ~ 7.8 led to an increase in dissolved calcium carbonate (Fig. 4). The pH time series data were relatively noisy and this led to a fluctuating historical dissolution rate (Fig. 5 and 6). The pH data set also included a large outlier in the year 2010, caused by an algal

bloom and fish die off within Greenwich Bay (Fig. 5). The basic model components showed that, as the amount of oyster shell dissolves, the pH increases, so that when the shell is totally dissolved, the pH becomes stagnant at a value of 8.08 (Fig. 7, 8, and 9). This model is for one shell in a liter of water under "perfect" conditions, and does not take into account biota, sediment, flow, or water circulation.

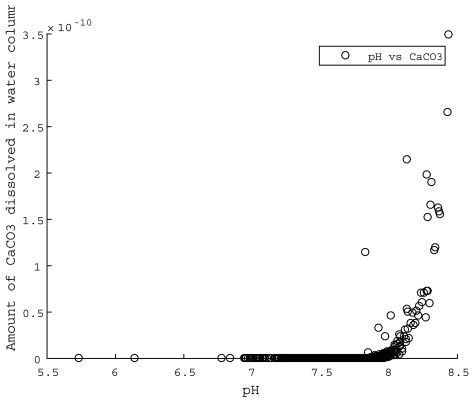

Fig. 4. Relationship between dissolved calcium carbonate and pH, based on historical data from Narragansett Bay.

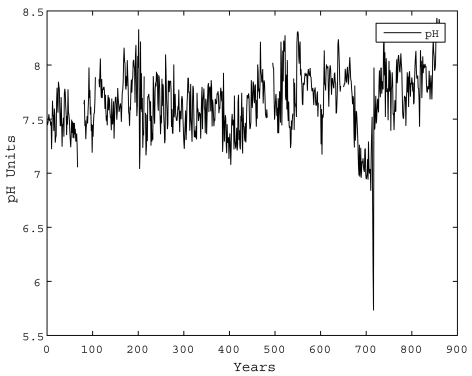

Fig. 5. pH change over time period 2004-2012, from historical data in Greenwich Bay.

DISCUSSION

The purpose of this experiment was to better understand the relationship between pH change and calcium carbonate dissolution, as well as the effects that outside variables, such as water quality, the presence of sediment, and the addition of flow might have on dissolution rate. In previous research, it has been noted that shells dissolve differently under different pH levels (Waldbusser, et al. 2011). It has also been shown that increased acidity negatively affects a larval oyster's ability to calcify in the under saturated waters (Miller et al. 2009). However, the effects of oyster shell dissolution on pH, and the effects of complex variables, such as might be found within estuarine waters, on dissolution rate, have not been studied.

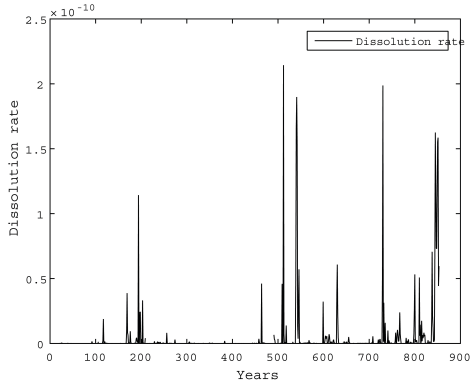

Fig. 6. Relationship between dissolved calcium carbonate and pH, based on historical data from Narragansett Bay.

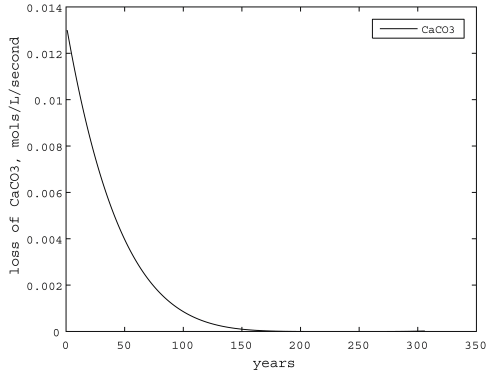

Fig. 7. Model prediction of $CaCO_3$ dissolution over time with preset rate constant assuming ambient pH of 7.00.

Through analysis of historical data and the implementation of some basic mathematical model components, it was found that as

dissolved calcium carbonate content increases, pH increases. Through experimental measurements, we found that the addition of sediment (treatments 9 and 10) lowered shell weight loss, that crushing the shells (treatment 11) lowered weight loss, and that the addition of flow had little to no effect.

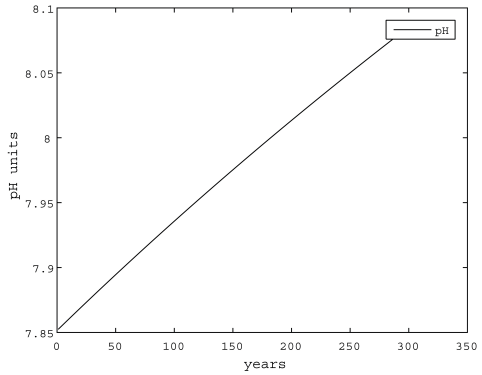

Fig. 8. Model prediction of pH change over time as a function of calcite dissolution.

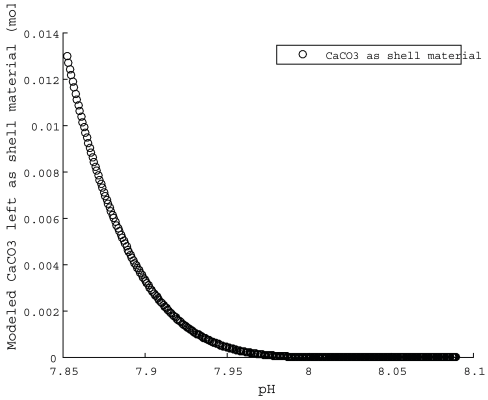

Fig. 9. Model prediction of residual CaCO3 shell material as a function of ambient pH.

The small change in experimental pH could be due to the short sampling period (30 days) or caused by other chemical reactions within the tanks. In addition, the effects of biological phenomena, such as primary productivity or microbial activity, were not studied. In future studies, light and aeration should be used to simulate conditions of growth.

Though pH change was small, there was high dissolution in treatments with whole oyster shells. There was comparatively low dissolution in tanks with sediment or tanks with crushed oyster shells. This could be caused by the super saturation of calcite and aragonite within organic sediments. Though previous research has shown increased dissolution in the presence of sediment due to biota interactions, dissolution in sediment without these biological activities has not been thoroughly studied (Aller, 1982) and should be included in further experimentation. There was no significant difference in pH or dissolution along the gradient in water quality. There was also no significant difference in dissolution between treatments with and without flowing seawater. Therefore, oysters could be placed at any location within a water column without being greatly affected by the changing water quality or flow rate. Furthermore placing oyster shells in hypoxic areas should not significantly help or hinder dissolution.

The model predicted that it would take 306 years for a single oyster shell (44 g) to dissolve under a pH value of 7 and a salinity of 28. However, this rate is much lower than the dissolution construed from the experimental data, partially because the model does not take into account any variables outside of the mathematical relationship of decreasing calcium carbonate and increasing Ca^{++} and HCO_3. As an effect of this, more complex physical and bio-chemical relationships are not accounted for. Future model components, accounting for the effects of additional variables, could predict pH and dissolution rate changes not seen within this experiment.

The analysis of the historical data supports the hypothesis that there is a positive relationship between dissolution rate and pH. As historical levels of dissolved bicarbonates have increased (suggesting a higher dissolution of these compounds), pH has increased. Because the model supports

this relationship as well, and an increase in pH was observed in treatments, it can be suggested that as oyster shells dissolve, there is an increase in pH. However, to gain a better understanding of how prominent this increase is, both temporally and spatially, more direct work with replicates needs to be done, in terms of evaluating outside conditions that could affect the dissolution rate and pH.

CONCLUSION

We studied the relationship between calcite dissolution rate and pH under different environmental conditions, as well as within historical data and through the development of a mathematical model. Dissolution rates were highest in treatments with water only and they were not enhanced by the presence of sediment, water flow, increased surface area, or hypoxia. Both model prediction and analysis of historical data showed that as the amount of dissolved calcium carbonate increased, the pH of the water column also increased. This increase in pH suggests that the addition of calcium carbonate, in the form of oyster shell reintroduction, is an appropriate measure to mitigate local estuarine acidification. More experimental and model studies need to be implemented to better understand how the effects of biological activities, such as primary productivity, might affect dissolution rate.

ACKNOWLEDGEMENTS

The SURFO program is funded by the National Science Foundation. This research was funded by the Rhode Island Sea Grant and the National Science Foundation. Special thanks to Heather Stoffel, for use of analytical equipment and, along with the RI Department of Environmental Management, for providing water quality data for Narragansett Bay, Stephen Granger, for assistance in water and sediment sample collection in Greenwich Bay, Edward Baker for assistance and use of the facilities in the Aquarium Building at the URI Bay Campus, and Jeff Mercer, for quahog density data in Greenwich Bay. Spent oyster shells were kindly provided by the Matunuck Oyster bar.

REFERENCES

Aller, R. “Carbonate Dissolution in Nearshore Terrigenous Muds: The Role of Physical and Biological Reworking.” *The Journal of Geology* 90, no. 1 (January 1982): 79–95.

Cygler, A. *Sector Management Plan for the Shellfish Fishery*, 2014.

Dame, R. *Ecology of Marine Bivalves: An Ecosystem Approach, Second Edition*. Second. CRC Press, 2012.

Doney, S. C., V. J. Fabry, R. A. Feely, and J. A. Kleypas. “Ocean Acidification: The Other CO2 Problem.” *Annual Review of Marine Science* 1, no. 1 (January 1, 2009):169–92. doi:10.1146/annurev.marine.010908.163834.

Miller, A. W., A. C. Reynolds, C. Sobrino, and G. F. Riedel. “Shellfish Face Uncertain Future in High CO2 World: Influence of Acidification on Oyster Larvae Calcification and Growth in Estuaries.” *PLoS ONE* 4, no. 5 (May 27, 2009): e5661. doi:10.1371/journal.pone.0005661.

Morse, J. W., R. S. Arvidson, and A. Lüttge. “Calcium Carbonate Formation and Dissolution.” *Chemical Reviews* 107, no. 2 (February 1, 2007): 342–81. doi:10.1021/cr050358j.

Ringwood, A. H., and C. J. Keppler. “Water Quality Variation and Clam Growth: Is pH Really a Non-Issue in Estuaries?”

Estuaries 25 no. 5 (October 1, 2002): 901–7. doi:10.1007/BF02691338.

Salisbury, J., M Green, C. Hunt, and J. Campell. "Coastal Acidification by Rivers: A Threat to Shellfish?" *Eos* 89, no. 50 (December 9, 2008): 513–28. doi:10.1029/2008EO500001.

Schulz, H. D., and M. Zabel. *Marine Geochemistry*. Springer Berlin Heidelberg, 2013. https://books.google.com/books?id=g4bnCAAAQBAJ.

Turner, C.. "Verification of pH Fluctuations in Narragansett Bay" Open Access Master's Theses, no. Paper 526 (2015). http://digitalcommons.uri.edu/theses/526.

Van Heuven, S., D. Pierrot, J. W. B. Rae, E. Lewis, and D. W. R. Wallace. 2011. MATLAB Program Developed for CO2 System Calculations. ORNL/CDIAC-105b. Carbon Dioxide Information Analysis Center, Oak Ridge National Laboratory, U.S. Department of Energy, Oak Ridge, Tennessee. doi: 10.3334/CDIAC/otg.CO2SYS_MATLAB_v1.1

Waldbusser, George G., Ryan A. Steenson, and Mark A. Green. "Oyster Shell Dissolution Rates in Estuarine Waters: Effects of pH and Shell Legacy." *Journal of Shellfish Research* 30, no. 3 (December 1, 2011): 659–69. doi:10.2983/035.030.0308.

J. Hogan is in the Marine Science Department, University of South Carolina, Columbia SC, USA (jhogan@email.sc.edu)
S. Miller (sabrina_miller@my.uri.edu)
Anton Post (anton_post@uri.edu

Growth and maturity of Narragansett Bay black sea bass, *Centropristis striata*

Connor Jones, Mary Kane, Anna Malek, Conor McManus, and Jeremy Collie
Graduate School of Oceanography, University of Rhode Island, Narragansett RI, 02882

Abstract

Black sea bass (*Centropristis striata*) inhabit the continental shelf along the east coast of the United States from the Gulf of Maine to the Florida Keys. This rockfish species grows up to 60 cm in length and is targeted by commercial and recreational fisheries. Black sea bass are protogynous hermaphrodites, transitioning from female to male as they grow and mature. Little is known about when this sexual transition occurs, particularly in southern New England waters. To address this uncertainty, a total of 96 black sea bass, ranging in size from 21 cm to 45.5 cm, were collected from Narragansett Bay during the months of June and July 2015. Of these fish, 30 were male and 66 were female. We recorded length (cm), weight (kg), sex, sexual maturity (immature, developing, ripe, spent), gonad length (mm), gonad weight (g), and age of each fish based on scales and otoliths to determine the size-at-age, and size/age at sexual maturity relationships for black sea bass in southern New England. Mature (ripe) males and females were found in almost every size and age class collected. A quantitative relationship was established between length and weight. Length-versus-age data were fitted with a von Bertalanffy curve to create a growth model for the Narragansett Bay black sea bass population. We compared our results with literature and NOAA black sea bass growth, maturity, and sexual transition data from other regions and decades. Our data are similar to NOAA data (4,221 fish) in terms of weight-versus-length comparisons and size-at-age.

Narragansett Bay (NB) is home to many facultative and obligate estuarine-dependent fish species, including scup, summer flounder, winter flounder, and black sea bass (Collie et al. 2008). Black sea bass (*Centropristis striata*) are fairly new to the Bay, only showing up in the Graduate School of Oceanography (GSO) Weekly Fish Trawl in significant numbers within the last decade or so (Fig. 1). Current research suggests that there are two distinct populations of black sea bass; one inhabiting the Gulf of Mexico, and the other living along the east coast of the United States. The east coast population can be divided into northern and southern subpopulations. These subpopulations were first believed to be ecological and reproductively identical, but recent work by Roy et al. (2012) suggests that the southern and northern black sea bass stocks are significantly different.

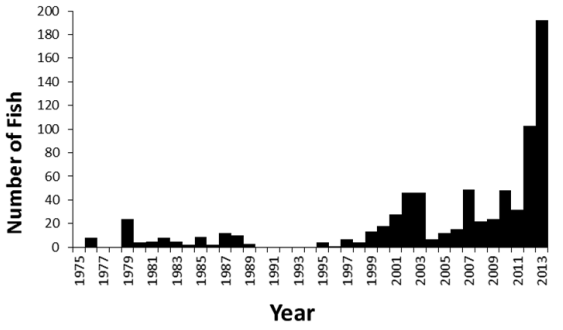

Fig. 1. Number of black sea bass caught per year, in Narragansett Bay for the GSO Fish Trawl Survey.

The two subpopulations are separated by Cape Hatteras off North Carolina (Roy et al. 2012). The increase in black sea bass abundance in Rhode Island waters is thought

to be due to warming water temperature associated with global climate change (Roy et al 2012). The center of biomass is located in more southern waters; however, larger fish have been found to move north to colder and deeper waters (Bell et al. 2014). The northern subpopulation of black sea bass has an upper lethal temperature threshold of 33.7°C and a lower limit of 2.8°C with optimal growth occurring at 25.7°C. Thus as water temperatures warm, black sea bass must move farther north to find their thermal niche, and ideally their optimal growth temperature (Sullivan and Tomasso 2010).

Black sea bass are demersal predatory fish that can grow to be 600 mm in length (Bigelow et al 2002). Their diet includes small fish, squid, mollusks and crustaceans (Roy et al. 2012). Black sea bass are protogynous hermaphrodites, meaning that they are born as females and have the ability to transition to males at some point in their lives. However, small, young males have been observed, suggesting that some black sea bass may be born male. It is possible, however, that these small males are just cases of misidentification (Wuenschel et al. 2011). It has been suggested that the transition from female to male is triggered by visual cues (Benton and Berlinsky 2006). If the dominant male dies or is removed from an area, a female will change sex and replace it (Benton and Berlinsky 2006). Males are usually greater than 240 mm, with an age of at least five years. Females will have reached sexual maturity by the time they are 182 mm and three years of age, but there are some that mature at 100 mm when they are less than one year old (McGovern et al. 2002). Male and female black sea bass both transition through distinct maturity stages as they grow. Females start out as immature, followed by developing, ripe, spent and resting. Under the right circumstances, a female will enter a transitional stage after resting. After the transitional stage, the now male fish will go from resting to developing to ripe to spent (Klibansky and Klibansky). Most fish going through the transition are three years old (Waltz et al. 1979).

Given their nature as a popular sport and commercial species there is concern that black sea bass may be overfished. Based on a 2011 stock assessment by the Northeast Fisheries Science Center (NEFSC), the northeastern Atlantic stock was determined to be neither overfished nor experiencing overfishing (NEFSC 2011). Little is known about the population of black sea bass that resides in Narragansett Bay, yet it is fished both commercially and recreationally. To avoid overfishing of this population, data need to be collected with a special emphasis on their unique life history.

We collected black sea bass in order to determine at what size and age individuals are likely to transition from males to females. We also sought to determine the makeup of the population in the Bay in terms of sex ratios and size ranges. This information would be used in making management decisions about the specific stock of black sea bass in Narragansett Bay.

METHODS AND MATERIALS

Obtaining the specimens – Black sea bass used for this study were obtained from the University of Rhode Island GSO's Fish Trawl Survey, the Rhode Island Department of Environmental Management (RI DEM) trawl survey and the RI DEM ventless trap survey. The GSO Fish Trawl was conducted weekly during June and July, 2015 on the R/V *Cap'n Bert*. Two stations were sampled in the west passage of Narragansett Bay: Fox Island and Whale Rock. Fox Island is located in the central part of the west passage, just outside of Wickford Harbor, whereas Whale Rock is located at the mouth of the Bay. The GSO standardized otter

trawls were conducted for 30 min at a speed of 2 knots. The DEM trawls were conducted from July 13th to July 17th, 2015 on the R/V *John H. Chafee*. DEM trawl sites in the Bay were a mix of fixed and randomly chosen sites. DEM trawls were conducted for 20 min at each station (Olszewski 2015). The RI DEM ventless trap survey aims to assess the lobster populations in state waters and deploys both vented and unvented lobster traps that capture a variety of species. The black sea bass collected for this study were caught in RI DEM traps around Block Island on July 17th, 2015. A total of 96 black sea bass were collected for this study.

Data on an additional 4,221 black sea bass were provided by the NOAA Northeast Fisheries Science Center. These black sea bass were caught during spring and fall bottom trawl surveys conducted across the continental shelf between Cape Hatteras and the Gulf of Maine. Biological black sea bass data from 2005 to 2014 were used in this study.

Laboratory Analysis – After collection, fish were taken back to the lab for processing. Total fish length was measured to the nearest 0.5 cm and weighed to the nearest 0.005 kg. A photograph was taken of each fish with an identification card, with the fish positioned so its left side was facing the camera. Fish were then repositioned so that a photograph could be taken of just their head in order to analyze visual differences between males and females. Images were later analyzed for any color, size or shape differences that could be used to determine differences between males and females.

The sex of each fish was predicted based on external characteristics before dissecting the specimen. Gonads were then removed to validate/disprove the visual sex assignment and identify their maturity stage. Gonads were weighed to the nearest 0.001 g and measured in length to the nearest 0.1 mm. Life stages for the specimens were assigned based on the categorizations described in Klibansky and Klibansky.

Aging – Ages were estimated for all fish based on both scales and otoliths. Two to three scales were removed from the left side of each fish, approximately six rows of scales behind the pectoral fins, and then preserved in ethanol. The scales were analyzed by counting the number of annuli seen under a dissecting microscope. Annuli were counted as bands that spanned the middle section of the scale. To be considered a true annual ring, the bands had to be either darker or lighter than the surrounding scale. Otoliths were removed and preserved in ethanol for annuli readings under the dissecting microscope. Otolith annuli were easier to discern than scale annuli. Annuli for both scales and otoliths were counted by two people independently to ensure accuracy of age estimates.

Data analysis – Length-at-age functions were created for the data generated by this work as well as NOAA's black sea bass data. We used otolith ages whereas NOAA used a combination of scales and otoliths. Age-length relationships were described using the von Bertalanffy growth curves in Excel and the Solver add-in. Solver calculates the best fitting parameter values by solving for the least sum of squares. We then obtained a growth rate for our data using the maximum length and t_0 from the NOAA data. Weight-versus-length data were plotted for both data sets. Length and weight data were then log transformed and fitted with a linear regression. The slope and y-intercept were used to create a relationship between weight and length for both data sets:

$$w = A \times L^b$$

where w is fish weight (kg), L is fish length (cm), A and b are coefficients. To obtain A and b, the weight-versus-length relationship was converted to:

$$\log w = \log A + b \log L$$

A linear regression was then fitted to the data. $\log A$ is the y-intercept and b is the slope of the linear trend line of the log transformed data:

$$w = 10^{\log A} \times L^b$$

We then fit the data with a von Bertalanffy Growth Curve:

$$L_t = L_\infty(1 - e^{-k(t-t_0)})$$

where L_t = the length of a fish at a given age t, L_∞ is the asymptotic length of the fish species, k is the "curvature parameter" or how fast the fish approaches L_∞, t is the age in years of the fish, and t_0 is the theoretical age at which the fish has zero length.

RESULTS

Of the 96 fish we dissected, 30 were male and 66 were female. Of the 30 male fish, 4 were classified as cryptic males. They all fell into three sexual maturity categories: Developing, Ripe and Spent (Fig. 2). Of the 4,221 fish data from NOAA, 1,010 were male, 2,622 were female and 589 were unsexed/unknown/not observed.

von Bertalanffy growth curve – The fish we collected were between the ages of one and four years old, with the majority being two to three years old. NOAA collected data from fish that were 0 to 12 years old. This wider range in ages of the NOAA data gave a better estimate for L_∞ and t_0. L_∞ for the NOAA data was calculated to be 70.7 cm, t_0 was estimated to be -0.737 cm, and k, was estimated to be 0.150 per year. Using the L_∞ and t_0 values from the NOAA data, we obtained a higher growth rate for our fish, with k estimated to be 0.202 per year.

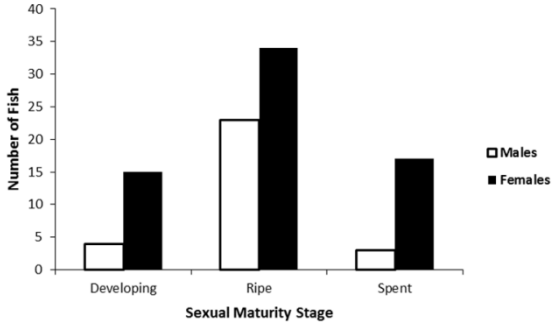

Fig. 2. Frequency of developing, ripe, and spent sexual maturity stages in the 96 black sea bass (*C. striata*) examined for this study. Black bars are female fish, white bars are male fish. Only three different maturity stages were observed for males and females.

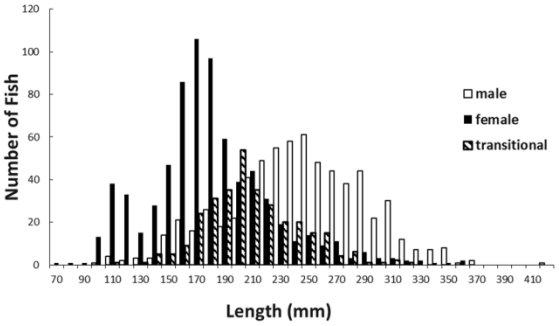

Fig. 3. Number of black sea bass per length class for data from Waltz et al. (1979). Black bars are females, white bars are males and striped bars are transitional fish. Sample size: 2,215 fish

Length frequencies – The number of females, males and transitional fish were classified by size category similar to Waltz et al. 1979 (Fig. 3). Males tend to be found more frequently at longer lengths, the largest fish we caught was a male (455 mm). However, a few of the males were quite small, including the smallest fish we caught (210 mm). Some of these smaller males

were classified as cryptic males based on their lack of external male characteristics. The four cryptic males were 210, 280, 285 and 345 mm in length. Males in our study peaked in abundance between 370 – 380 mm in length, whereas females peaked between 330 – 360 mm (Fig. 4).

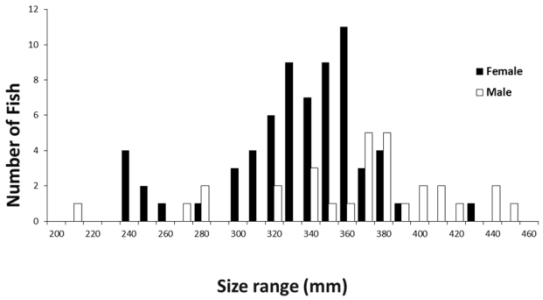

Fig. 4. Number of fish per length class for this study. Black bars are females and white bars are males. Sample size: 96 fish.

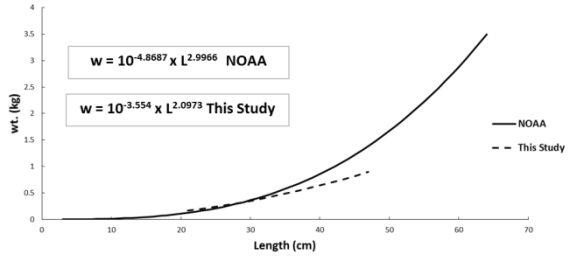

Fig. 5. Weight-versus-length relationships for NB fish data (dashed line, n = 96) and NOAA fish data (solid line, n = 4,221). The equations for each line were calculated from a linear trend line of the log transformed data, for both separate data sets.

Weight – length relationship – Weight (kg) versus length (cm) relationships were found to be $w = 2.79\times10^{-4}\times L^{2.0973}$ and $w = 1.35\times10^{-5}\times L^{2.9966}$ for our data and NOAA's data, respectively. The NOAA data spans a much larger size range, 3 – 64 cm, compared to our 21 – 45.5 cm. Our data follow the same trend as the NOAA fish from about 20 – 30 cm. For fish longer than 30 cm, our curve drops below the NOAA curve, an indication that Narragansett Bay fish are 'light' for their size (Fig. 5).

DISCUSSION

The growth curve (k) for Narragansett Bay fish was slightly higher than that of NOAA's. However, this might not accurately represent the growth trend in Narragansett Bay, nor necessarily support that the population of black sea bass in the Bay is growing faster than fish along the east coast. The most likely reason for this is the limited age range of the fish collected for this study. The ages ranged from 1 to 4 years. NOAA collected fish that ranged in age from 0 to 12 years (Fig. 6). Even within our four-year data range, 81 of the 96 fish were either two or three years old (Fig. 7). These two factors may have skewed the growth curve for the Narragansett Bay fish (Fig. 8). In order to come to a more concrete conclusion, we would need a larger sample size spanning a broader age range.

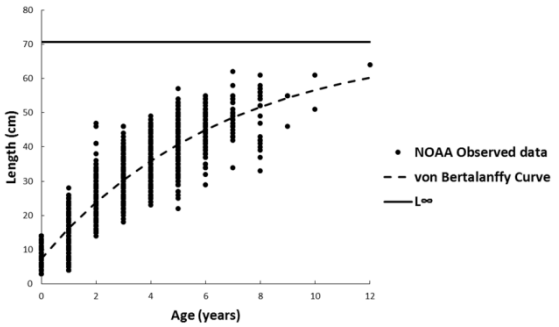

Fig. 6. NOAA length-at-age data (black dots) fitted with a von Bertalanffy Growth Curve (dashed line). The calculated upper size limit for black sea bass is illustrated by the solid black line. Ages based on scale and otolith readings. Sample size: 4,221 fish.

Based on Waltz et al. (1979) we were able to infer that transitional individuals are most abundant at a length that falls in between lengths at which males and females are most abundant. This happened to be 200 mm for

their data (Fig. 3). Our data didn't show peaks that were as distinct so there was a range of lengths that transitional fish might occur, 330 – 380 mm. We did see a distinct difference in the sizes of the Narragansett Bay fish compared to Waltz's. Our fish were generally longer and showed peak abundances at longer lengths (Fig. 4). This could be due to the fact that the fish in Waltz's study came from the southern population along the east coast and our fish are from the north.

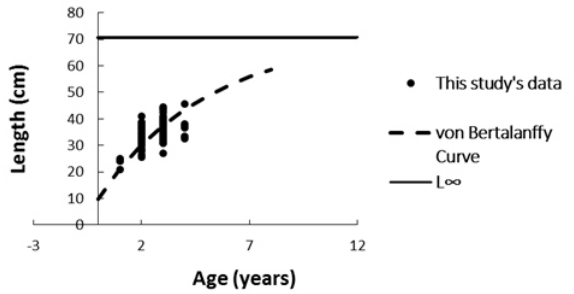

Fig. 7. NB black sea bass length-at-age data (black dots, n = 96) fitted with a von Bertalanffy Growth Curve (dashed line, n = 96). The calculated upper size limit for black sea bass is illustrated by the solid black line. Ages based on otolith readings.

The weight-versus-length relationship for our data was lower than the NOAA data past 30 cm in length (Fig. 5). This seems to contradict the slightly higher growth rate seen in the growth curve of our fish. It could be that our fish are growing faster length-wise than fish off the entire east coast, but they are not putting on as much weight. This could be a result of the colder water temperatures in Narragansett Bay leading to a slower metabolic rate. Rhode Island and Narragansett Bay are at the northern edge of the black sea bass' range, so any fish found farther south would experience warmer water temperatures. The differences could also be due to seasonality. Our fish were caught in the summer when all fish were either getting ready to spawn, spawning or had just recently spawned. NOAA conducted their surveys in the spring and fall when black sea bass are not spawning. It could be that fish in the summer are focusing and expending their energy on reproducing, while in the spring they need to feed more to have the energy to spawn. In the fall they need to focus on feeding in order to prepare for winter (Steimle et al. 1999).

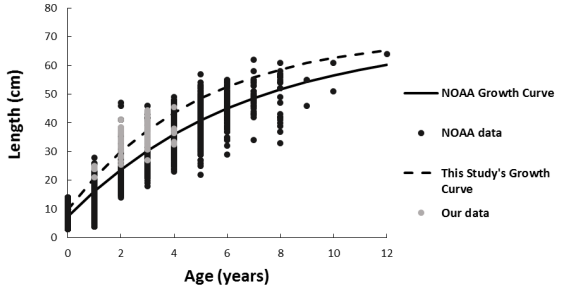

Fig. 8. Comparison of the growth curves for NB's (dashed line, n = 96) and NOAA's (solid line, n = 4,221) black sea bass. NOAA data shown in black dots, our data shown in grey.

There are a number of inherent limitations associated with this study. Aging black sea bass is a subjective process, such that different people may assign a different age to the same fish. The benthic trawls utilized in the study do not sample every possible type of ecosystem. Boats will most likely not trawl over reefs, pilings or rocky bottoms. This can limit the type and number of species sampled. This study would have ideally spanned a much longer period of time, and collected a greater number of specimens.

This study has provided much needed information on the seasonal black sea bass population in Narragansett Bay. If black sea bass continue to be a popular commercial and recreational fish, management protocols will need to be established in order avoid a stock crash. This study shows that it may not

be possible to rely solely on general data and models to assess populations within a specific area. Areas like Narragansett Bay will have their own localized subpopulations that set them apart from fish that are found along the northern half of the east coast. Fisheries regulations developed for Rhode Island will need to account for the life history characteristics of the local subpopulation.

ACKNOWLEDGEMENTS

This study was funded by the National Science Foundation's (NSF) Research Experience for Undergraduates (REU) program. Special thanks to Captain Tom Puckett of the R/V Cap'n Bert for his assistance in collecting black sea bass through the GSO Fish Trawl Survey. We thank Dr. Richard McBride at NOAA Fisheries for providing data. Thank you to Scott Olszewski and Jeff Mercer at the Rhode Island DEM for providing black sea bass from their trawl and ventless trap surveys. We thank the Summer Undergraduate Research Fellowship in Oceanography (SURFO) program and its coordinators: Drs. Lucie Maranda, David Smith and Kathleen Donohue.

REFERENCES

Bell, R., D. Richardson, J. Hare, P. Lynch, and P. Fratantoni. 2014. Disentangling the effects of climate, abundance, and size on the distribution of marine fish: an example based on four stocks from the Northeast US shelf. ICES Journal of Marine Science 72: 1311-1322.

Benton, C., and D. Berlinsky. 2006. Induced sex change in black sea bass. Journal of Fish Biology 69: 1491-1503.

Bigelow, A., W. Schroeder, B. Collette, G. Klein-MacPhee, and H. Bigelow. 2002. Bigelow and Schroeder's fishes of the Gulf of Maine, Smithsonian Institution Press.

Collie, J., A. Wood, and H. Jeffries. 2008. Long-term shifts in the species composition of a coastal fish community. Can. J. Fish. Aquat. Sci. 65: 1352-1365.

Klibansky, N., L. K. J. Klibansky. Black Sea Bass (*Centropristis striata*) Gonad Analysis Manual

McGovern, J., M. Collins, O. Pashuk, and H. Meister. 2002. Temporal and Spatial Differences in Life History Parameters of Black Sea Bass in the Southeastern United States. North American Journal of Fisheries Management 22: 1151-1163.

Northeast Fisheries Science Center (NEFSC). 2011. 53rd Northeast Regional Stock Assessment Workshop (53rd SAW) Assessment Report. US Department of Commerce, Northeast Fish Science Center Reference Document 12-05; 559 p.

Olszewski, S. July 16th, 2015. Rhode Island Coastal Trawl Survey - Coastal Fishery Resource Assessment. RI Division of Fish and Wildlife - Marine Fisheries Section

Roy, E., J. Quattro, and T. Greig. 2012. Genetic Management of Black Sea Bass: Influence of Biogeographic Barriers on Population Structure. Marine and Coastal Fisheries 4: 391-402.

Steimle, F. W., C. A. Zetlin, P. L. Berrien, and S. Chang. 1999. Essential fish habitat source document. Black sea bass, *Centropristis striata*, life history and habitat characteristics. Vol. 143. DIANE Publishing.

Sullivan, M., and J. Tomasso. 2010. Limiting and Optimal Temperatures for the Northern Atlantic Population of Black Sea Bass. North American Journal of Aquaculture 72: 258-260.

Waltz, W., Roumillat, W. A., & Keener-Chavis, P. 1979. Distribution, age structure, and sex composition of the black sea bass, *Centropristis striata*, sampled along the southeastern coast of the United

States. South Carolina Wildlife and Marine Resources Department.

Wuenschel, M. J., Shepherd, G. R., McBride, R. S., Jorgensen, R., Oliveira, K., Robillard, E., & Dayton, J. 2011. Sex and maturity of black sea bass collected in Massachusetts and Rhode Island waters; preliminary results based on macroscopic staging of gonads with a comparison to survey data. Working paper for SARC-53, Black sea bass working group. National Marine Fisheries Service, Woods Hole, MA

C. Jones is at State University of New York at Binghamton, NY (jonesco29@gmail.com)
M. Kane (mkkane@my.uri.edu)
A. Malek (anna_malek@my.uri.edu)
C. McManus (cmcmanus@gso.uri.edu)
J. Collie (jcollie@uri.edu)

Determination and estimation of polyethylene - water equilibrium partition coefficients for organophosphate flame retardants and current-use pesticides

Brittany A. Kerr, Carrie McDonough, Rainer Lohmann
Graduate School of Oceanography University of Rhode Island: Narragansett, RI, USA

Abstract

In order to properly identify and quantify hydrophobic organic chemicals within water samples through passive sampling, the chemical's equilibrium partition coefficient needs to be known. Polyethylene (PE) - water equilibrium partition coefficients (K_{PEw}) were determined empirically and estimated from the literature for six organophosphate flame retardants (OPFRs) and six current-use pesticides (CUPs). The K_{PEw}s were calculated based upon a laboratory study with four variables, including fresh and salt water as well as an amber glass bottle as the control bottle and a clear glass bottle. The coefficients were estimated using literature-based octanol-water equilibrium partition coefficients (K_{ow}) and water solubilities (C_w^{sat}). For most compounds, the estimated K_{PEw} values were upper limits to the calculated values. Although the literature indicates that there should be a relationship between increasing salinity and K_{PEw}, no statistically significant relationship between the two was identifiable for most of the OPFRs and CUPs. Comparison between the K_{PEw} values from the two types of bottles suggests that there is little difference between the two; however, a more in-depth study is suggested. Future work should be analyzing samples that are given more time to reach equilibrium, or to alter the water extraction methodology.

There are many types of organic chemicals contaminating the world's oceans and water sources. Some chemicals are considered persistent, toxic, bioaccumulative, and prone to long-range transport, and are referred to as persistent organic pollutants (POPs). Legacy POPs such as polychlorinated biphenyls (PCBs), which were insulating agents, and the pesticide DDT are studied to determine if reduced emissions have led to reduced concentrations in receiving waters, oceans, and aquatic food chains (Lohmann & Muir 2010). There are other chemicals, however, that are fairly new to the environment and not very well understood. They are referred to as contaminants of emerging concern (CECs). This study focuses on two types of CECs: organophosphate flame retardants (OPFRs) and current-use pesticides (CUPs) (Table 1).

OPFRs were introduced to replace restricted polybrominated diphenyl ethers that were used as brominated flame retardants (Salamova et al. 2014). OPFRs are getting into the environment due to the way in which they are used as flame retardants. They are added to consumer products but are not covalently bonded, so they can easily be released into the environment (Salamova et al. 2014). Today, some OPFRs are banned already whereas others are still used. Tris(1,3-dichloro-2-propyl) phosphate (TDCPP), before it was removed from use for some applications, was found in children's pajamas; however, it was discovered to be mutagenic, harmful to the thyroid, and it has neurotoxic effects (Salamova et al. 2014). 2-ethylhexyl diphenyl phosphate (EHDPP) is currently used in food packaging; however, it may potentially bioaccumulate and could be toxic

Table 1. Studied CUPs, OPFRs (with their abbreviations) and structures (drawn with ChemSketch).

Studied current-use pesticides (CUPs)		**Studied organophosphate flame retardants (OPFRs)**		
Dichlorvos	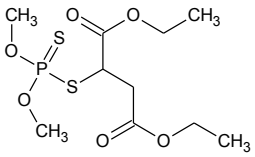	Tri-n-butyl phosphate	TnBP	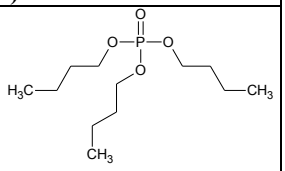
Fenitrothion	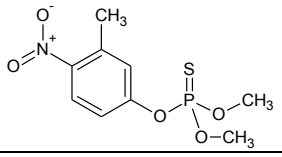	Tris(2-chloroethyl) phosphate	TCEP	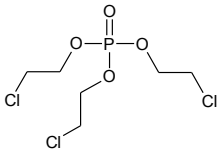
Fipronil	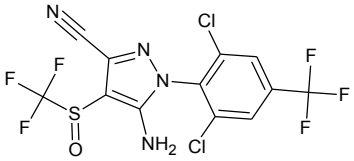	Tris(1-chloro-2-propyl) phosphate	TCPPs	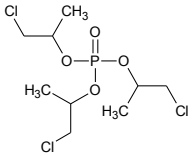
Malathion	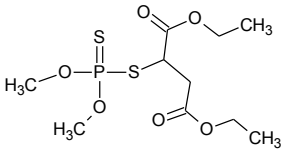	Tris(2-chloropropyl) phosphate		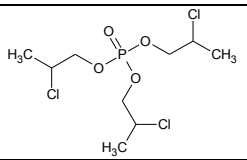
Methoprene	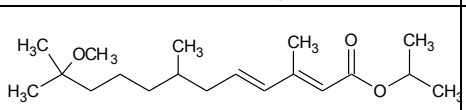	Tris(1,3-dichloro-2-propyl) phosphate	TDCPP	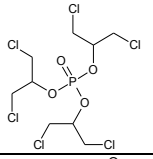
Resmethrin	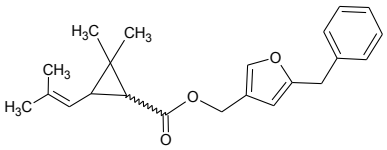	Triphenyl phosphate	TPP	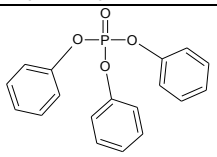
		2-ethylhexyl diphenyl phosphate	EHDPP	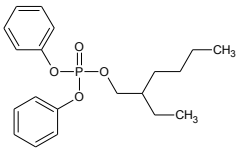

to fish and other aquatic species (Salamova et al. 2014).

CUPs are used for a range of reasons. Some, like Malathion and Methoprene, have a history of use to control the West Nile virus, especially in New York in 1999 (McElroy et al. 2005), whereas others, such as Fipronil, are currently used as main ingredients in brand-name flea and tick killing medicine for pets (http://www.frontline.com/Pages/About.asp x#what-is-it last accessed August 8, 2015). Since CUPs are released directly to the environment in some cases, runoff from areas where they are used eventually leaches into larger bodies of water, supplementing global water with the potentially harmful pesticides. It is thought that the large-quantity uses of some pesticides have created unintended problems for the environment, such as lobster population decreases (McElroy et al. 2005).

Table 2. OPFRs' and CUPs' standard solution concentration with quantity added to the laboratory study stock solution.

OPFR and CUP concentration and required volume for stock solution					
Compound	**CAS**	**Current concentration**	**(units)**	**Vol to add to stock**	**(units)**
TnBP + TPP	126-73-8 , 115-86-8	1000	ng/μL	50	μL
TCEP	115-96-8	50	ng/μL	100	μL
T1CPP	13674-84-5	50	ng/μL	100	μL
T2CPP	6145-73-9	50	ng/μL	100	μL
TDCPP	13674-87-8	50	ng/μL	100	μL
EHDPP	1241-94-7	1000	ng/μL	50	μL
Dichlorvos	62-73-7	1000	μg/mL	50	μL
Fenitrothion	122-14-5	100	μg/mL	200	μL
Fipronil	120068-37-3	100	μg/mL	200	μL
Malathion	121-75-5	1000	μg/mL	50	μL
Methoprene	40596-69-8	100	μg/mL	200	μL
Resmethrin	10453-86-8	100	μg/mL	200	μL

To better understand the fate and effects that may arise from the use of OPFRs and CUPs, it is critical that researchers gain a better understanding of their concentration in water sources.

Passive sampling is an increasingly popular process in the field to measure concentrations of CECs. Passive samplers are made up of an organic material that has similar characteristics to organic pollutants in order to accumulate the pollutants present in water or air (Lohmann & Muir 2010). Since most POPs and CECs are hydrophobic and organic, polyethylene (PE) is widely used as the sampling material because it is also hydrophobic and organic and has a nonpolar structure (Sacks & Lohmann 2011).

Concentrations of pollutants in PE can be used to estimate concentrations in water; however, this is possible only when equilibrium is reached for the pollutants within the PE and the water, or when the percent equilibration reached during deployment can be estimated (Adams et al. 2007, Sacks & Lohmann 2011). To determine the pollutant concentration in the water, Equation 1 is commonly used,

$$C_w = \frac{C_{PE}}{K_{PEw}} \qquad (1)$$

where C_w (ng/L) represents the concentration of the pollutant in the water at equilibrium, C_{PE} (ng/L) represents the concentration of the pollutant in the PE at equilibrium, and K_{PEw} is the equilibrium partition coefficient between PE and water (Adams et al. 2007, Lohmann & Muir 2010, Lohmann 2011, Sacks & Lohmann 2011). The purpose of this study is to determine the equilibrium partition coefficient for each OPFR and CUP listed in Table 1. The K_{PEw} could then be applied in field research where C_{PE} is determined from sampling to calculate C_w for these pollutants.

METHODS AND MATERIALS

Pollutant stock solution – The stock solution was made up of 12 pollutants. Six were OPFRs and six were CUPs (Table 1). A

specified volume of each OPFR and CUP was added to a solvent-rinsed 2-mL volumetric flask (Table 2). The volumes were determined based on concentration of individual stock solutions, desired final concentration, volume available, and likelihood of a low or high strength K_{PEw}. Once all pollutants were added, the flask was topped off with methylene chloride (Fisher Scientific). The stock solution was transferred into a 2-mL amber vial.

Water solution preparation – Each of 30 solvent-rinsed 120-mL amber bottles received 50 µL of the stock solution. The liquid was allowed time to evaporate (usually ranging between 3 and 5 minutes) within the bottle. After all bottles were ready, 100 mL Milli-Q water was added to the bottle. The bottles sat in the hood for 72 hours to allow the evaporated stock solution to dissolve in the water. Three additional bottles were used to verify the amount of stock solution that dissolved into the water in the 72-hour time period.

Sample bottle preparation – Spiked water solution from the above bottles was transferred to solvent-rinsed, numbered bottles: twelve bottles were 120-mL amber bottles, and two of them were clear 120-mL glass bottles (refer to Table 2). Aluminum foil was placed under the cap before closing. The ionic strength in three of the 14 bottles was altered to have salinity values of 20‰ and another three to a salinity of 30‰ by adding 2 or 3 g of Instant Ocean® sea salt per 100 mL of water, respectively.

Polyethylene samplers – PE (50-μm thickness) was cut (3.5 x 3.5 cm) and numbered according to the bottle it would be sampling. All PE samplers were weighed (Table 3), and two metal rings were attached to act as anchors during deployment. The samples were left to equilibrate for three weeks on a shaking table. For this study, it was assumed that equilibrium had been reached during the three-week shaking time period.

Table 3. Variables for each bottle along with the mass of the PE (g) into the bottle.

Sample descriptors		
Bottle	**Variables**	**PE Mass**
1	Blank	0.0651
2	Blank	0.0640
3	Blank	0.0648
7	Amber bottle	0.0643
8	Amber bottle	0.0599
9	Amber bottle	0.0605
13	30.9 ‰ salinity	0.0588
14	32.6 ‰ salinity	0.0590
15	31.4 ‰ salinity	0.0583
19	20.4 ‰ salinity	0.0621
20	20.6 ‰ salinity	0.0611
21	20.3 ‰ salinity	0.0621
28	Clear bottle	0.0548
29	Clear bottle	0.0590
31	Spiked water test	-
32	Spiked water test	-
33	Spiked water test	-

Polyethylene extraction

After the three-week shaking period, the PE was removed from the bottles and extracted for 24 hours with n-hexane (Fischer Scientific). The extract was concentrated down to 0.5 mL using an evaporator (Biotage Turbovap II, 6 psi, 35°C) and further concentrated to <0.5 mL with streamed nitrogen gas.

Water extraction – The water was also extracted for 24 hours after the three-week shaking period according to modified EPA Method 505, where section 11.2 was the main focus. Na_2SO_4 was used, instead of NaCl, to absorb water that may have been

removed from the sample with the hexane, and volumes of 20-mL sample water with 5 mL hexane were used per sample. The extract was concentrated down to a smaller volume with the same process as the PE sample extracts.

Analysis – Samples were analyzed by gas chromatography/mass spectrometry (GC/MS). An Agilent 6890 series GC system coupled with 5973 network Mass Selective detector was used along with a 7683 series injector. An Agilent J&W GC column was used with the following: 122-5532 DB-5ms, 30-m length, 250-μm diameter, and 0.25-μm film. Injection was splitless at 275 °C with 18.97 psi, electron-impact (EI) ionization was set in selected-ion-monitoring (SIM) mode. The GC temperature method began at 90 °C and was held for 3 min, then increased 10 °C/min until a temperature of 200 °C was reached, then increased 5 °C/min to a final temperature of 315 °C with no end hold time. Total run time was 47 min. Injection was 1 μL, and the helium carrier gas flow remained at 1.9 mL/min.

Table 4. Amount of OPFRs and CUPs recovered from PE and water samples compared to amount added into the stock solution as represented by percent recovery.

	Amount Recovered			Amount Added	
	from PE (ng)	**from Water (ng)**	**Total**	**to Stock (ng)**	**% Recovery**
TnBP	166.17	533.42	699.59	12,500	6%
TCEP	20.25	20.08	40.33	5,000	1%
TCPPs	97.54	32.94	130.48	20,000	1%
TDCPP	1,078.35	177.73	1,256.08	5,000	25%
TPP	844.76	538.15	1,382.91	12,500	11%
EHDPP	5,039.13	61.50	5,100.63	50,000	10%
Dichlorvos	1,718.83	0.00	1,718.83	50,000	3%
Fenitrothion	115.38	320.52	435.90	20,000	2%
Fipronil	16.96	5.68	22.64	20,000	0%
Malathion	6.68	39.85	46.53	50,000	0%
Methoprene	1,332.43	197.20	1,529.63	20,000	8%
Resmethrin	2,686.39	73.69	2,760.08	20,000	14%

Quality control – Several quality control measures were taken to assess the efficiency of the extraction process and assure quality of the data. A TnBP-d_{27} and TPP-d_{15} OPFR internal standard (4 ng/ μL) and a deuterated Dichlorvos, deuterated Malathion, and ^{13}C Me Triclosan CUP internal standard (1 ng/μL) were added to each sample prior to extraction at volumes of 10 μL and 20 μL, respectively. However, because the analysis method on the GC/MS could not properly identify the CUP internal standard, the OPFR internal standard was used for all comparisons during data analysis. An OPFR matrix spike containing all target analytes was added to Sample #1 at 10 μL to determine the recovery percentage of the pollutants based on the extraction process. This was also evaluated by comparing the amount recovered (in ng) for each pollutant to the amount spiked into the stock solution (Table 4). Recovery ranged from 1% to 67% with most percentages falling within the mid-20s, for both PE extraction and water extraction; however, recovery from the extraction of the water was noticeably lower

(from 1% to 32%) than extraction from the PE. Furthermore, an injection standard made up of p-terphenyl-d_{14} at a volume of 20 μL was added to each sample after the extraction process to monitor instrumental variability. Two calibration curves, one for the OPFRs and one for the CUPs, were used to calculate the amount of each pollutant present within the sample based on the OPFR internal standards. One standard from each calibration curve was analyzed after every 12 samples during GC/MS analysis as a checkpoint.

K_{PEw} estimations – K_{PEw} values were estimated for each OPFR and CUP using two methods: octanol-water equilibrium partition coefficient (K_{ow}) and water solubility (C_w^{sat}) values. Because octanol and PE have similar structures, the partition coefficient for octanol can be related to that of PE for non-polar organic pollutants in which van der Waals forces would be the only interactions for octanol and polyethylene. All K_{ow} values were adopted from chemical databases and used in Equation 2, adopted from Lohmann (2011),

$$logK_{PEw} = 1.14logK_{ow} - 1.14 \quad (2)$$

to calculate K_{PEw}. For organic pollutants that have functional groups and more than van der Waals interactions (except for pollutants with hydrogen donation capabilities), water solubility can be used to predict K_{PEw}. All C_w^{sat} (mol/m^3) values were adopted from chemical databases and used in Equation 3, also adopted from Lohmann (2011), to calculated K_{PEw} for the OPFRs and CUPs.

$$logK_{PEw} = -0.99logC_w^{sat} + 2.39 \quad (3)$$

Effect of salinity on K_{PEw} values – Dissolved salts can affect K_{PEw}s. Using $logK_{PEw}$ calculated from amber bottles containing freshwater and PE, each pollutant's $logK_{PEw}$ ($logK_{sw}$ in the equation) was calculated with Equation 4, adopted from Lohmann et al. (2012), where $logK_{sw,0}$ is the freshwater $logK_{PEw}$ value for the pollutant, K_s is the Setschenow constant (taken to be 0.35 L/mol), and I is the ionic strength of the salts present in water. Due to a lack of information on the salt composition of Instant Ocean® sea salt, the ionic strength was calculated assuming NaCl was the dominant salt.

$$logK_{sw} = logK_{sw,0} + K_sI \quad (4)$$

RESULTS AND DISCUSSION

Laboratory K_{PEw} determination – $LogK_{PEw}$ values for the OPFRs ranged from 2.2 for TnBP to 4.3 for EHDPP, where four out of the six OPFRs had $logK_{PEw}$ values between 2.2 and 2.6. Higher $logK_{PEw}$ values, such as 4.3 for EHDPP and 3.7 for TCPP suggest a high affinity for the chemicals to the PE. TnBP and TCEP have similar molecular weights with a difference of 20 g/mol and also had similar $logK_{PEw}$ values: 2.2 and 2.3, respectively. Though TDCPP and TPP had similar $logK_{PEw}$ values (2.6 for both), their structures differ, in that TDCPP has two polar chlorines on each of the three branches whereas TPP has three phenyl rings as the three branches off the phosphate group, and they have diverging molecular weights with a difference near 100 g/mol.

Similarly to the OPFR $logK_{PEw}$ values, CUP $logK_{PEw}$ values also displayed a narrow log-value range from 1.2 for Fipronil to 3.2 for Methoprene, where four out of the six CUPs had $logK_{PEw}$ values between 1.2 and 1.8. Lower $logK_{PEw}$ values demonstrate a relatively higher affinity of the chemicals for water. The four CUPs with low $logK_{PEw}$ values had a wider range of functional groups within their structures (i.e. additional chlorines in Dichlorvos, sulfur and nitrogroup in Fenitrothion, additional fluorine and an amine group in Fipronil, and

sulfur in Malathion) than the two CUPs with higher $\log K_{PEw}$ values. Methoprene had a $\log K_{PEw}$ value of 3.2, and its structure is a long carbon chain with an ester at one end of the chain and ether at the other. Resmethrin also has a carbon chain structure; however it has three rings within the structure and had a lower $\log K_{PEw}$ value of 2.6 compared to Methoprene (3.2).

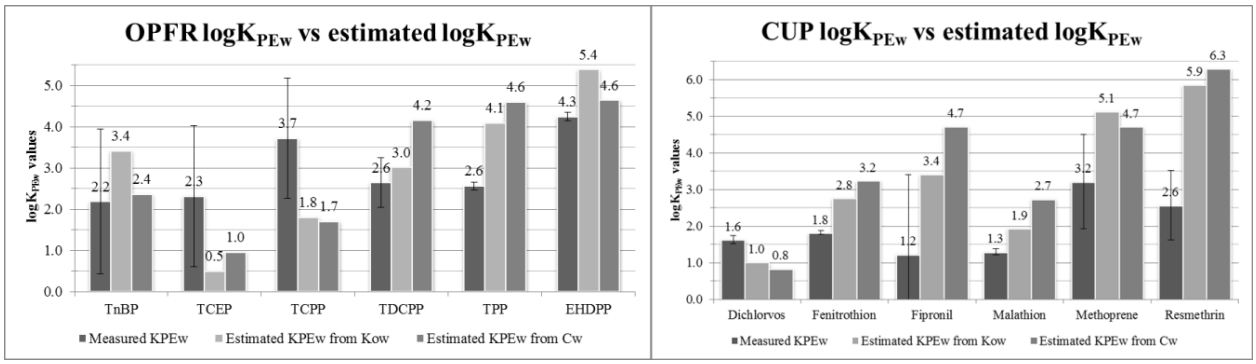

Fig. 1. K_{PEw} values calculated from the laboratory study versus the K_{PEw} values estimated from both K_{ow} and water solubility (C_w).

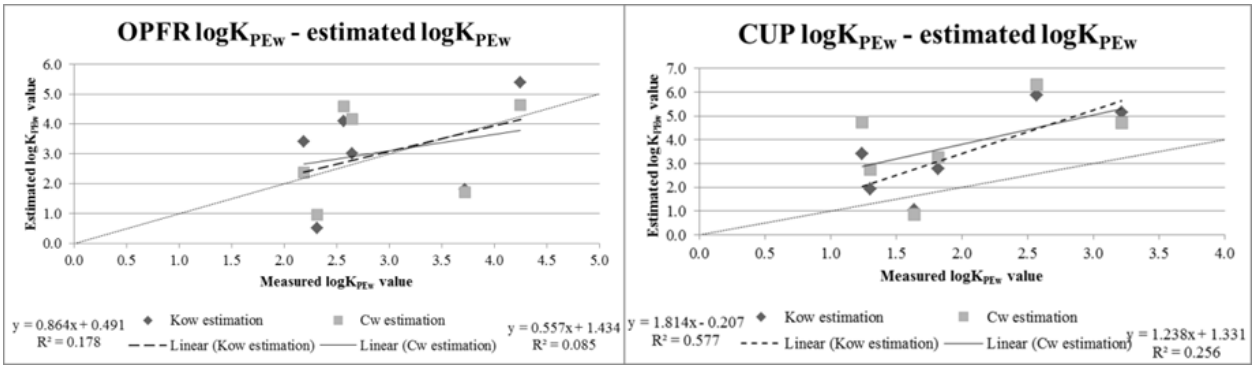

Fig. 2. Laboratory-derived K_{PEw} values versus estimated K_{PEw} values for K_{ow}- and C_w-based estimation methods.

Comparison of measured and estimated K_{PEw}s – Because the OPFRs had fewer functional groups and displayed more non-polar characteristics compared to the CUPs, it was expected that the K_{ow} estimations would be more similar to the observed K_{PEw}s than the C_w^{sat} estimations would be to the observed K_{PEw}s. It was also expected that the C_w^{sat} estimations would be similar to the observed K_{PEw}s for the CUPs rather than the K_{ow} estimations would have been since the CUPs display additional polar characteristics and functional groups within their structures.

To test these expectations, laboratory $\log K_{PEw}$ values were compared to estimated values, which were found to be significantly different. Generally, for both the OPFRs and the CUPs, the estimation based on $\log K_{ow}$ values had a larger difference than the estimation from C_w^{sat} values, which is evident in Fig. 1. For all pollutants except for Fipronil, TCEP, and TCPP, the estimations based on $\log K_{ow}$ were an upper limit, demonstrating that the laboratory $\log K_{PEw}$ values were lower than expected. Fipronil, TCEP, and TCPP had $\log K_{PEw}$ values that were higher than expected from both estimation methods. The equations used for the estimations were created using pollutants with biphenyl and diphenyl ether structures, so it was expected that predicted

K_{PEw}s would be greater than observed K_{PEw}s.

Though Fig. 2 displays low R^2 values for the best fit lines to the K_{PEw} data of both estimation methods, evaluating the slopes of the best fit lines with regards to the slope of the x=y line shows how far away from a perfect estimate each method is because the x=y line represents where the estimation K_{PEw} equals the measured K_{PEw}. For OPFRs, the K_{ow} estimation method showed results that were closer to the laboratory K_{PEw}s in comparison with results from the C_w^{sat} method, as evident by a 0.86 slope for the K_{ow} estimation best fit line versus a slope of 0.56 for the C_w^{sat} estimation best fit line. For CUPs, the C_w^{sat} estimation method showed results that were more reflective of the laboratory K_{PEw}s (as seen by a slope of 1.3) compared to results from the K_{ow} estimation method (as seen by a slope of 1.8). The closer the slope of the best fit line is to a value of one, the closer the relationship is between the estimation method and the observed laboratory $logK_{PEw}$ value. Ideally, the slope between the two would be a value of one demonstrating that the expected $logK_{PEw}$ value is equivalent to the observed laboratory value. However, that slope comparison would only work for ideal chemicals that do not have hydrogen donation capabilities because there are too many possible interactions between the chemical and it's surrounding to be able to predict its affinity to both water and PE.

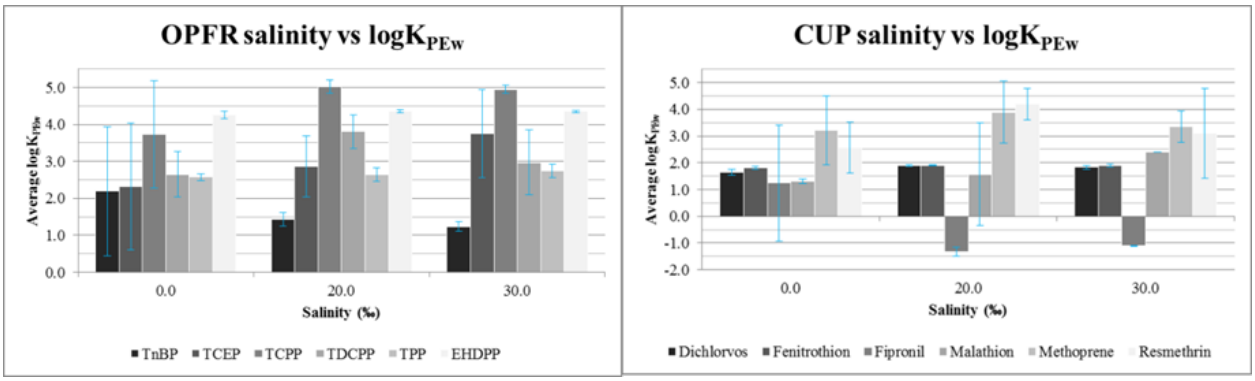

Fig. 3. $LogK_{PEw}$ values as a function of freshwater and saline water. Error bars represent ± one standard deviation about the mean.

Freshwater versus saline water – For most hydrophobic organic pollutants literature suggests that the pollutants' $logK_{PEw}$ value should increase as salt content increases (Lohmann 2011, Lohmann et al. 2012). The OPFRs and CUPs of interest show a range of possible patterns in regards to salinity (Fig. 3).

TCEP, TCPP, and Malathion follow the pattern that literature claims should occur. All three have increasing $logK_{PEw}$ values with increased salinity; however, due to large standard deviations for each, the pattern is not statistically significant. When the standard deviations overlap for a pollutant in comparison with variables, the data is not statistically different from each other, so no conclusion can be made to say that the data points can be distinguished from one another.

TnBP and Fipronil have the opposite pattern where the $logK_{PEw}$ decreases as salinity increases. For both pollutants the standard deviation for freshwater is much larger (± 1.7 for TnBP and ± 2.1 for Fipronil) than that in both concentrations of

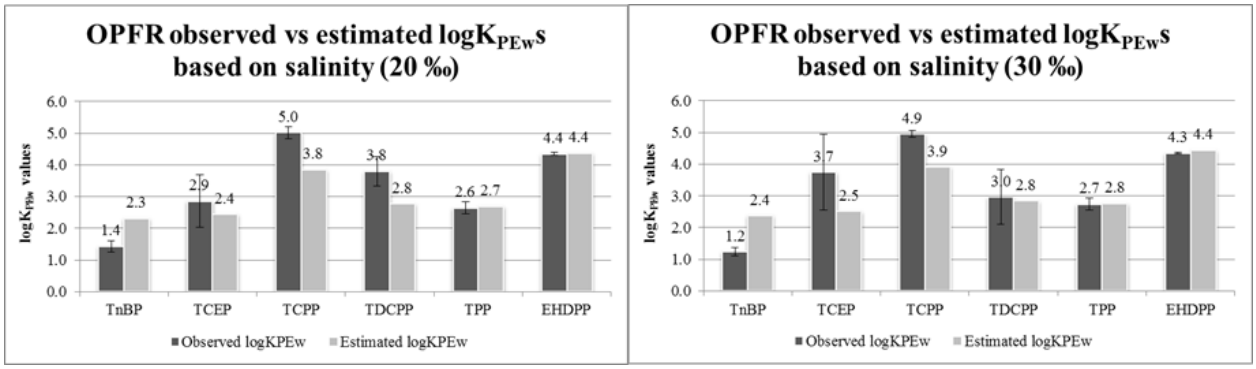

Fig. 4. LogK$_{PEw}$ values for OPFRs as observed in the lab versus their estimated values based on salinity (20 and 30‰).

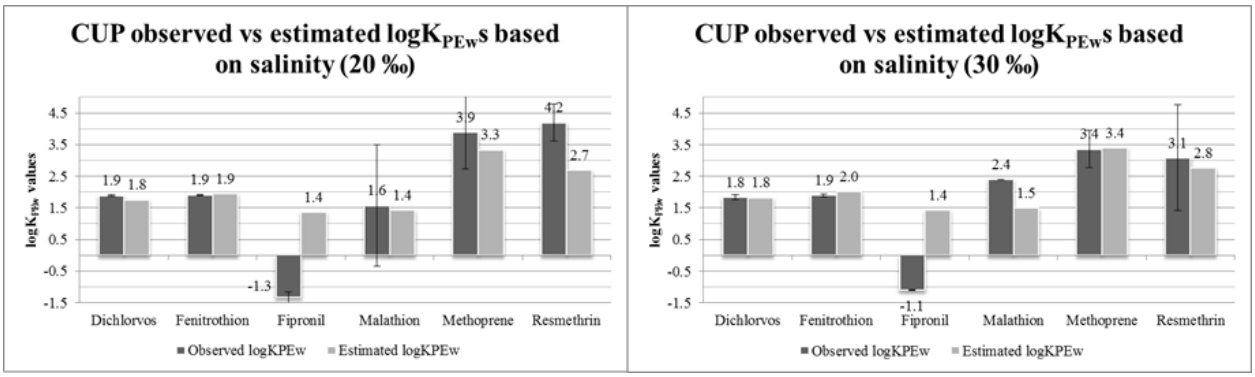

Fig. 5. LogK$_{PEw}$ values for CUPs as observed in the lab versus their estimated values based on salinity (20 and 30‰).

saline water (±0.2, ±0.1 for TnBP and ±0.2, ±0.01 for Fipronil), leading to the conclusion that the pattern is also not statistically significant since the intervals still overlap.

TDCPP, Methoprene, and Resmethrin the K$_{PEw}$ at 20‰ is higher than at 0‰ and 30‰; however, again the pattern is not statistically significant within standard deviation.

However, for the pollutants, such as TPP, EHDPP, Dichlorvos, and Fenitrothion, where the standard deviations do not overlap, there is no distinguishable pattern that can be identified because the logK$_{PEw}$ values remain constant as salinity increases.

Though the OPFRs and CUPs of interest do not follow patterns identified in literature, their logK$_{PEw}$ values can still be used. Since there is no significant pattern, a K$_{PEw}$ that was calculated in the lab under freshwater circumstances could still be used in field research even if it is under saline water circumstances. However, to ensure that this could hold true, another study should be conducted to 1) verify that there are no statistically significant patterns and 2) prove or disprove that pollutant concentrations in water samples are the same where a freshwater-calculated K$_{PEw}$ is used and where a saline water-calculated K$_{PEw}$ is used.

Furthermore, when comparing the measured K$_{PEw}$s with K$_{PEw}$s that were estimated with salinity taken into consideration, there was little difference from what was expected. In regards to the OPFRs (Fig. 4), the largest difference between an estimated and a measured K$_{PEw}$ was a log value of 1.2, observed for TCPP at 20‰ salinity, for TCEP at 30‰ salinity, and for TnBP at 30‰ salinity. All other estimations were within 0-1 log units of laboratory values. In regards to the CUPs

(Fig. 5), two (Fipronil and Resmethrin) showed large differences between the measured and expected KPEws (log values of 2.7 at 20‰ and 1.5 at 20‰, respectively), whereas the rest of the estimations were within 0-0.9 log units of laboratory values.

Though there are some cases where the variation between the estimations and measured K_{PEw}s is high, most estimations were very similar to values observed in the laboratory, which was expected. Fipronil's negative laboratory $logK_{PEw}$ values were unexpected; however, it seems that either the extraction process failed to extract Fipronil out of the water or Fipronil did not partition into the PE. It would be beneficial in future studies to alter the extraction process for water to verify if the low K_{PEw} came from extraction or from a lack of absorption into the PE. Other large differences between expected K_{PEw}s and observed K_{PEw}s could arise from the calculation method for the estimations. Since only NaCl was taken into consideration for ionic strength, a lack of other salts within the calculation could account for differences observed. Future studies may benefit from taking other salts into consideration for these calculations.

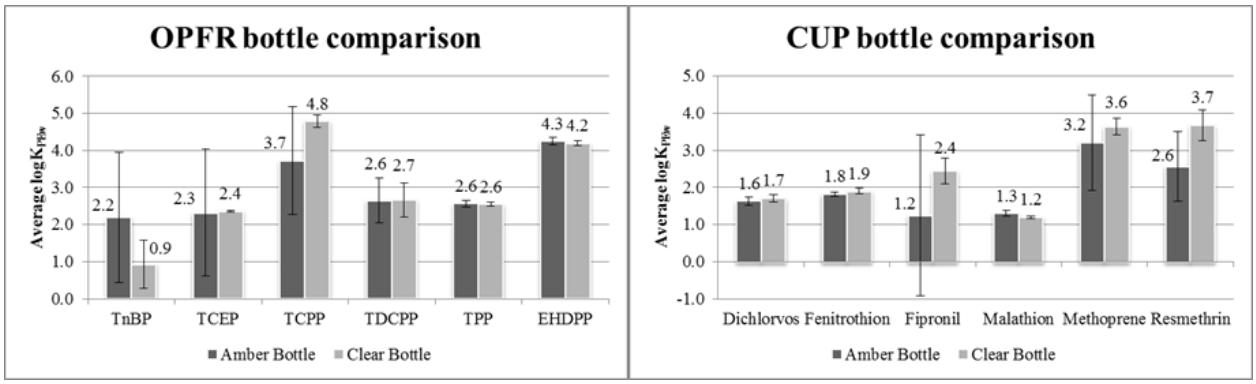

Fig. 6. Comparison of $LogK_{PEw}$ values obtained in amber versus clear bottles.

Table 5. Comparison of the total amount recovered (PE + water) for each OPFR and CUP between amber and clear bottles. Dark gray indicates a value higher than the value in light gray.

	Amount Recovered (ng)					
	from Amber			from Clear		
	PE	Water	Total	PE	Water	Total
TnBP	41.74	119.25	160.99	28.30	113.45	141.75
TCEP	9.83	5.58	15.42	3.39	0.00	3.39
TCPPs	29.62	11.84	41.45	15.78	6.82	22.60
TDCPP	300.99	55.90	356.88	239.07	43.83	282.90
TPP	472.52	296.69	769.21	349.03	231.00	580.03
EHDPP	1,242.09	16.36	1,258.45	873.56	13.54	887.10
Dichlorvos	348.62	0.00	348.62	255.56	0.00	255.56
Fenitrothion	32.27	99.29	131.56	18.10	49.05	67.15
Fipronil	5.74	3.12	8.85	3.01	2.56	5.58
Malathion	1.83	20.93	22.76	1.14	18.07	19.21
Methoprene	264.21	58.24	322.45	195.54	12.43	207.97
Resmethrin	706.81	15.46	722.27	400.53	27.58	428.11

Amber bottle versus clear bottle – Amber glass bottles and clear glass bottles were used to determine whether or not access to light affects a chemical's K_{PEw}. There were only a few scenarios where log K_{PEw}s were different for pollutants when exposed or not to light (Fig. 6). TnBP displayed the single case where the amber bottle K_{PEw} (2.2) was higher than the clear bottle K_{PEw} (0.9). For other pollutants that showed differences between the two variables, the clear bottle K_{PEw} was usually higher than the amber bottle K_{PEw}: 3.7 amber compared to 4.8 clear for TCPP, 1.2 amber compared to 2.4 clear for Fipronil, and 2.6 amber compared to 3.7 clear for Resmethrin. Out of the 12 pollutants, 67% displayed between a 0.1-1.1 log unit difference between the clear and amber K_{PEw} where the clear K_{PEw} was greater. To account for this, the amount of each pollutant recovered was compared for the amber and clear bottles (Table 5). In the clear bottle, less of each pollutant was recovered in the water compared to recovery in the amber bottle. With the K_{PEw} being higher in the clear bottle, it makes sense that less recovery of the pollutants was seen because a high K_{PEw} means there is a high affinity to PE or a low recovery in water. In this case, the low recovery of chemicals in the water samples could be due to degradation of the chemicals from the light passing through the clear glass.

CONCLUSION

K_{PEw}s were measured for six OPFRs and six CUPs. They varied based on the structure and molecular weight of the compounds, and were compared to estimated K_{PEw}s. K_{PEw}s were also estimated using the chemicals' octanol-water equilibrium partition coefficient, water solubility, and freshwater K_{PEw} taking into consideration salinity of sample water. Octanol-water partition coefficients calculated closer estimations for the OPFRs whereas water solubility calculated closer estimations for the CUPs. The K_{PEw}s estimated considering salinity were found to be similar in value for most of the OPFRs and CUPs. No statistically significant pattern was identifiable between salinity (0‰, 20‰, and 30‰) and K_{PEw}. Furthermore, a sample's access to light may degrade pollutants in the water.

ACKNOWLEDGEMENTS

The authors acknowledge NSF for funding of the SURFO program at URI GSO. Thanks to Ben Chebot and the Lohmann Lab group for support and feedback, and thanks to Lucie Maranda, David Smith, and Kathy Donohue for guiding and mentoring the SURFO program. R.L. acknowledges funding from EPA's Great Lakes Restoration Initiative Award GLAS No. 00E00597-0 (Project Officer Todd Nettesheim).

REFERENCES

Adams, R. G, R. Lohmann, L. A. Fernandez, J. K. Macfarlane, and P. M. Gschwend. 2007. Polyethylene devices: passive samplers for measuring dissolved hydrophobic organic compounds in aquatic environments. Environ. Sci. Technol. 41: 1317-1323.

Lohmann, R., and D. Muir. 2010. Global aquatic passive sampling (AQUA-GAPS): using passive samplers to monitor POPs in the waters of the world. Environ. Sci. Technol. 44: 860-864.

Lohmann, R. 2011. Critical review of low-density polyethylene's partitioning and diffusion coefficients for trace organic contaminants and implications for its use as a passive sampler. Environ. Sci. Technol. 46: 606-618.

Lohmann, R., K. Booij, F. Smedes, and B. Vrana. 2012. Use of passive sampling devices for monitoring and compliance checking of POP concentrations in water. Environ. Sci. Pollut. Res. 19: 1885-1895.

Sacks, V. P., and R. Lohmann. 2011. Development and use of polyethylene passive samplers to detect triclosans and alkylphenols in an urban estuary. Environ. Sci. Technol. 45: 2270-2277.

Salamova, A., M. H. Hermanson, and R. A. Hites. 2014. Organophosphate and halogenated flame retardants in atmospheric particles from a European arctic site. Environ. Sci. Technol. 48: 6133-6140.

McElroy, A. E., A. M. Zulkosky, J. P. Ruggieri, S. A. Terracciano, and B. J. Brownawell. Acute toxicity of Resmethrin, Malathion, and Methoprene to larval and juvenile American lobsters (*Homarus americanus*) and analysis of pesticide levels in surface waters after Scourge™, Anvil™, and Altosid™ application. J. Shellfish Res. 24 (3): 795-804.

B. Kerr is at Adrian College, Adrian, MI, (bkerr@adrian.edu)
C. McDonough (carriemc@my.uri.edu)
Rainer Lohmann (rlohmann@uri.edu)

Ocean Surface Wave Modeling under Hurricane Conditions

Joshua Port and Tetsu Hara
Graduate School of Oceanography, University of Rhode Island, Narragansett, RI 02882

Abstract

In order to best prepare coastal regions for incoming storms, the ability to model hurricane track and intensity has never been more vital. The ocean surface wave field (sea state) may significantly impact the hurricane intensity forecast because it modifies the air-sea momentum and heat fluxes as well as the upper ocean turbulent mixing. Therefore, it is important to include accurate sea state predictions in hurricane prediction models. The WAVEWATCH III (WW3) model, a wind-wave model developed by the National Oceanic and Atmospheric Administration, is one of the best models currently available and will be incorporated in the next generation hurricane prediction models. However, WW3 performance under hurricane conditions has not been thoroughly tested and requires further validations against observational data. This study compares the significant wave height (SWH) predicted by WW3 with satellite and Scanning Radar Altimeter (SRA) observational results during Hurricane Irene (2011). The WW3 data are generated with and without considering ocean currents and with different wind forcing products. The inclusion of currents generally reduces the predicted SWH and improves the correlation between WW3 predictions and observational data. While both SRA and satellite data offer reasonably good correlations with the WW3 data, the standard deviation of the satellite data from the WW3 data is significantly smaller than that of the SRA data. The generally good correlation found between the observational SWH readings and the SWH values from WW3 supports the validity of the WW3 wave model results under hurricane conditions.

In order to best prepare coastal regions for incoming storms, the ability to model hurricane track and intensity has never been more vital. Although there is still some debate over the extent to which man-induced climate change impacts the intensity of Atlantic hurricanes, the general consensus is that warming ocean temperatures are one factor that can contribute to an increase in hurricane intensity; therefore, being able to model and adjust for more frequent larger storms will remain important for the foreseeable future (Demaria and Kaplan 1994; Goldenberg 2001; Vecchi and Soden 2007).

The ocean surface wave field (sea state) may significantly impact the hurricane intensity forecast because it modifies the air-sea momentum and heat fluxes and the upper ocean turbulent mixing. Therefore, it is important to include accurate sea state predictions in the hurricane prediction models. WAVEWATCH III (WW3), a coupled wind-wave model originally developed at the National Oceanic and Atmospheric Administration (NOAA), has been used for many years to model the surface wave field during hurricanes. An earlier version of the model was validated against Scanning Radar Altimeter (SRA) data collected during Hurricane Bonnie (1998), although the WW3 simulation did tend to break down in shallow water (Moon et al. 2003). Tolman et al. (2005) showed that WW3 systematically overestimated significant wave height (SWH) for

Hurricane Isabel. Moon et al. (2008) came to a similar conclusion while investigating WW3 performance during Hurricane Katrina. It was determined that WW3 tended to overestimate SWH during the hurricane with error increasing with wave height. Fan et al. (2009) examined WW3 output and SRA observations during Hurricane Ivan (2004), a category five hurricane, and showed that improving the drag coefficient parameterization and accounting for ocean currents lowered SWH predictions and made them more consistent with observations.

This study seeks to validate the WAVEWATCH III model by comparing simulated SWH values during Hurricane Irene (2011) to observationally determined SWH; values from NOAA's SRA and the Jason-1, Jason-2, and CryoSat-2 satellite altimeters are compared to WW3 values to determine the quality of model predictions under hurricane conditions. Specifically, the model's simulations are performed with two different wind forcing products (TC Vitals and HWnd) and with or without considering ocean currents. WW3 results in shallow water regions are also investigated in order to determine the impact of depth on model output.

METHODS

The WW3 simulations were performed with the approach of Fan et al. (2009); their improved drag coefficient parameterization was used. Two simulations with TC Vitals were performed with and without ocean currents and one simulation with HWnd was performed without the ocean current. Version 3.14 of WW3 was used to conduct both simulations that disregarded ocean currents, whereas version 5.05 of WW3 was used to conduct the simulation that considered currents. Although the versions of the model differed in number, the same source term packages were used.

All of the satellite altimetry data used in this study were made publicly available online. Jason-1's network Common Data Form (NETCDF) altimetry data were obtained from the NASA Jet Propulsion Laboratory's Physical Oceanography Distributed Active Archive Center (PODAAC). Jason-2's NETCDF altimetry data was sourced from the Centre National d'Études Spatiales (CNES) through their Archiving, Validation, and Interpretation of Satellite Oceanographic data (AVISO+) database. The NOAA's National Environmental Satellite, Data, and Information Service (NESDIS) provided altimetry data for the CryoSat-2 satellite.

Once all SWH data sets were accessed, MATLAB software was then used to extract all of the unflagged temporally and spatially relevant points from the satellite data set. The WW3 data were then interpolated temporally and spatially using the built-in three-dimensional interpolation function to align them with the points from the observational data sources. All points with SWH values less than two meters were removed from the data set. Once this data set was assembled, a series of observational SWH vs. simulated SWH plots were made comparing all four sources of observational data with all three WW3 data sets. The standard deviations of the observational data from the WW3 data (i.e., the standard deviation from the line y=x, where x is the WW3 data and y is the observational data) were then tabulated along with the slopes of the lines of best fit (found using linear regression). The standard deviations and best fit slopes were then used to determine the quality of the data set; WW3 SWH predictions using TC Vitals and HWnd, SWH predictions in deep (>50 meters) and shallow (<50 meters) water, and SWH

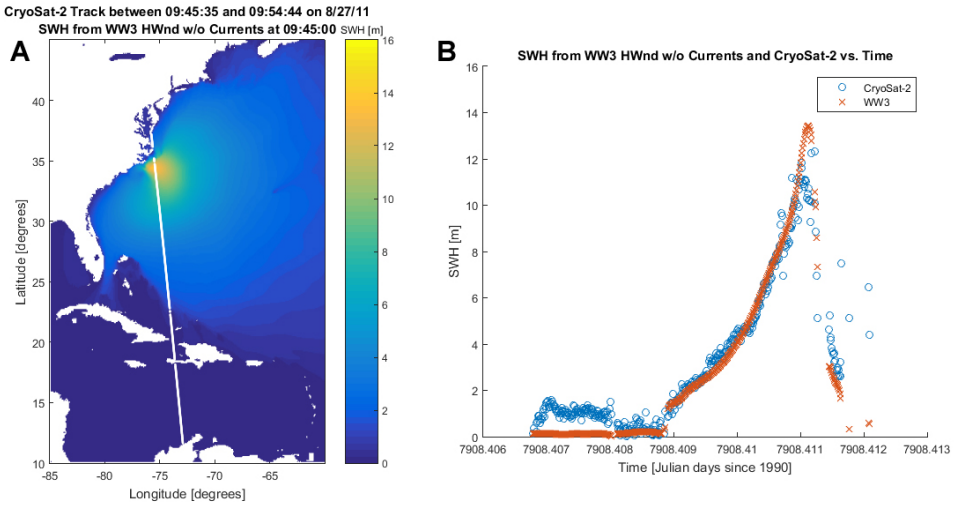

Fig. 1. An example of comparison between satellite SWH and WW3 SWH. a) White line shows Pass 10 of CryoSat-2, and background color shows simulated SWH at the corresponding time from WW3 with TC Vitals. b) Time series of satellite SWH and WW3 SWH during the satellite pass.

predictions with and without considering ocean currents were all compared for relative quality. Furthermore, by comparing the tabulated values for SRA and satellite sources, the relative quality of these SWH data sources can be inferred.

RESULTS

Fig. 1a shows an example of the correlation between satellite and simulated SWH values, with the satellite path and the significant wave height estimated by the WW3 at the same time. Fig. 1b compares the observed and simulated SWH values along the path and shows excellent agreement between the satellite and WW3 SWH values except for waves below 2 m. The poor agreement of very small waves is expected because the WW3 simulation ignores wind forcing outside the hurricane and underestimates the wave field in those regions. We therefore removed all wave data below two meters as mentioned earlier.

Impact of Currents – The SWH on the right side of the storm tends to be larger than on the left; hurricane winds rotate counter-clockwise in the northern hemisphere, and thus winds to the right of the eye are roughly in the direction of the storm's propagation. Since the energy of waves formed on the right side of the storm propagates at their group velocity roughly in the same direction as the storm, the waves are able to stay under the areas of high wind for a longer period than waves formed elsewhere in the storm. The group velocity of these large waves is usually larger than the storm propagation speed and the wave field eventually propagates out of the region of highest wind. Since ocean currents in this region are typically in the same direction as the wind, they tend to increase the effective propagation speed of the wave field, i.e., the wave field stays under areas of strong wind for a shorter period. Consequently, it is expected that including ocean currents in the WW3 simulations decreases the predicted SWH.

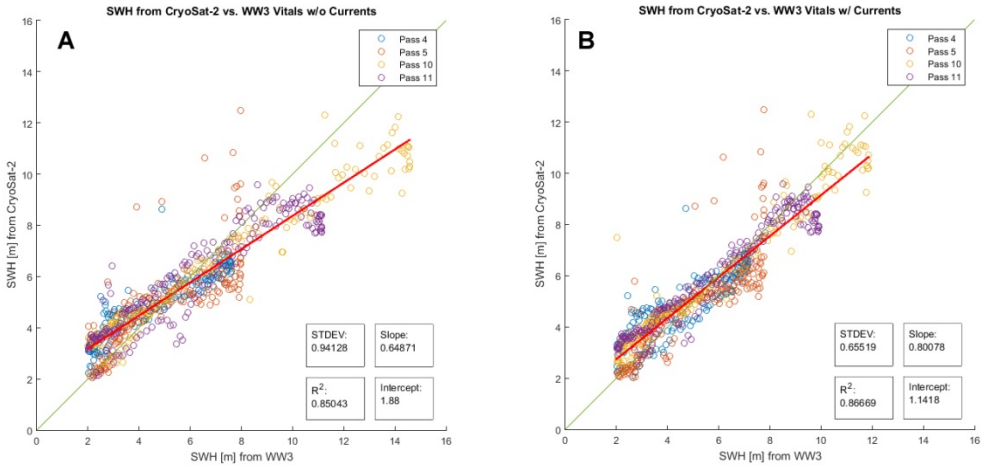

Fig. 2. a) Plot of CryoSat-2 significant wave height vs. simulated significant wave height. WW3 data is generated using the TC Vitals wind product and without considering currents. Data from each satellite pass over the WW3 data region during Hurricane Irene is distinguished as shown in the legend. The field marked "STDEV" is the standard deviation around the line y=x. The "Slope" and "Intercept" fields refer to the line of best fit, which is shown by a thick red line. The thin black line indicates y=x. b) Same as Fig. 2a, except WW3 data is generated considering currents

Table 1. Comparison of observational significant wave height vs. simulated significant wave height. Standard deviation values (m) around the line y=x are shown in rows 2-4, and slopes of the lines of best fit are shown in rows 5-7. The WW3 parameters (wind product, current effect) are specified in the first column, whereas the observational data source is listed in the first row.

	Jason-1	Jason-2	CryoSat-2	SRA (total)	SRA (<50 m)	SRA (> 50m)
Irene (Vitals w/o currents)	0.93	0.71	0.94	1.79	1.21	1.85
Irene (Vitals w/ currents)	0.90	0.75	0.66	1.70	1.41	1.72
Irene (HWnd w/o currents)	0. 80	0.74	0.77	1.63	1.32	1.66
Best fit slope (Vitals w/o currents)	0.84	1.05	0.65	0.67	N/A	N/A
Best fit slope (Vitals w/ currents)	1.03	1.14	0.80	0.75	N/A	N/A
Best fit slope (HWnd w/o currents)	1.02	1.00	0.78	0.81	N/A	N/A

The WW3 simulation results indeed show that including ocean currents reduces the predicted SWH. Fig. 2 is an example showing that including currents reduces WW3 SWH estimates and increases the slope of the best fit line. The inclusion of currents in the WW3 model results in a systematic increase in slope for all comparison plots (Table 1); when currents are considered, WW3 systematically lowers its predictions for SWH. This result is consistent with the findings of Fan et al. (2009) for Hurricane Ivan. The inclusion of currents generally improves correlation as well (reduces the standard deviation of the difference between observed and predicted SWH values and makes the slope of the best fit line closer to one). This was true for three of the four sources of observational data in this study (Table 1), and is also consistent with the findings of Fan et al. (2009) for Hurricane Ivan.

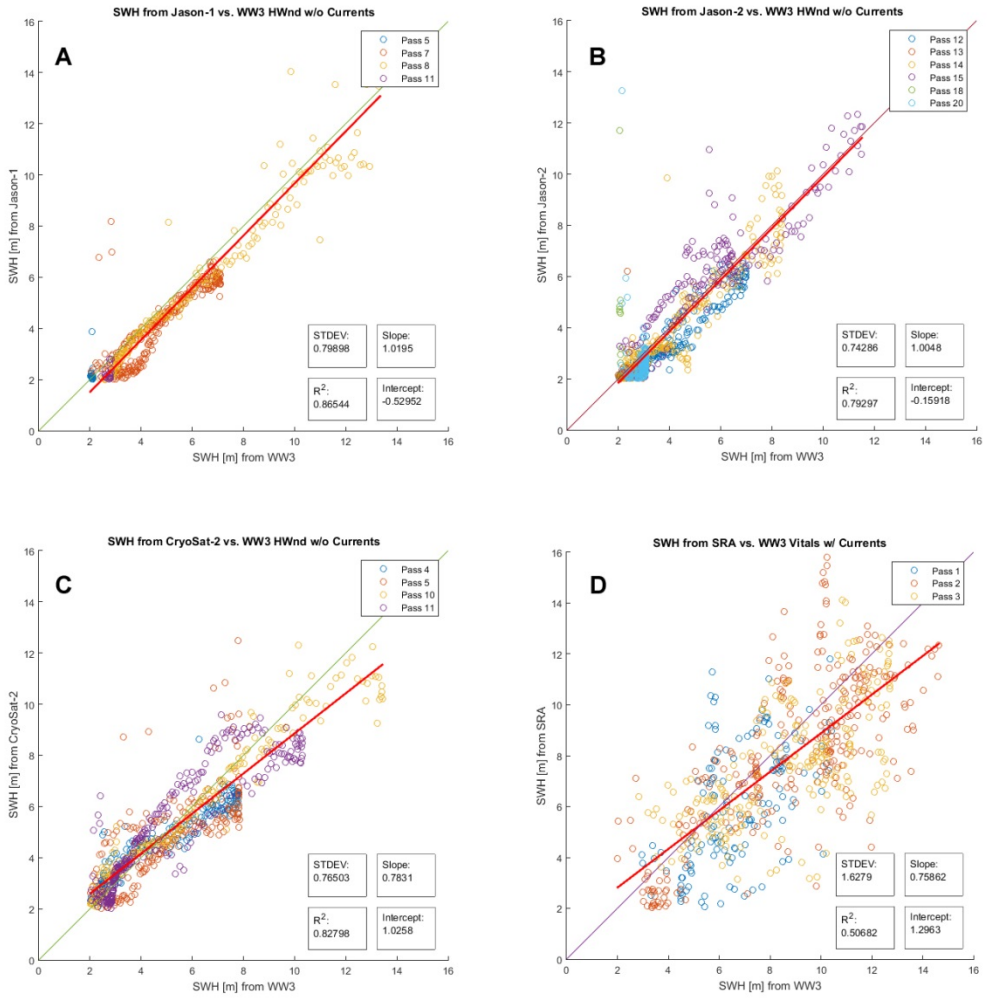

Fig. 3. a-c) Plots of satellite significant wave height vs. significant wave height simulated using HWnd. d) Same as Fig. 3a-c, except the y-axis is SRA significant wave height.

Observational Data Quality – Since the slope of the best fit line between the WW3 results and the observational data is usually close to one (Table 1), it suggests that the WW3 results are reasonably accurate without a significant bias. Then, the standard deviation value around the line y=x, which shows the extent to which two data sets agree, can be used to evaluate the quality of different observational data sets. Fig. 3a, 3b, and 3c show plots of observational SWH vs. WW3 SWH (using HWnd) for the three satellite altimeters used in this study. Fig. 3d compares SWH measured by the SRA vs. WW3 SWH (using HWnd). Whereas the standard deviation values of the satellite vs. WW3 plots are all between 0.74 meters and 0.80 meters, the SRA vs. WW3 plot has a standard deviation of 1.63 meters. Since the slopes of the lines of best fit are comparable between all plots, this high standard deviation value is a result of more widely spread (noisier) data points rather than a systematic over or underestimation by WW3. The larger standard deviation value of the SRA data is partly due to the way the

SWH is estimated; since the footprint (area of averaging) of the individual SRA observation is small compared to that of the satellite observation, it is expected that the standard deviation would be larger. However, the quality of the SRA data in the study by Fan et al. (2009) is significantly better, that is, the standard deviation is smaller. Therefore, it is possible that the SRA data of Hurricane Irene (2011) had some data quality control problems. Concerning satellite data quality, all three satellites correlated similarly well with WW3 despite their different ages and altimetry packages, as evidenced by their similar standard deviation values when compared to the WW3 data sets.

Wind Product – Although more difficult to access than TC Vitals, HWnd is generally considered to be the superior wind product. HWnd provides a grid of wind vectors at regular time intervals, between which interpolation determines the approximate wind field. TC Vitals, however, is essentially limited to the radius of maximum wind speed and the radii of a certain wind speed in four quadrants around the storm center, through which a contour of constant wind can be fitted. By interpolating between these contours, the wind field over the entire region can be determined. The lack of detail in the TC Vitals file is the reason why the HWnd product is considered superior; due to the large amount of interpolation required, TC Vitals tends to be less accurate in irregular wind conditions.

This study supports the conclusion that HWnd is a superior wind product to TC Vitals. The SWH from each observational source vs. the WW3 SWH using HWnd showed smaller standard deviation as compared to the WW3 SWH using the TC Vitals, as can be seen in Table 1. Furthermore, the slope of the line of best fit was closer to one in all cases when HWnd was used instead of TC Vitals. Because we did not have access to the WW3 data using HWnd that also considered ocean currents, the above comparisons were made between data sets that did not take currents into account. It remains to be seen if a similar improvement is observed when currents are considered.

Ocean Depth – As noted by Moon et al. (2003), early versions of WW3 did not accurately predict the SWH in shallow water, likely because they improperly accounted for the wave shoaling process. Newer editions of WW3 are supposed to have fixed this issue, but they have not been tested under hurricane conditions. Unfortunately, there were insufficient satellite data points in shallow water with moderate or high SWH values to validate the WW3 results. Each satellite SWH reading is obtained from many radar pulses reflected over a large area, and any radar pulses that reflect off of land give very erratic results. Therefore, SWH values recorded too close to shore tend to be flagged for quality. The SRA readings, however, can be taken much closer to shore without compromising data quality, and can be used to examine the quality of shallow water WW3 predictions. Although the slope of the line of best fit cannot be estimated because of the relatively small range of SWH readings in shallow water, the standard deviation of the shallow water subset of the SRA data vs. WW3 is comparable to that of the deep water subset as shown in Fig. 4. This observation suggests that the WW3 simulation quality in shallow water regions is reasonably good.

SUMMARY AND CONCLUSION

In this study, simulated SWH values from the WW3 model correlated well with observational data in hurricane conditions.

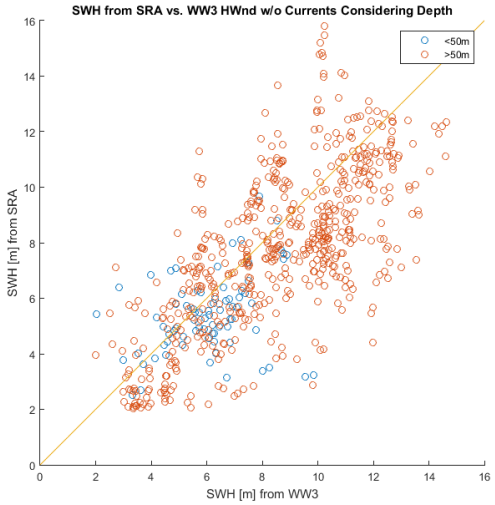

Fig. 4. Plot of SRA significant wave height vs. significant wave height simulated using HWnd. Readings taken in shallow water are distinguished from readings taken in deep water.

The satellite SWH readings deviated much less from the WW3 data than did the SRA SWH readings. Furthermore, the inclusion of currents in the WW3 simulation systematically lowered SWH predictions, which generally improved correlation with observational data. When the HWnd wind product was used instead of TC Vitals, SWH from WW3 agreed better with observational SWH values. This was expected given the higher level of detail in HWnd as compared to TC Vitals. It remains to be seen if this trend will hold true when ocean currents are taken into account. Additionally, it was determined that the SWH predictions by the current version of WW3 in shallow water were reasonably accurate.

ACKNOWLEDGMENTS

The author would like to thank Mr. Brandon Reichl for running the necessary WW3 simulations and for advice throughout the research process. Mr. Austen Blair is also thanked for his advice. Additionally, Dr. Isaac Ginis was instrumental in the WW3 simulation process. The funding for this research was provided by NSF through the SURFO program at the URI Graduate School of Oceanography.

REFERENCES

Demaria, M., and J. Kaplan. 1994. Sea Surface Temperature and the Maximum Intensity of Atlantic Tropical Cyclones. Journal of Climate 7: 1324-1334.

Fan, Y., I. Ginis, T. Hara, C. Wright, and E. Walsh. 2009. Numerical Simulations and Observations of Surface Wave Fields under an Extreme Tropical Cyclone. J. Phys. Oceanogr. 39: 2097-2116.

Goldenberg, S. 2001. The Recent Increase in Atlantic Hurricane Activity: Causes and Implications. Science 293: 474-479.

Moon, I., I. Ginis, and T. Hara. 2008. Impact of the Reduced Drag Coefficient on Ocean Wave Modeling under Hurricane Conditions. Mon. Wea. Rev. 136: 1217-1223.

Moon, I., I. Ginis, T. Hara, H. Tolman, C. Wright, and E. Walsh. 2003. Numerical Simulation of Sea Surface Directional Wave Spectra under Hurricane Wind Forcing. J. Phys. Oceanogr. 33: 1680-1706.

Tolman, H., J. Alves, and Y. Chao. 2005. Operational Forecasting of Wind-Generated Waves by Hurricane Isabel at NCEP*. Wea. Forecasting 20: 544-557.

Vecchi, G., and B. Soden. 2007. Effect of remote sea surface temperature change on tropical cyclone potential intensity. Nature 450: 1066-1070.

J. Port is at Tufts University, Medford, MA (joshua.port@tufts.edu)
T. Hara (tetsuhara@uri.edu)

Biogenic silica records of productivity across Narragansett Bay's nutrient gradient from pre-industrialization to present

Kyle C. Rennell, Neil Redmond, Rebecca S. Robinson
Graduate School of Oceanography, University of Rhode Island, Narragansett, RI 02882

Abstract

Documenting variations in diatom productivity in relation to global climate and anthropogenically driven environmental changes aids in assessment of the health and vitality of estuaries. Sediment cores representing 300-1000 years of deposition from Narragansett Bay were used to study the nutrient gradient and its impact on diatom productivity. Here, biogenic silica (BSi), diatoms' biomineral, is used as a tracer of diatom abundance through time. BSi was extracted from the sediment and quantified colorimetrically. Nitrogen and carbon contents of each core were compared to BSi to evaluate changes in total production. Core NB70, recovered in the upper bay, and core NB66, from the mid bay, show an increase in carbon and nitrogen content as well as an increase in the ratio of carbon-to-nitrogen (C/N) throughout the past 150 years. The shift in C/N indicates that the increase in sedimentary organic matter contents may be from enhanced terrestrial inputs. BSi percentages in both cores decreased toward the present. Higher organic matter content and slightly higher BSi content in NB70 are consistent with its location near point source nutrient inputs. The similar long-term trend in BSi content in both cores NB70 and NB66 suggests a bay wide cause, possibly related to a diatom production decrease. However, the data also suggest that increased delivery of terrestrial sediment, likely due to land use changes, may bias the record.

Alterations in estuary productivity due to anthropogenic influences on coastal ecosystems have occurred during the last century (Bowen & Valiela, 2001). Industrialization occurred in New England around ~1850 (Lima et al., 2005), and with it came massive land clearance, leading to increased sedimentation rates as well as established sources of pollution (King et al., 2008). Determining how these environmental fluctuations due to human activity have led to increases or decreases in productivity within the bay is of great importance. Areas such as the Chesapeake Bay have experienced disastrous eutrophic events and algal blooms resulting from the discharge of nutrients and influx of terrestrial organic matter into the bay (Colman & Bratton, 2003). This influx results in nutrient over-enrichment and an increase in phytoplankton production that can lead to the near complete depletion of oxygen (Colman & Bratton, 2003). A key concern in Narragansett Bay is the amount of nutrients being transported via freshwater tributaries (Pruell, et al., 2006). A major source of nitrogen influx into Narragansett Bay is from the discharge of waste water treatment facilities into local surface water. These sources extend from Massachusetts down into the Narragansett Bay area (Pruell et al, 2006), and they clearly impact the Providence River where the tributaries meet the estuary. However, the role of these additional nutrients on the overall Bay productivity remains unclear. By looking at diatom productivity over longer timescales, we may be able to see how the ecosystem in the area has reacted in the context of longer term productivity trends.

Diatoms make up a large percentage of the phytoplankton in Narragansett Bay (Borkman & Smayda, 2009), and are highly susceptible to changes in temperature, pH, salinity, and nutrient levels (Andren et al, 1999; Borkman & Smayda, 2009). For over fifty years, decreases in diatom productivity within Narragansett Bay have been recorded and attributed to a changing climate (Falkowski, 1998). The frustules of diatoms are composed of biogenic silica, and the preservation of this biogenic silica within sediment can produce a record of diatom productivity within the bay (Colman & Bratton, 2003) that extends beyond the current plankton time-series, and beyond recorded history. The objectives of this study were: 1) To look at long-term productivity trends found in the sediment records of Narragansett Bay, and 2) To see if recent historical observations in productivity are atypical of the long-term trends.

METHODS

Setting – Cores NB70 and NB66 were collected by W. Prell and D. Murray of Brown University. These two cores were selected based on their positions within Narragansett Bay (Fig. 1) along the nutrient gradient (Pruell et al. 2006). Each core is approximately a meter in length and spans 300-1000 years. Core NB70 was recovered in the nutrient rich Providence River and NB66 was from the mid-bay. Lead concentrations from the cores were used to roughly determine the time of industrialization in the area (1850) (Lima et al., 2005). Radiometric dating of cores will be completed at Brown University.

Analysis – Opal content was measured in two-centimeter increments on dried bulk samples. Prior to analysis, samples were ground with a mortar and pestle to produce a homogeneous fine powder. Eighty mg of sample was used for opal extraction following the method of Mortlock and Froelich (1989). A change was made to the method where 0.5 M sodium hydroxide (NaOH) was substituted for the sodium carbonate (Na_2CO_3)because previous work found NaOH was more effective at extracting biogenic silica completely. Biogenic silica percentages were obtained and then multiplied by 2.4 to obtain opal percentages (Mortlock & Froelich, 1989). An in-house sediment standard was run with each series of core samples in order to evaluate precision. Absolute standard error was ±0.08%.

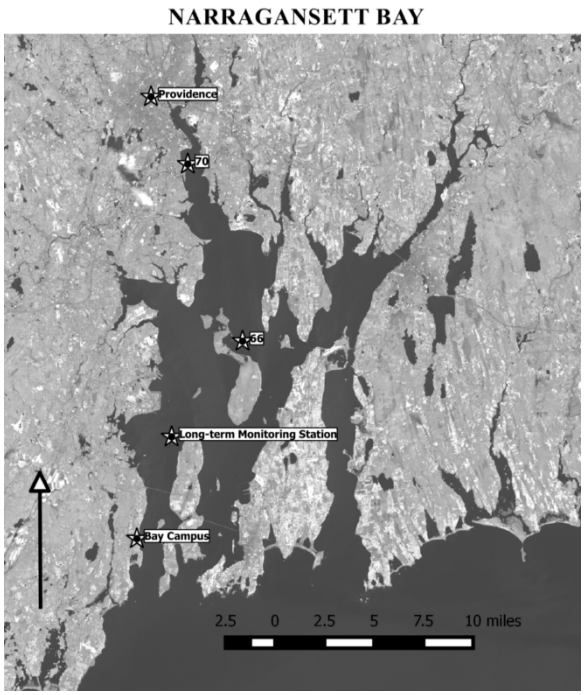

Fig. 1. Map of Narragansett Bay, Rhode Island, USA. Core locations, city of Providence, URI Bay Campus, and long-term plankton monitoring station are marked with a star.

RESULTS

Core 70 – Opal content was high (~9%) at the base of core NB70 and decreased to ~5% near present (Fig. 2a). The lead data (Fig. 2d) suggest that opal decreased around

1850, at the onset of industrialization. Nitrogen and carbon contents (Fig. 2c) in NB70 increase from ~0.20% to ~0.40% and ~0.22% to ~0.50%, respectively, after the onset of industrialization. The C/N (Fig. 2b) increases at ~47 cm from a value of ~13 to ~19 mol/mol.

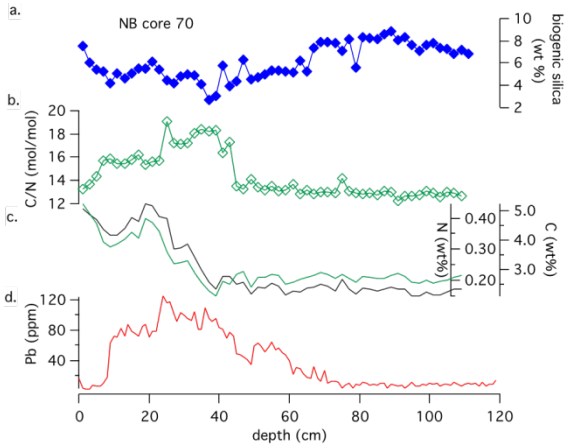

Fig. 2. Downcore data from Core 70. (a) Biogenic Silica percentages. (b) C/N. (c) Carbon and Nitrogen percentages. (d) Lead (ppm) from W. Prell and D. Murray (unpubl.).

Core 66 – Core NB66 shows a long-term decrease, from ~9% to ~5% in opal content toward present (Fig. 3a). At ~32 cm, lead began to increase from ~12 to ~50 ppm (Figure 3d) signifying regional industrialization (Lima et al., 2005). At this location in the core there is also a decrease in opal followed by a slightly lagging increase in organic carbon and nitrogen (Fig. 3c) content. Nitrogen and Carbon increase from ~0.18% to ~0.29% and ~0.20% to ~0.32%, respectively. C/N (Fig. 3b) increased at ~32 cm from ~12 to ~14 mol/mol.

DISCUSSION

Core 70 had much higher opal percentages than Core 66, most likely attributed to being further up on the nutrient gradient. The observed decreases in opal, present in both the mid and upper bay cores, suggest a regional control on opal deposition. This trend can be explained either by 1) a decrease in diatom abundance due to changing climate as suggested by Borkman & Smayda, (2009), or 2) a change in the relative contribution of terrestrial sediment, effectively diluting the opal within the sediment (Tyson, 2001).

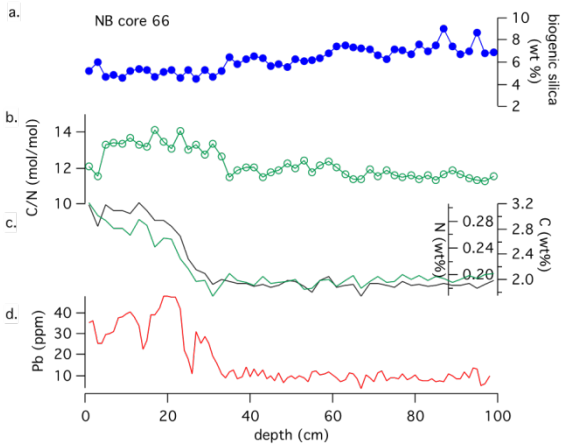

Fig. 3. Downcore data from Core 66. (a) Biogenic Silica percentages. (b) C/N. (c) Carbon and Nitrogen percentages. (d) Lead (ppm) from W. Prell and D. Murray (unpubl.).

A decrease in nutrient mixing has been attributed to warming of sea surface temperatures, which in turn decrease diatom productivity (Falkowski, 1998). The increase in temperature seen in Narragansett Bay may be the driving force behind the decrease in opal percentages. It may not reflect an overall decrease in production but rather a shift away from diatom dominance. An increase in winter bay temperatures by 1.5-2.5 °C (Borkman & Smayda, 2009) in the face of high nutrient contents from point source contributions (Pruell et al., 2006) could have shifted production from diatoms to another member of the phytoplankton community (Borkman & Smayda, 2009)

such as flagellates and/or nanoplankton (Anderson, Glibert, & Burkholder, 2002).

Dilution of sediment seems to be a likely cause of the apparent decrease in opal percentages. The data taken from both cores show large increases in carbon, nitrogen, and C/N after industrialization occurred. Vast and widespread clearing of land as well as residential and burgeoning industry development have occurred in the last century (King et al., 2008). These changes would all contribute to an increase in sediment transport into the bay. Terrestrial organic matter contains more carbon than marine organic matter (Polyakova & Stein, 2004), so the drastic increases in C, N, and C/N suggest that the source of the material is terrestrial in origin (Tyson, 2001). Even if diatom production stayed constant after industrialization, it may appear to have decreased because of a higher percentage of terrigenous sediment in relation to the opal (Tyson, 2001). Sedimentation rates via radiometric dating are needed in order to determine a more accurate production history.

The shifts in opal at the top of each record hint at a reversal of the downward trend. These peaks may be associated with attempts to reduce pollution entering into the bay (King et al., 2008), but equivocal at best. However, not enough data are available to uniquely interpret them.

CONCLUSION

Opal measurement in cores taken along the nutrient gradient in Narragansett Bay has shown to have a long-term downward trend in opal contributions. It remains unclear whether these decreases are attributed to a changing climate or whether they are just from the effects of an increase in sedimentation. Efforts to understand these changing dynamics will continue with the processing of the other two cores taken from the bay as well as an investigation in possible changes in phytoplankton communities and the role of sea surface temperatures in the area.

ACKNOWLEDGMENTS

Thanks to Colin Jones of URI Graduate School of Oceanography for discussion and support in the lab; Warren L. Prell and David Murray of Brown University provided sediment cores, Pb, C, and N data. The National Science Foundation and URI's SURFO program funded Rennell. Research was supported by a RI STAC grant to Robinson.

REFERENCES

Andren, E., Shimmield, G., & Brand, T. (1999). Centuries Indicated, 1, 25–38.

Borkman, D. G., & Smayda, T. (2009). Multidecadal (1959-1997) changes in Skeletonema abundance and seasonal bloom patterns in Narragansett Bay, Rhode Island, USA. Journal of Sea Research, 61(1-2), 84–94. http://doi.org/10.1016/j.seares.2008.10.004

Bowen, J. L., & Valiela, I. (2001). The ecological effects of urbanization of coastal watersheds: historical increases in nitrogen loads and eutrophication of Waquoit Bay estuaries. Canadian Journal of Fisheries and Aquatic Sciences, 58(8), 1489–1500. http://doi.org/10.1139/f01-094

Colman, S. M., & Bratton, J. F. (2003). Antropogenically induced changes in sediment and biogenic silica fluxes in Chesapeake Bay. Geology, 31(1), 71–74. http://doi.org/10.1130/0091-7613(2003)031<0071:AICISA>2.0.CO;2

Falkowski, P. G. (1998). Biogeochemical Controls and Feedbacks on Ocean Primary Production. Science, 281(5374), 200–206.

http://doi.org/10.1126/science.281.5374.200

King, J. W., Hubeny, J. B., Gibson, C. L., Laliberte, E., Ford, K. H., Cantwell, M., McKinney, M. & Appleby, P. (2008). Anthropogenic Eutrophication of Narragansett Bay: Evidence for Dated Sediment Cores. In Science for Ecosystem-Based Managment (pp. 211–232).

Lima, A. L., Bergquist, B. a., Boyle, E. a., Reuer, M. K., Dudas, F. O., Reddy, C. M., & Eglinton, T. I. (2005). High-resolution historical records from Pettaquamscutt River basin sediments: 2. Pb isotopes reveal a potential new stratigraphic marker. Geochimica et Cosmochimica Acta, 69(7), 1813–1824. http://doi.org/10.1016/j.gca.2004.10.008

Mortlock, R. A., & Froelich, P. N. (1989). A simple method for the rapid determination of biogenic opal in pelagic marine sediment. Deep-Sea Research, 36(9), 1415–1426.

Polyakova, Y. I., & Stein, R. (2004). Holocene paleoenvironmental implications of diatom and organic carbon records from the southeastern Kara Sea (Siberian Margin). Quaternary Research, 62(3), 256–266. http://doi.org/10.1016/j.yqres.2004.08.002

Pruell, R. J., Taplin, B. K., Lake, J. L., & Jayaraman, S. (2006). Nitrogen isotope ratios in estuarine biota collected along a nutrient gradient in Narragansett Bay, Rhode Island, USA. Marine Pollution Bulletin, 52(6), 612–620. http://doi.org/10.1016/j.marpolbul.2005.10.009

Tyson, R. V. (2001). Sedimentation rate, dilution, preservation and total organic carbon : some results of a modelling study, 32, 333–339.

K. Rennel is at Lock Haven University, 401 N. Fairview Street, Lock Haven, PN 17745, kcr1153@lhup.edu
N. Redmond (neil_redmond@my.uri.edu)
R. S. Robinson (rebecca_r@uri.edu)

Exploring the use of I/Ca as a proxy for dissolved oxygen in the eastern tropical pacific

Felicia Rodier and Rebecca Robinson
Graduate School of Oceanography, University of Rhode Island, Narragansett, RI 02882

Abstract

Oxygen is fundamentally important to most organisms because it is required to carry out respiration. Some regions of the ocean have so little oxygen that they are hypoxic, below 60-120 μmol kg^{-1}, and populations living in these regions are under physiological stress and experience enhanced mortality rates. Over time, these regions have expanded and contracted. A proxy for dissolved oxygen must be used to determine the past extent of these oxygen minimum zones. We explored the use of a novel proxy, the iodine-to-calcium ratio (I/Ca) in planktic foraminifera in hypoxic systems. Iodine exists in two forms in the ocean, iodate and iodide. Iodate is incorporated in calcium carbonate whereas iodide is not. Under conditions of low oxygen, iodate reduces to form iodide. The use of this proxy has been restricted to anoxic systems and its sensitivity has not been thoroughly explored. Two types of planktic foraminifera, surface and thermocline dwelling forms, were picked from sediment cores at two locations in the Eastern Tropical Pacific. Each sample was cleaned of clays and other contaminants through a series of physical and chemical separations. The cleaned foraminifera were dissolved and the resulting solutions measured by inductively coupled plasma mass spectrometer (ICP-MS) for iodine and calcium. Preliminary results, giving very high I/Ca values, suggest that the cleaning of the foraminifera was not as effective in our samples. More data are needed to provide conclusive evidence for the effectiveness of this proxy in regions of hypoxia.

Dissolved oxygen is essential for most forms of marine life because it is needed to respire. Without adequate levels of dissolved oxygen, most species undergo stress, migrate, or die (Deutsch et al. 2011). Some regions of the oceans have persistent hypoxic levels of dissolved oxygen below the surface waters. These regions are known as oxygen minimum zones (OMZ). OMZs have been known to expand and contract during large scale climate changes and with changes biological activity (Zhou et al. 2014; Stramma et al. 2008). Geological records of dissolved oxygen are needed to understand when and how it has changed in the past and how the marine ecosystem has been impacted. Looking at past levels of dissolved oxygen requires the use of a sediment proxy. For a sediment proxy to be reliable, it must be sensitive to changes in dissolved oxygen without being sensitive to other abiotic and biotic factors (Lu et al. 2010).

In the ocean, iodine exists in two oxidation states, iodide (I^-) and iodate (IO_3^-). When ocean deoxygenation occurs, iodate is reduced to iodide. The redox potential of iodate to iodide is similar to the redox potential of oxygen to water (Lu et al. 2010). Iodate thus has the potential to form calcium iodate $Ca(IO_3)_2$ and be incorporated into calcium carbonate by substituting for the carbonate ion (Lu et al. 2010). Iodide cannot be incorporated within this structure. This difference in behavior suggests that iodine ratios in calcium carbonate can become a potential dissolved oxygen proxy (Lu et al. 2010).

Foraminifera are sources of calcium carbonate formed from seawater that can be found in sediment cores. Different species of foraminifera live in different locations of the water column allowing us to look at the differences in iodine-to-calcium ratios in foraminifera from the surface where there are high levels of oxygen and the thermocline where the level of dissolved oxygen is much lower (Rohling et al. 2004). The purpose of this project was to determine if iodine could be a suitable proxy for hypoxic regions and what modifications the method may need for this proxy to be effective.

METHODS

Sample selection – ODP 1240A was recovered from the Eastern Equatorial Pacific at latitude 0°1.311´N and longitude 86°27.758´W. This core was selected for its location near the eastern tropical Pacific OMZ as well as its abundance of foraminifera. The samples used were estimated to be 1000 years old (Robinson et al. 2009).

ODP 1242 was located within the OMZ. However, it contains significantly fewer foraminifera than ODP 1240A. Samples from Site 1242 were selected to reconstruct a downcore record spanning from the mid Pleistocene to early Pliocene when the OMZ is posited to have expanded (Robinson et al. 2014).

Bulk sediment samples were placed in 50-mL centrifuge tubes with a 2% hexamethphosphate solution and placed on a shaker table overnight. The samples were sieved the following day using a 150-μm sieve. The >150-µm fraction was dried and transferred to a 50-mL centrifuge tube. Using a binocular microscope, the species *Globigerinoides sacculifer* and *Globigerinoides ruber* were picked and separated as surface foraminifera and *Neogloboquadrina dutertrei* was picked as a thermocline foraminifera. Subsamples of the picked foraminifera were separated in 0.5-mg samples and transferred to labeled 2-mL centrifuge tubes.

Cleaning – Foraminifera were gently crushed between two microscope slides and transferred back into a centrifuge tube. One mL of Milli-Q water was added, and the mixture was agitated by a pipet. After the foraminifera settled to the bottom, the liquid was pipetted off. This was repeated two more times, and then repeated using methanol. After rinsing, 250 µL of 1% hydrogen peroxide buffered by 0.1M sodium hydroxide were added to each sample, and the samples placed in a hot water bath (80 °C) for ten min. Halfway through, the samples were sonicated for 30 seconds. This was repeated once and the samples were rinsed with Milli-Q water 2-3 times. 250 µL of 0.01% nitric acid were added to each sample and sonicated for 30 seconds. The acid was quickly pipetted off, and the samples were rinsed with Milli-Q water two times.

Measurement and Preparation – Samples were dissolved in 1 mL of a solution of 0.5% nitric acid and 0.5% tetramethylammonium hydroxide (TMAH) overnight and centrifuged for 4 min. The supernatant was transferred to clean microcentrifuge tubes. Each sample was diluted in a matrix of 0.5% nitric acid and 0.5% TMAH to attain ~2 ppm calcium for final analysis. Standards of varying iodine-to-calcium ratios were prepared in a matrix of 0.5% nitric acid and 0.5% TMAH (Dickson et al. 2014). A KIO_3 salt was used to make the I standard. Measurements of masses for Ca (43) and I (127) were made on the inductively coupled plasma mass spectrometer (ICP-MS) in the Kelley Laboratory at GSO-URI.

RESULTS

In samples taken from Site 1240, the surface samples had an average I/Ca of 251.7 μmol I per mol Ca (µmol/mol) with a standard deviation of 203.62. The thermocline samples for Site 1240 had an average ratio of 49.45 µmol/mol with a standard deviation of 54.47. Samples from Site 1242 had variable levels of iodine to calcium, between 402.5 µmol/mol to 1.9 µmol/mol (Fig. 1). Several samples were removed from the final data analysis because they contained iodine concentrations lower than the nitric TMAH blank. JCP-1, a calcium carbonate standard from coral, was run as an unknown and we measured an average I/Ca of 3.48 µmol/mol.

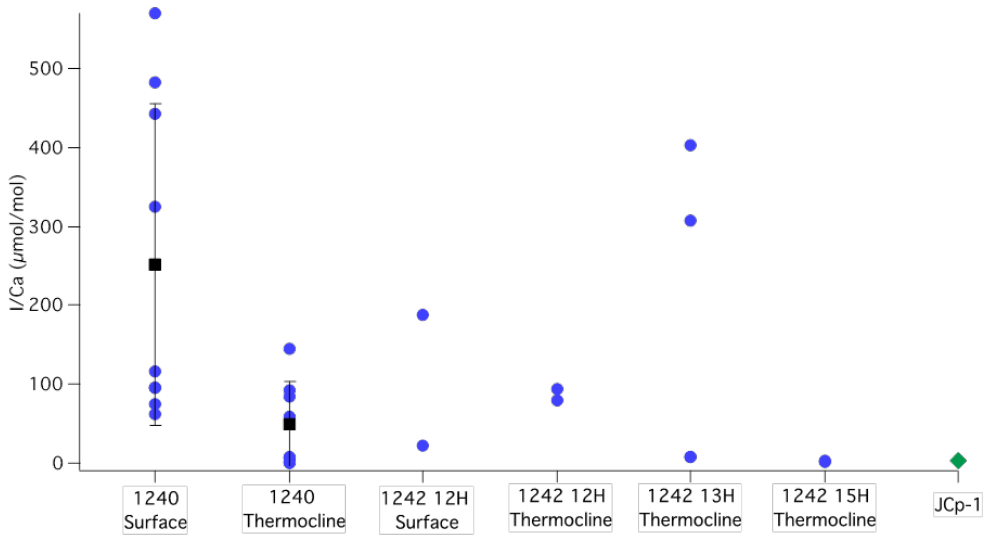

Fig. 1. I/Ca values for samples and standards measured above 0 in μmol/mol. The black square on the 1240 samples shows the average and standard deviation of the measured samples. JCP-1 was measured at an average value of 3.48 μmol/mol.

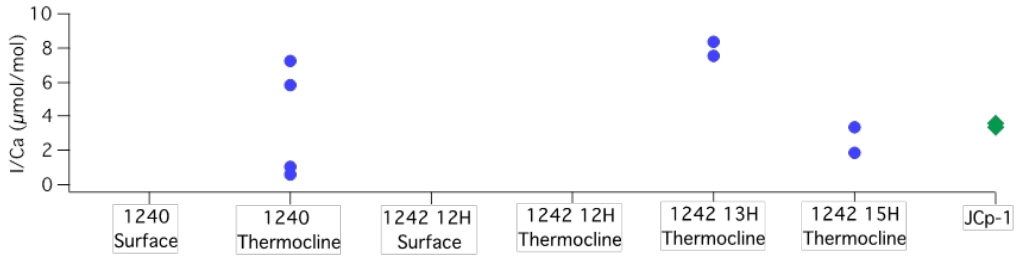

Fig. 2. Measurements within published I/Ca values as well as JCP-1

DISCUSSION

Expected ratios of iodine to calcium in foraminifera are between 0-8 μmol /mol (Lu et al. 2010). Our results showed much higher values than the published values as well as a high range of values. JCP-1 has a known iodine-to-calcium ratio of 4 µmol/mol (Lu et al. 2010; Glock et al. 2014) which is relatively close to the 3.48 μmol /

mol value we measured. There is only a 13% difference between the published value of JCP-1 and the measured value, whereas the 1240 surface samples were one or two magnitudes higher than the published range for I/Ca. 1240 thermocline sample splits 1, 2, and 3 had measurements within published values whereas split numbers 4 and 5 had values an order of magnitude higher. Samples 1242 13H4 thermocline split 3 and 1242 15H2 surface split 1 had measurements within published values as well (Fig. 2). The rest of the samples either had levels of iodine that were below the blank or iodine-to-calcium ratios that were at least one magnitude higher than published values.

The small difference in the known measurement of JCP-1 and our measurement of JCP-1 indicates that it is possible for us to make these measurements on the ICP-MS with some level of accuracy. This implies that our measurements for the other samples were relatively accurate measurements of what was in each sample. For the measurements to have such high levels of iodine while still being accurate there must have been contamination during the cleaning process or incomplete cleaning. Organic matter contains iodine (Tsunogai et al. 1971). The hydrogen peroxide used in the cleaning removes this organic matter. In the procedure discussed by Lu et al. (2010), after this step, the foraminifera were transferred to clean centrifuge tubes. In our cleaning process, we did not transfer the samples to clean centrifuge tubes after this step. Iodine that was leached off of the organic material while the hydrogen peroxide was in the sample could have stuck to the surfaces of the centrifuge tube and, since we did not switch tubes, it was available to reenter the sample during the dissolution step. It is also possible that not all of the organic matter was removed from the samples and this organic matter could have added iodine to the samples when it was dissolved (Yamaguchi et al. 2008).

The I/Ca values were not uniformly high, suggesting that incomplete cleaning may have been the cause of the inconsistent high values, but contamination is still a possibility. The buffered hydrogen peroxide that was used to remove organic matter was left in the samples for 10 min, and this step was repeated once. It is possible that this step could have required more time due to the high levels of organic material at both sites or a stronger concentration was needed.

CONCLUSION

Before we can assess whether I/Ca can be used as a proxy for ocean oxygenationn in hypoxic zones, the cleaning method needs to be perfected and better data generated. A longer wait period during the organic matter removal step, using buffered hydrogen peroxide, or using a stronger concentration could help remove any excess organic material from the samples. Changing centrifuge tubes more often may also limit contamination.

ACKNOWLEDGMENTS

We would like to thank Katherine Kelley for allowing us to use her lab facilities and microscope as well as running our standards and samples on her ICP-MS. We would also like to thank Bruce Corliss with help in initial foraminifera identification. Funding for this project was provided by NSF.

REFERENCES

Deutsch, C., Brix, H., Ito, T., Frenzel, H., Thompson, L.,2011. Climate-forced variability of ocean hypoxia. Science 333 doi: 10.1126/science.1202422

Glock, N., Liebetrau, V., Eisenhauer, A., 2014. I/Ca ratios in benthic foraminifera

from Peruvian oxygen minimum zone: analytical methodology and evaluation as a proxy for redox conditions. Biogeosciences 11: 7077-7095 doi: 10.5194/bg-11-7077-2014

Lu. Z., Jenkyns, H., Rickaby, R. 2010. Iodine to calcium ratios in marine carbonate as a paleo-redox proxy. Geology 38: 1107-1110

Rohling, E., Sprovieri, M., Cane, T., and others. 2004. Reconstructing past planktic foraminiferal habitats using stable isotope data: a case history for Mediterranean sapropel S5. Marine Micropaleontology 50: 89-123

Stramma, L., Johnson, G., Sprintall, J., Mohrholz, V. 2008. Expanding oxygen-minimum zones in the tropical oceans. Science 320: 655-657 doi: 10.1126/science.1153847

Tsunogai, S. 1971 Iodine in the deep water of the ocean. Deep Sea Research and Oceanography Abstracts 18(9): 913-919

Yamaguchi, N., Nakano, M., Takamatsu, R., Tanida, H. 2008. Inorganic iodine incorporation into soil organic matter: evidence from iodine K-edge X-ray absorption near-edge structure. Journal of Environmental Radioactivity 101(6): 451-457 doi: 10.1016/j.jenvrad.2008.06.003

Zhou, X., Thomas, E., Rickaby, R., Winguth, A., Lu, Z. 2014. I/Ca evidence for upper ocean deoxygenation during the PETM. Paleoceanography 29(10):964-975. doi: 10.1002/2014PA002702

F. Rodier is in the Department of Biology at Salem State University Salem, MA (f_rodier@salemstate.edu)
Rebecca Robinson (rebecca_r@uri.edu)

Spring High Tides and Inundation Risk at Four Northeastern Coastal National Parks

Nicole Statler, Amanda Babson
Graduate School of Oceanography, University of Rhode Island, Narragansett, RI, 02882

Abstract

This project analyzed spring high tides by using the tidal datum mean high water spring (MHWS) and determined inundation risk at four northeastern coastal national parks. We created two tools in the statistical program R, to find MHWS. The first compares elevations of the desired location to a control station. The second and more accurate tool finds and averages all the spring high tides. Record length (between 3-9 months) for various parts of the year at three stations was tested to determine how long of a record is needed to produce an accurate MHWS value. For six months of record length, 87% of the MHWS values had an error of 10 cm or less when compared to the MHWS value found over an entire tidal epoch. The ratio of MHWS to mean high water (MHW) at all the locations except Buntings Bridge at Assateague Island National Seashore had similar ratios. Buntings Bridge's ratio was smaller, approximately half the size of the other locations including other microtidal sites. The inundation risk due to sea level rise (SLR) for MHWS was then compared to that of MHW to see if there was a difference between the datums under scenarios of 60 cm, 1 m, and 2 m of SLR. Buntings Bridge was the only location where the land was inundated under MHWS but not MHW; this occurred for SLR of 60 cm. SLR trends in MHWS and MHW were compared by looking at long term annual averages.

The rate of SLR along New England's coastline is accelerating (Boon, 2012). With increasing sea level comes increasing risk in terms of inundation or flooding. Typically, analysis of inundation risk has used the mean sea level or mean high water (MHW) datum, but inundation risk during spring tides is also of management concern. During times of spring tides, the tidal range is greater, resulting in higher high tides (NOS, 2007). The mean high water spring (MHWS) datum is higher than the MHW datum, introducing a greater chance of flooding. Shaw and Bradley (2014) modeled sentinel sites, locations with resources of interest (Murdukhayeva, 2013) at Northeast coastal national parks that would become inundated if the MHW datum increased 60 cm, 1 m, and 2 m due to SLR. The National Park Service (NPS) is working on obtaining an accurate description of inundation risk associated with SLR trends at northeastern coastal national parks for coastal adaptation planning on reducing flood risk to infrastructure and cultural resources. Marsh vegetation is affected by where the marsh resides in the tidal range. Where the marsh sits in the spring tidal range will change how much flooding the marsh receives and affect the vegetation. By knowing MHWS, the NPS will be better able to know the upslope migration of marshes and prioritize marsh restoration projects. The National Oceanic and Atmospheric Administration (NOAA) does not have a long-term tide gauge at every park; even when there is a long term station, there can be significant differences between two locations within the park, so the NPS and other groups put out sensors, but only for short time periods. Therefore it is important to know how long of a record is needed to compute MHWS at a desired

accuracy. The purpose of this project is to determine the MHWS value at locations within four of those parks: Assateague Island National Seashore (ASIS), Boston Harbor Island National Recreation Area (BOHA), Fire Island National Seashore (FIIS), and Gateway National Recreation Area (GATE), and assess the inundation risk at select locations for the same three SLR scenarios but using MHWS instead of MHW.

METHODS

Data sources – Water level elevations were collected from various sources and are relative to the North American Vertical Datum of 1988 NAVD88. Many of the analyses were done using water levels collected at six-minute intervals and verified daily highs and lows for 1983 through 2014 for Sandy Hook (station ID 8531680) at GATE because NOAA has a long term tide gauge there. Verified water levels collected at 6-min intervals, daily highs and lows, and monthly mean values were obtained from NOAA tide gauges for The Battery, NY (station ID 8518750), Lewes, DE (station ID 8557380), Montauk, NY (station ID 8510560), Ocean City Inlet, MD (station ID 8570283, and Boston, MA (station ID 8443970) for the years 1996 through 2015. If there were any missing values in the data, NOAA's astronomical predicted levels that are determined using tidal harmonic analysis (NOS, 2007) were used to fill the gaps. The School of Marine and Atmospheric Science at Stony Brook measures and reports water levels every six minutes for Bellport, NY for their Great South Bay Project. The instrument used is the SBE 16plus SeaCAT, a pressure sensor to measure water level. Due to there being gaps, the data were broken up into multiple time periods, starting at December 5, 2014 and ending July 22, 2015. Lastly, data ranging from February 8, 2013 to March 6, 2014 for Buntings Bridge were used. These data are collected by a NPS Microwave Water Level (MWWL) sensor that is assembled and operated by NOAA CO-OPS for NPS.

Determining inundation risk at sentinel sites at 12 northeast coastal national parks during mean high water (MHW) under three SLR scenarios was conducted by URI's Environmental Data Center (Shaw and Bradley, 2014). Our study used their reported Light Detection and Ranging (LiDAR) and real-time kinematic global positioning system (RTK GPS) elevations, MHW value, and whether the site was inundated for the SLR scenarios of 60 cm, 1 m, and 2 m. Ground truthing found the mean LiDAR accuracy to be plus or minus 15 cm, but can have an error of up to a meter (Gao, 2007). The accuracy of RTK GPS is within 2 – 4 cm (Gao, 2007).

The accepted datum values for MHW, mean low water, mean tidal level, and mean range of tide were obtained for Montauk, The Battery, Boston, Lewes, Ocean City, and Sandy Hook. These datums are reported by NOAA and are from the last tidal epoch (1983 – 2001). A tidal epoch is a 19-year period over which water level elevations are averaged to determine the tidal datum of interest (NOS, 2000). The 19-year period was accepted by the National Ocean Service because that is the required time length to account for all variations in sea level (NOS, 2000). The principal solar semidiurnal constituent for The Battery, Lewes, Montauk, and Ocean City Inlet was obtained from NOAA.

Comparison tool – The comparison tool is a function in the statistical program R, designed to calculate MHWS. The tool uses tide gauge data from both the desired location and a control station for the same time period. The first part of the tool calculates the daily high and low tides and

the monthly mean values. The second part of the comparison tool uses the Modified-Range Ratio Method (NOS, 2003) to correct the mean range of tide for the desired location. Then the two methods described by Marmer (1951) are used to determine MHWS: the harmonic constituent method for the control station and the comparison equation for the desired location.

For FIIS, the comparison tool was used at Bellport using Montauk and The Battery as the control station. Due to gaps in the data and from testing the comparison tool (the accuracy of the tool was similar for various record lengths), the longest continuous record which is from April 22, 2015 through June 28, 2015, was used. For both Montauk and The Battery, verified monthly mean water level values for April 2015 to June 2015 were used to do the comparison. For ASIS, the comparison tool was used at Buntings Bridge with Ocean City Inlet as the control station. Ocean City Inlet's 6-min water level data from February 8, 2013 to March 6, 2014 were used because that is length of available data for Buntings Bridge.

Averaging tool – The averaging tool is a second tool in R. MHWS is defined by NOAA as, "the average height of the high waters of the spring tides" (NOS, 2000). This tool gets MHWS by finding the greatest tidal range occurring at the date of the new or full moon plus the phase lag and averages the height of the high water associated with the greatest tidal range and the successive high tide (McInnes et al. 2009). The average of all the spring high tides is then taken. The averaging tool was used to determine a 19-year average at Sandy Hook for the last tidal epoch (1983-2001) and the last 19 years (1996-2014).

Length of Record and Accuracy – To determine the needed length of a record and the accuracy of both tools, record lengths varying from three to nine months at one-month intervals were tested for Sandy Hook for the year 2014. Each record length was tested at different parts of the year to look at the influence of the seasons. For the comparison tool, The Battery and Lewes were used to show the influence of a control station on the accuracy of the MHWS value. The MHWS value obtained through this testing was compared to the 19-year average calculated for the last 19 years (1996-2014) to determine the accuracy. For all stations, verified 6-min water levels were used.

Ocean City Inlet has only 13 years of data available, but is the longest available station for Assateague Island National Seashore, and was used as the control station for Buntings Bridge. The accuracy of using 13-years of data compared to 19-years was tested using the averaging tool. Then seven 13-year periods ranging from 1996 to 2014 were tested to determine an average uncertainty value for a 13-year interval at Sandy Hook using the verified daily high and low water level data.

To determine if the accuracy of the averaging tool was general and not specific to Sandy Hook for 2014, various six-month intervals were tested at Sandy Hook for 2011 and 2013, Ocean City Inlet for 2014, and Boston for 2014. Five seven-month and one ten-month intervals for 2014 were also tested at Boston.

Other datums – Mean high water, mean low water, and mean range of tide were calculated by using the Modified-Range Ratio Method simultaneous comparison method described by NOAA (NOS, 2003). Direct averages were taken to determine MHW and mean low water. The difference between those two averages was used to determine mean range of tide.

Inundation – Using static (bathtub) inundation modeling, not accounting for

storm surge or dynamic landform response, Shaw and Bradley (2014) used the scenarios 60 cm, 1 m, and 2 m to determine flooding risk associated with MHW at all the sentinel sites. This study also used the bathtub inundation scenarios of 60 cm, 1 m, and 2 m, but used the MHWS datum. Select sentinel sites, used for inundation comparison, were chosen based on proximity to one of the tested tide gauge sites, if MHW was given, and if there was at least one scenario where the sentinel site was not inundated. To determine MHWS for the sentinel site, the difference between MHW and MHWS for the tested site was added to the MHW elevation of the sentinel site. This estimated MHWS value was then compared to the LiDAR and RTK-GPS elevation at the sentinel site under the three SLR scenarios. For the sentinel site near Boston, the NAVD88 ortho height determined by the National Geodetic Survey for station MY0015 was used.

Sea level rise – To compare SLR trends for MHW and MHWS the program R was used to create regression equations. Average MHWS elevations for each year at Sandy Hook from 1983 to 2014 were plotted and then using the linear regression function, a best fit line was produced. The same approach was followed for MHW.

RESULTS AND DISCUSSION

Comparison of tools and record lengths – The accuracy of the two tools was compared to the 1996-2014 MHWS to determine which of the two tools is more accurate. The MHWS value at Sandy Hook for the current National Tidal Datum Epoch (NTDE) (1983 – 2001) is 0.77 m. The MHWS value for the past 19 years (1996-2014) is 0.81 m as determined using the averaging tool. For Boston, the MHWS value for the past 19 years is 1.56 m. Since Ocean City Inlet only has 13 years of data available, the 13-year average is 0.32 m.

The MHWS for the current NTDE and for the most recent 19-year interval were compared to see how the datum has changed. There is a 0.04 m difference between calculating MHWS over the current NTDE and over the most recent 19-year interval at Sandy Hook. SLR is considered the main reason for this difference, but was not tested. Since the most recent National Tidal Datum Epoch does include any data past 2001, any SLR that has happened since then, is not accounted for. When using the most recent 19-years of data, SLR is included in the datum value. Most of the data the park service are using is more recent than the National Tidal Datum Epoch, so it would be more fitting to use the last 19-year MHWS. When using The Battery as the control station for Sandy Hook when testing the comparison tool, the difference from the most recent 19-year MHWS and the comparison tool MHWS ranged from 0.96 to 0.97 m for all the record lengths used. Similarly, when using Lewes as the control, the difference for all the intervals tested ranged from 0.62 to 0.63 m. An important factor when using the comparison tool is the selection of the control station. Control stations are used to correct short-term stations datums to an equivalent 19-year value. Using Lewes as the control produced results that were about 0.3 m more accurate than when using The Battery. If there is not a representative control station to choose from, the accuracy of the comparison tool greatly decreases.

When testing how long a record is needed to calculate MHWS with reasonable accuracy at Sandy Hook for 2014 we found that for six months or more, the accuracy was less variable and greater than the accuracy of records lengths less than six months (Table 1). While there is some variation in the error between the six-

through-nine-month record lengths, it was 5 cm or less for all the cases tested. From these results we determined that at least six months of data should be used for the averaging tool.

Table 1. Length of Record Testing For Averaging Tool, Sandy Hook 2014

Number of Months	Intervals	MHWS (m)	Difference from 1996-2014 Average (m)
3	July – Sep	0.67	0.14
3	Oct – Dec	0.90	0.09
4	May – Aug	0.72	0.09
4	Sept – Dec	0.96	0.15
5	Aug – Dec	0.90	0.09
5	April – Aug	0.71	0.10
6	Jan – June	0.86	0.05
6	July – Dec	0.78	0.03
7	Jan – July	0.76	0.04
8	Jan - Aug	0.76	0.05
9	Jan – Sept	0.80	0.01

Results for testing six-month record lengths at Ocean City Inlet for 2014, Boston 2014, and Sandy Hook for 2011 and 2013 are shown in Table 2. January through June for Ocean City Inlet had an error of 10 cm. An error of only 2 cm was produced for Ocean City Inlet during March through August. Boston had errors of 9 cm and 7 cm for January through June and March through August respectively (Table 2). Testing the year 2011 at Sandy Hook gave a result with an error of 2 cm and 2013 had 7 cm. The year and the location do influence the accuracy, but there were no clear patterns in the degree of spatial and interannual variability, so based on this analysis we cannot estimate conditions that produce the larger errors. The NPS typically deploys water level recorders for three to six months. If the NPS were interested in calculating MHWS to 10-cm accuracy, then the water level recorders would need to be in for at least six months. A 10-cm error is reasonable when using LiDAR-based elevations, however, it is not sufficient when comparing to RTK GPS. A longer record is needed to get an error within 2 – 4 cm.

To determine if using Ocean City Inlet as a control station, which does not yet have a full 19 years of data available, was appropriate, seven 13-year periods were tested at Sandy Hook (Table 3). The average error of the seven 13-year periods tested at Sandy Hook is one centimeter with the maximum error coming from 2002 through 2012. Ocean City Inlet was used as a control station for Buntings Bridge even though only 13 years of data are available. From testing the different year lengths of record, and the seven 13-year periods, we decided using Ocean City Inlet as the control station was appropriate, noting that there could be an additional 5 cm of error.

Table 2. Six-Month Record Length Testing For Different Years and Locations.

Location	Date	Averaging Tool MHWS (m)	Difference from 1996-2014 Average (m)
Ocean City Inlet, MD	Jan – Jun, 2014	0.22	0.10
Ocean City Inlet, MD	Mar – Aug, 2014	0.3	0.02
Ocean City Inlet, MD	April – Sept, 2014	0.36	0.05
Boston, MA	Jan – Jun, 2014	1.47	0.09
Boston, MA	Mar – Aug, 2014	1.50	0.07
Boston, MA	April – Sept, 2014	1.48	0.08
Sandy Hook, NJ	Jan – June, 2013	0.70	0.07
Sandy Hook, NJ	April - Sept, 2011	0.79	0.02

Table 3. 13-year averages at Sandy Hook

Date	MHWS (m)	Difference from 1996-2014 Average (m)
1996 - 2008	0.80	0.01
1997 – 2009	0.80	0.01
1998 – 2010	0.79	0.02
1999 – 2011	0.78	0.03
2000 – 2012	0.78	0.03
2001 – 2013	0.81	0.00
2002 – 2014	0.81	0.00

MHWS and other datums – At the five locations, MHWS, MHW, mean low water, and mean range of tide were determined (Table 4). The comparison tool was used at Bellport with Montauk, NY and The Battery, NY as the control stations. Using The Battery produced a MHWS value that was 0.43 m greater than the MHWS obtained when using Montauk. The comparison tool value when using Montauk was 0.99 m greater than the averaging tool's MHWS. This large difference indicates that the comparison tool with Montauk as the control is not appropriate to use.

The comparison tool was not used to determine MHWS for Boston, MA and Ocean City Inlet, NJ. For Boston, 19 years of data were used in the averaging tool. The 13 years of available data at Ocean City Inlet were used in the averaging tool giving a MHWS value of 0.32 m. From our 13-year testing at Sandy Hook, the MWHS should be accurate to within 5 cm.

Ocean City Inlet, MD was used at the control station at Buntings Bridge, MD. The comparison tool's MHWS was 0.54 m. The averaging tool's MHWS was 0.17 m. Eleven months of data were used at Buntings Bridge so we expect the averaging tool to be within 10 cm of the actual value. The comparison tool's value was 0.37 m greater than the averaging tool.

Microtidal locations have tidal ranges of 0 – 2 m. Bellport, Buntings Bridge, Ocean City Inlet, and Sandy Hook are microtidal (Table 4). Boston has a tidal range of 2.90 m, making it mesotidal. Mesotidal locations have tidal ranges of 2 – 4 m (Table 4).

The ratio of MHWS to MHW was calculated at the five sites to determine the relationship between the two datums (Table 5). Buntings Bridge which is microtidal and located at Assateague Island National Seashore like Ocean City Inlet had a ratio that was about half the size of the other locations. Ocean City Inlet, Sandy Hook, Bellport, and Boston all had similar ratios. This project did not investigate why Buntings Bridge ratio was different from the other locations.

Table 4. Datum values for tested sites[1]

Location and Park	Comparison Tool MHWS (m)	Averaging Tool MHWS (m)	MHW (m)	Mean Low Water (m)	Mean Range of Tide (m)
Bellport FIIS	1.18	0.19	0.17	-0.16	0.43
Buntings Bridge ASIS	0.54	0.17	0.07	-0.13	0.20
Boston BOHA	NA	1.56	1.38	-1.52	2.90
Ocean City Inlet ASIS	NA	0.32	0.26	-0.37	0.63
Sandy Hook GATE	0.62	0.81	0.70	-0.77	1.47

[1] The reported MHW, MLW, and mean range of tide values were found by averaging all the highs, averaging all the lows, and taking the difference of those two averages, respectively. The comparison tool was not used at Boston and Ocean City Inlet. The comparison tool value for Sandy Hook is from using Lewes, DE as the control station and is the approximate value obtained for the different record length testing. The comparison tool value for Bellport is from using Montauk, NY as the control station.

Table 5. Ratio of MHWS to MHW

Location	Ratio
Buntings Bridge	1 : 0.41
Ocean City Inlet	1: 0.81
Sandy Hook	1: 0.87
Bellport	1: 0.87
Boston	1: 0.88

Inundation – Inundation risk due to MHWS under SLR scenarios of 60 cm, 1 m, and 2 m at northeastern coastal national parks sentinel sites was done to build upon the work of Shaw and Bradley (2014). Within Boston Harbor Islands National Recreation Area, the sentinel site, Georges Visitors Center, was tested. The difference between Boston's MHWS and MHW was added to the site's MHW to get an estimated MHWS value of 0.42 m. The NPS benchmark monument, MY0015's, NAVD88 ortho height of 2.40 m was used instead of the LiDAR elevation, because it has been selected as a coastal flooding indicator in the State of the Park report. For a SLR of 60 cm and 1 m, this site is not flooded. For a SLR of 2 m, the site is inundated. The flooding risk associated with MHW determined by Shaw and Bradley (2014) is the same as that of MHWS.

The difference between Sandy Hook's most recent 19-year MHWS and MHW was added to the sentinel site, Post Chapel at GATE, MHW to get the estimated MHWS of 0.77 m. The LiDAR elevation was 3.95 m. For all three SLR scenarios there was no inundation risk.

Within Fire Island National Seashore two locations were assessed for inundation risk. The difference between Bellport's MHWS and MHW was added to the MHW of sentinel site 851 4322 B Tidal Mark in Patchogue to get the estimated MHWS of 0.21 m. The site was not at risk for a SLR of 60 cm, but became inundated for a SLR of 1 m and 2 m. This assessment was the same for MHW. The other site tested was the NPS benchmark monument KU4471. Bellport's MHWS value was used at this location because a MHW value was not available and the site is in the vicinity of the Bellport station. The NAVD88 ortho height was 1 m. There was no risk for a SLR of 60 cm. The site became inundated for a SLR of 1 m and 2 m. The same risk assessment was found for MHW. The MHW risk assessment was done by using Bellport's MHW value.

At Assateague Island National Seashore, two sentinel sites were tested. The first sentinel site was 2010ASISBayr. The difference between Ocean City Inlet's MHWS and MHW was added to 2010ASISBayr's MHW value to get an estimated MHWS value of 0.47 m. The LiDAR elevation for the sentinel site is 1.63 m. Under a SLR of 60 cm and 1 m the site is not inundated. For a SLR of 2 m the land is inundated. The same flooding risk was determined for MHW.

The second sentinel site tested was 2010ASIS004. The difference between Buntings Bridge's MHWS and MHW was added to the sentinel site's MHW for an estimated MHWS. The LiDAR elevation was 0.88 m. For all three SLR scenarios the site was inundated. There was a difference between MHW and MHWS risk assessment for a SLR of 60 cm, the site was not inundated for MHW. This is the only location tested where MHW and MHWS had a different flooding risk. Bunting Bridge was the location with the smallest ratio of MHWS to MHW. The connection between the ratio and the inundation risk was not tested.

Sea level Rise – The annual averages for MHWS from 1983 to 2014 at Sandy Hook display an upward trend, but the line did not fit the data well, as shown by the low coefficient of determination, due to high variability in the data (Fig. 1). The linear regression line for MHW against time fits

the data better (Fig. 1). The rate of SLR trends for MHWS appears slower than the rate for MHW, but we were unable to conclude whether this difference is significant.

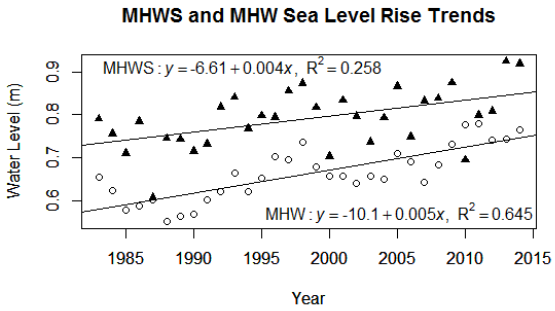

Fig. 1. Regression lines for MHWS (triangles) and MHW (circles) against time. Annual averages from 1983 to 2014 at Sandy Hook were used.

CONCLUSION

With sea level rising, inundation risk is becoming more of a concern; the NPS is working to get an accurate description of this risk. The MHWS value was calculated at five locations within four national parks. Two different methods of calculating MHWS were compared; the averaging tool was found to be more useful. Both tools are publicly available on GitHub. Tests on length of record showed that using at least six months of data to get a value accurate within 10 cm was needed. Sentinel sites from Shaw and Bradley (2014) nearby the tide gauge locations were chosen and an estimated value MHWS was used to determine the inundation risk of MHWS under the SLR scenarios of 60 cm, 1 m, and 2 m. At Buntings Bridge, the flooding risk of MHW and MHWS differed for a rise of 60 cm; the site was not inundated for MHW, but was for MHWS. The other locations tested did not have a difference in risk for these SLR scenarios between the two datums.

When looking at inundation risk associated with future SLR, it is important to look at not only MHW or mean sea level, but also MHWS in order to get the most accurate description of risk. With this more accurate description, coastal adaptation planners will be more knowledgeable and prepared. Since data were not available for the exact location of the sentinel sites, an estimated MHWS value was used, potentially affecting the risk assessment or the severity of the risk. One modification to this study for more accurate results would be to use RTK GPS instead of LiDAR. A second modification would be to either create a more accurate tool or have longer tide gauge data available for the exact sentinel site locations. To get a more complete inundation risk assessment, evaluating the hazard associated with perigean spring tides would be recommended.

ACKNOWLEDGEMENTS

This research was funded by the National Science Foundation (NSF) through the Summer Undergraduate Research Fellowship in Oceanography at University of Rhode Island's Graduate School of Oceanography. We are thankful to Jeff Hollister for helping getting the tools useable and available to the public. We acknowledge Dave Ullman and Thom Curdts for providing the data for Buntings Bridge.

REFERENCES

Boon, J. D. 2012. Evidence of sea level acceleration at U.S. and Canadian tide stations, Atlantic Coast, North America. J. Coastal Res. 28(6):1437-1445.

Gao, J. 2007. Towards accurate determination of surface height using modern geoinformatic methods:

possibilities and limitations. Progress in Physical Geography. 31(60):591-605.

NOS. 2000. Tide and current glossary, special publication 228. National Ocean Service, NOAA.

NOS. 2003. Computational techniques for tidal datums handbook, NOAA special publication NOS CO-OPS 2. National Ocean Service, NOAA.

Marmer, H.A. 1951. Tidal datum planes. Special Publication 135, revised ed. NOAA, National Ocean Service, U.S. Coast and Geodetic Survey.

McInnes, K.L., Macadam, I., and O'Grady, J. 2009. The effect of climate change on extreme sea levels along Victoria's coast a project undertaken for the Department of Sustainability and Environment, Victoria as part of the 'Future Coasts' program. CSIRO, 6.

Murdukhayeva, A., August, P., Bradley, M., LaBash, C., and Shaw, Nigel. 2013. Assessment of inundation risk from sea level rise and storm surge in northeastern coastal national parks. Journal of Coastal Research. 29(6A):1-16.

Parker, B. B. 2007. Tidal analysis and prediction, NOAA special publication NOS CO-OPS 3. National Ocean Service, NOAA.

Shaw, N. and Bradley, M. 2014. Assessing risk from climate change impacts of sea level rise and storm surge. 2010-2014. Project-2216861. https://irma.nps.gov/App/Reference/Profile/2216861

N. Statler is at the University of Portland, 5000 N Willamette Blvd. Portland, OR 97203 (statler16@up.edu)

A. Babson is with the Northeast Region, National Park Service, Narragansett, RI (amanda_babson@nps.gov)

3D flow visualization of the wake of a flexible cylinder undergoing vortex-induced vibrations using digital particle image velocimetry

Emma Thomas, Deniz Gedikli, Jason Dahl
Graduate School of Oceanography and Department of Ocean Engineering, University of Rhode Island, Narragansett, RI 02882

Abstract

Vortex-Induced Vibrations (VIV) have been studied for years due to problems they pose for marine structures that make use of long, cylindrical cables such as oil rigs and off shore wind energy systems. Due to the high cost and difficult implementation of obtaining 3D datasets, the wake of a cylinder undergoing VIV has typically been visualized using separate 2D slices oriented perpendicular to the vibrating cylinder. This method is limited to detecting vorticity within the sampled plane, and only provides data representing a single location along its length. In order to create a 3D reconstruction of such a cylinder's wake, we used Stereoscopic Digital Particle Image Velocimetry to obtain 2D vorticity fields of the flow at several different locations. Since the slices were recorded at different times, motion tracking of the cylinder was used to find the periodicity of the vibrations, allowing both the cylinder's motion and the shape of the water flow to be averaged across many cycles (or phase-averaged). Slices of the wake are recorded at 20 locations, spaced 1 cm apart along a cylinder with a diameter of 0.635 cm. Currently, a phase-averaged wake representing a typical cycle has been assembled using the z-component of vorticity, as in previous 2D experiments. The methods developed here, however, may be used to find vortices in other directions, and will ultimately allow for more accurate analysis of a range of similar experiments aimed at characterizing the shape of the wake of a flexible cylinder undergoing VIV.

Both the durability and cost-effectiveness of marine structures including off shore oil rigs and wind energy systems, tow lines, and mooring lines stand to be improved by a more comprehensive understanding of Vortex-Induced Vibrations. The problem of VIV includes many different interrelated issues, including the mode shape and frequency of the cylinder, the pattern of the wake it creates, the forces acting between the cylinder and the fluid, and how all of these are connected to one another. The shape of the 2D wake, specifically, has been studied extensively, resulting in the classification of vortex shedding modes (Williamson and Roshko 1988). Many different methods have been explored, from smoke visualizations (Griffin and Ramberg 1974) to Digital Particle Image Velocimetry (DPIV). Other experiments such as Gedikli and Dahl (2014) have used motion tracking software to visually track features on the cylinder, while yet others, e.g. Xu et al. (2009), make use of accelerometers and load meters to simultaneously track the cylinder and its wake. What the majority of experimental studies have in common is that they only present 2D information on the wake at any moment in time, and as such mostly deal with vorticity in only one direction (usually parallel to the cylinder).

There are multiple techniques used to obtain similar data in three dimensions, such as Volumetric 3D Velocimetry (Peterson et al. 2012), which requires a specialized triple-aperture camera, and the hydrogen

bubble method (Matsuzaki et al. 2004), which uses bubbles generated by the cylinder itself. Stereoscopic Digital Particle Image Velocimetry, a technique already widely used to obtain data within a 2D plane, has the potential to provide a 3D visualization across larger volumes and without extra equipment.

Digital Particle Image Velocimetry (DPIV) is a technique that uses neutrally buoyant particles to track water movement; before DPIV there were much slower PIV methods used for similar purposes (Willert & Gharib, 1991). Neutrally buoyant particles are mixed into the water, at a concentration that will allow accurate particle tracking; a laser, converted into a laser sheet with a cylindrical lens, illuminates the particles within its plane. Two high-speed cameras with slightly differing perspectives (making the process stereoscopic) take images as the experiment is carried out. The positions of particles in consecutive images are compared using cross-correlation to obtain velocities for each of the "interrogation windows" the images are divided into, producing a velocity field of the illuminated plane. The differing perspectives of the two cameras allow velocities perpendicular to the plane to be calculated, as well. DPIV, if stereoscopic, yields velocity fields with components in three spatial directions, but is limited to providing 2D vorticity fields.

This project uses phase-averaging techniques on Stereoscopic DPIV produced velocity and vorticity fields to construct a 3D visualization of a flexible cylinder's wake over a typical cycle. By tracking the motions of the cylinder simultaneously, these methods will hopefully provide 3D vorticity data that may be visualized to better understand how the shape of such a cylinder's wake corresponds to its behavior. Additionally, continuous 3D velocity fields will potentially reveal vorticity components in multiple directions, creating a more accurate complex picture of a VIV associated wake.

METHODS

Setup & initial testing – Data were collected using a recirculating open water flow channel with glass viewing walls providing side, bottom, and head-on views such that both inline and crossflow movements could be observed. A black 30A neoprene rubber cylinder, diameter 0.635 cm with 25 round white dots at 1 cm intervals along its length was stretched horizontally across the channel and affixed to the side of the flow channel with suction cups. In order to allow motion perpendicular to the cylinder's orientation (but not along the cylinder), the suction cups are joined to the cylinder at either end with U-joints. Round plastic plates, with a diameter ten times that of the cylinder, were situated between the U-joints and suction cups to provide a flat surface for vortices to end on. All trials were conducted with the flow set at 0.17 m/s, and images of the cylinder & wake were recorded at a speed of 250 Hz by two high-speed Vision Research Phantom V10 cameras.

Given that DPIV requires both cameras capturing images of the same plane, preliminary tests were conducted using one camera to capture the cross-flow motion of the cylinder and the other to capture in-line motion. The white markers were placed on the surface of the cylinder at right angles (2 at each distance), so that the footage of both the inline and crossflow motion would include features that can be used for motion analysis. Footage was captured for a period of 8 s, and then exported from LaVision software as .avi files. The motion of the cylinder was tracked using ProAnalyst to obtain a typical cycle of motion.

Stereoscopic DPIV – Digital Particle Image Velocimetry uses a time-series of images to calculate the velocity field of a 2D plane. Stereoscopic DPIV, as is used in these experiments, uses the differing perspectives of two cameras to obtain velocity components within this plane as well as components perpendicular to it, though the locations of data points are still confined to the plane. In order to obtain these components for the entire 3D volume of the cylinder's wake, stereoscopic DPIV was carried out for multiple planes lining up with the 20 marked locations along the cylinder's length.

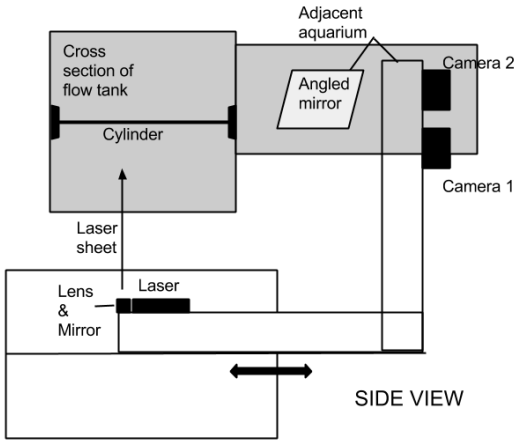

Fig. 1. A schematic diagram of the stereoscopic DPIV set up, viewed from the side with the water flowing into the paper.

A class 4 laser with a wavelength of 532 nm was situated underneath the flow tank, illuminating the seeded particles at an angle so as to minimize the cylinder's shadow across the wake. Additionally, changing either the distance between the laser sheet and the cameras or the ratio of water to air between them renders the software's calibration inaccurate. To deal with this, the laser and both cameras were held at a constant distance from one another on a structure that allowed the position of the entire system to be adjusted. To solve the problem of the water-to-air ratio, the cameras were directed not at the tank's viewing window but at an angled, underwater mirror in a smaller, adjacent tank. The entire setup is diagrammed in Fig. 1 and Fig. 2. Images were again recorded for a duration of 8 s at each plane with a frame rate of 250 Hz. Due to the angle of the cameras and the size of the suction cups, the last 5 dots were not visible, so there are only data on the first 20 points, starting on the far side of the tank.

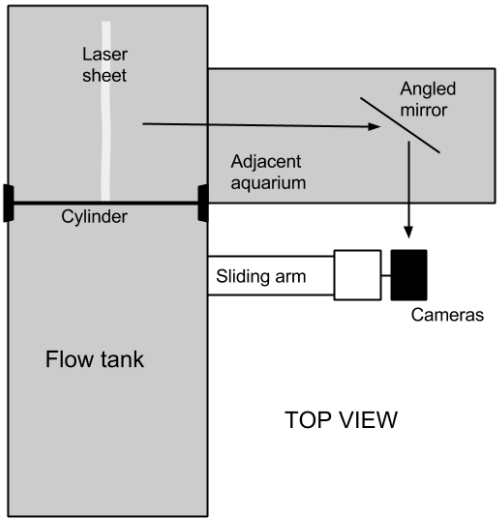

Fig. 2. A schematic diagram of the stereoscopic DPIV set up viewed from the top, with the water flowing from the bottom to the top of the diagram.

Data Analysis & Visualization – LaVision DPIV software was used to obtain a 2D vorticity field for each of the 20 slices; this only included the vorticity's z-components since a spatial derivative in the z-direction (across multiple slices) is required for x- or y-components. In order to compile planes of data taken at different times into a single representative cycle of motion, they must be phase-averaged using known characteristics of the cycle.

Obtaining Phase & Phase Averaging – Fig. 3 depicts an example image taken as part of the time-series for each slice. The smaller

white dots are the seeding particles; the laser reflecting off the edge of the cylinder results in the larger white smudge. Whereas PIV software uses particle-tracking of the seeding particles to produce velocity and vorticity fields, using the simpler ProAnalyst to track the cylinder's crescent in a time-series of PNG images exported from LaVision can provide information about the periodicity of the whole process. To this end, filters were applied to the original image, making the crescent more distinct and therefore more easily tracked (Fig. 4). A calibration was also applied that set the origin of the tracking data in the same location as in the PIV data, using the axes included in the exported image series as a guide. This tracking process was repeated for each of the twenty 2000-frame time series corresponding with their respective planes.

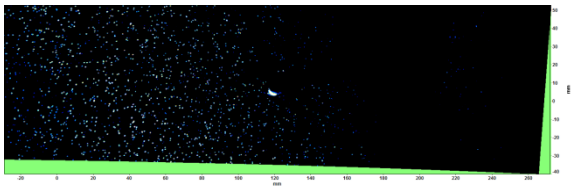

Fig. 3. An example frame taken during the DPIV process. The white crescent indicates where the laser is reflecting off the edge of the cylinder. The edges of the image are skewed because the frame is calibrated to provide a head-on perspective (as opposed to the original, angled view of the camera).

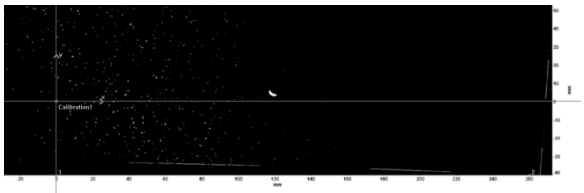

Fig. 4. The same frame, with filters applied so the crescent is more easily tracked.

The resulting tracking data were then used to assign a phase value between $-\pi$ and π to each frame of the corresponding time-series, via the MATLAB script instf.m. These phase values were converted to degrees (from 0° to 360°) and divided into 10° sections, resulting in 36 phase bins. The vorticity data from every frame assigned a phase within a given bin were averaged with all of the other data falling within that phase bin. For instance, 75 out of the 2000 images might fall within the first bin for a given slice's time series, and the average of their data provides a single representative beginning to the cycle. Due to time constraints, only every tenth data point was included and this was carried out just for slices 7 to 17.

Visualization – The cylinder tracking data for each slice were similarly phase-averaged and assembled to provide the cylinder's shape and position at each phase of the averaged cycle. As with vorticity, slices were phase-averaged separately from one another and all of the data for a given phase combined into a 3D representation of the cylinder's position at that phase. This revealed which positions in the cylinder's cycle correspond with specific stages of its wake.

Due to small variations in the cylinder's position at each slice, however, the combined segments did not produce a coherent mode shape without significant adjustments. Rather than use absolute position coordinates, it proved more practical to instead visualize how each segment oscillated around a given center point at which the whole cylinder presumably takes the shape of a straight, completely horizontal line. The preliminary tests in which the full cylinder's motion was tracked allowed for this position, and the phase at which it occurs, to be found. Using the instf.m script, phases were assigned to each of the 2000 positions of the cylinder. The phase values with the lowest standard deviation of point positions along the

cylinder were recorded. Finally, the position of each segment at the bin in which most of these phase values fall was subtracted from all of that segment's data. For instance, if most of the phase values with low standard deviations fell between 70-80 phase degrees, each segment was normalized according to its position during the 8th bin. In order to make sure the relative positions of the cylinder and the wake were correct, the coordinates of the vorticity field data are given the same offsets as the cylinder segments.

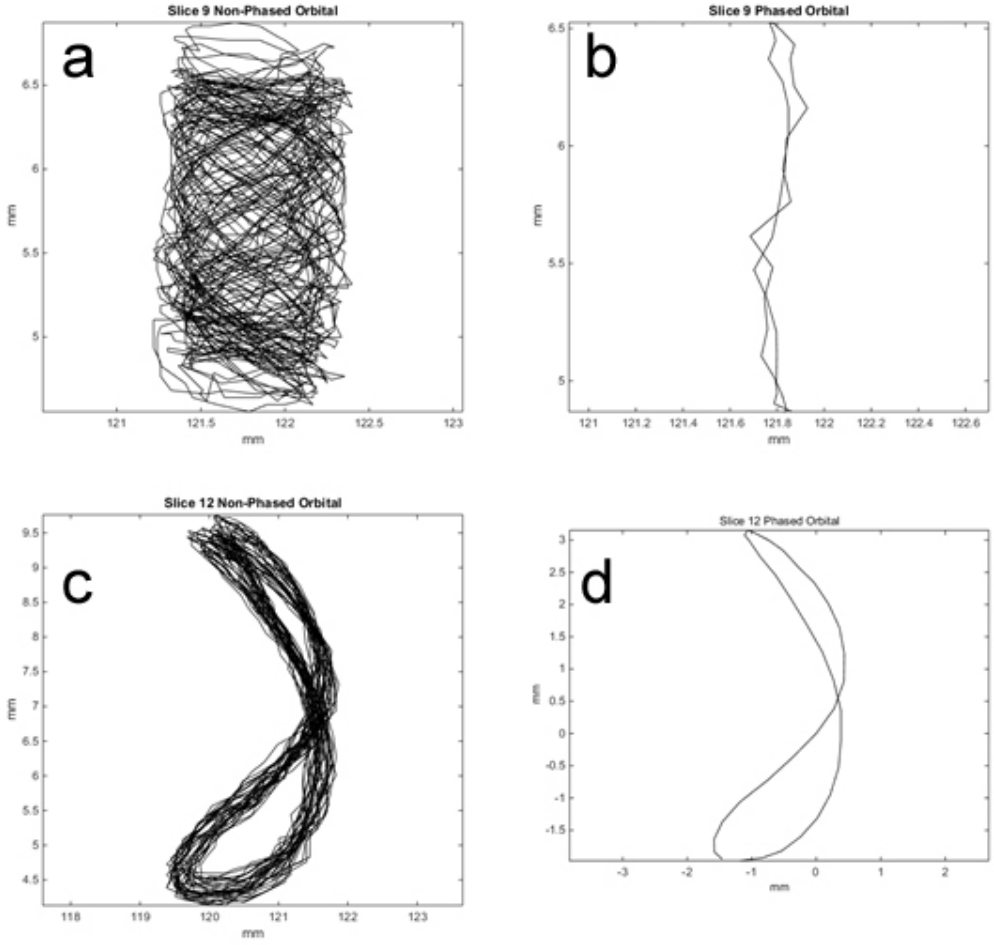

Fig. 5. (a) The path traced by the cylinder's 9th cross section's movement in the xy-plane, over the entire recording. This contrasts to the figure-eight crescent shape seen in other slices' orbitals/ (b) The result of attempting to phase-average this orbital. (c) The path traced by the 12th cross section's movement, which has a much more recognizable pattern and is more representative of the rest of the cylinder. (d) The phase-averaged orbital of the 12th slice.

Additionally, the position given by the tracking data was shifted for each cylinder upwards by a distance of the radius of the cylinder and at an angle of pi/4. While assuming the tracked point was located exactly on the bottom left edge of the cylinder was not very precise, fitting a circle of the correct radius to some of the crescents and finding their coordinates confirmed that this method caused no major anomalies.

The final, adjusted cylinder and wake data were written into 36 VTK unstructured grid

and structured grid files, respectively (one for each phase), and loaded into Paraview, where the averaged cycle of both may be viewed either as individual images or animated.

RESULTS

All phase-averaged cylinder orbitals except for slice 9 confirm that this procedure can give reasonable and synchronized data. Whereas most other points had distinctive, expected curved figure-8 shapes, the motion occurring when the data at slice 9 were taken appears to have been much more erratic (Fig. 5a). This results in a nearly meaningless average cycle (Fig. 5b). In contrast, slice 12, a typical representation of the rest of the data, traces a slightly varying but consistent orbital (Fig. 5c). This results in a reasonable looking and more useful average cycle (Fig. 5d). Therefore, the actions of the ninth cylinder segment in the positions of segments 8 and 10. When the orbitals for all slices are compared (Fig. 6), including this virtual 9th point, it is easy to see that they all represent similar behavior.

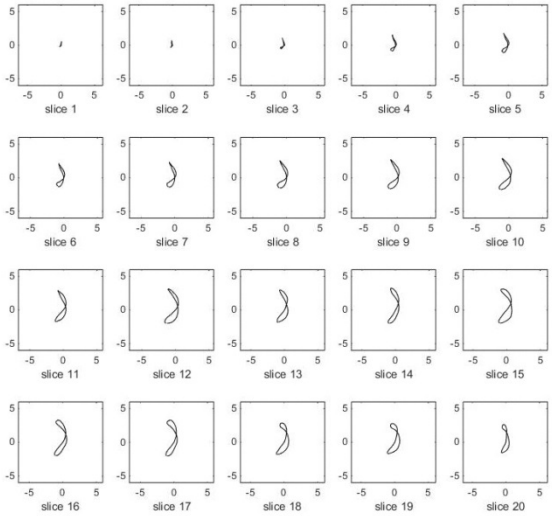

Fig. 6. Phase-averaged orbitals for every recorded slice, with slice 9 adjusted to be the average of slices 8 and 10.

The entire crossflow motion as recorded in the initial tests is depicted in gray in Fig. 7, with the length of the cylinder on the horizontal axis and its oscillation amplitudes on the vertical. The 20 frames with the lowest standard deviation of amplitude are highlighted in black, demonstrating the center position of a typical crossflow oscillation. The phases of these 20 frames are plotted against all phases (Fig. 8) and are shown to all occur roughly at the same point in the cycle, supporting this as an accurate strategy to normalize the cylinder's position data.

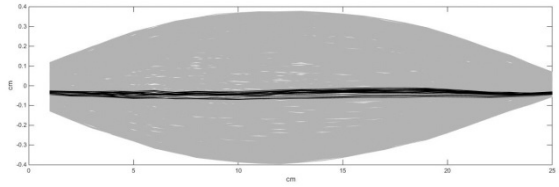

Fig. 7. The transverse movements of the cylinder are plotted, with the distance along the cylinder on the horizontal axis and its displacement perpendicular to the flow on the vertical. Each line represents the cylinder's position in one frame; the highlighted black lines are those with the lowers standard deviation in vertical positions across the length of the cylinder.

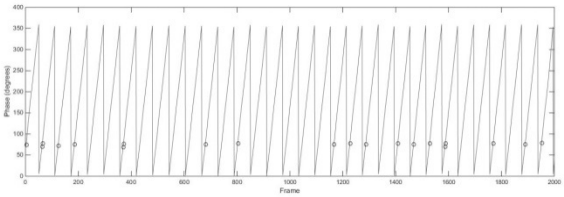

Fig. 8. Each frame is assigned a phase-value between 1 and 360, so at the end of each cycle the phase value returns to 1, producing this saw-tooth pattern. The phases of the frames with the highlighted center positions (Fig. 7) are indicated on the graph with circles, showing they all occur at the same stage in the cycle.

When the 36-frame time series of the cylinder is loaded into Paraview, the

cylinder's motion appears exactly as expected; the first mode is observed in both the crossflow and inline directions, as was observed visually and in the preliminary motion tracking data, and the frequency in the inline direction is roughly twice that in the crossflow direction. The wake data, despite only containing every tenth data point of the original data, proved to be not as convenient as a time series, with each frame taking minutes to load: additional efforts may be needed to produce a video visualization. Within Paraview, viewing the data as a "volume" seemed to be the most promising option, though also debilitatingly slow. Creating isosurfaces of vorticity data is another possibility, but only for scalars, so future tests with multiple-component vorticity vectors will need a different approach. For this, the "Glyph" mask will likely be the best option, since it is capable of reading vector components and representing their corresponding vectors visually.

DISCUSSION

Since this project was limited by time constraints, one difficulty with the final visualization was a lack of data points. For the vorticity fields of a significant number of slices to be processed in a timely fashion, only every tenth point in the x direction was processed; additionally, slices 7 to 17 only represent the center 10 centimeters of the cylinder. The cylinder being 25 cm long with images taken at 20 of those points, the current analysis does not provide nearly the whole picture.

For future visualizations, experiments should be conducted to ensure that the behavior of the cylinder during the data collection at each plane remains the same. Slice 9 in these experiments, for instance, presented an entirely different cycle of motion than other slices, and even the more similar orbitals had some differences. Many papers on VIV discuss the effects of hysteresis, in which changing or disturbing the flow speed between trials can result in certain non-reversible cycles (Sarpkaya 2004). Additionally, these methods should be tested with different flow speeds to determine whether the observed irregular motion is a result of 0.17 m/s being a transition point between cylinder modes or frequencies.

Future projects should also focus on calculating a 3D vorticity field from similarly assembled velocity fields, since this is one of the most important potential products of attempting such a visualization in the first place.

This project has confirmed that tracking the illuminated crescent provides accurate information on the motion of the cylinder, although a better method for finding the necessary shift to apply to the tracked point is a worthwhile goal. It is possible that this method could be used to track, in addition to the crescent, a virtual point created in ProAnalyst at the location of the cylinder's center. If an additional high-speed camera is available, however, it may be more fruitful to simply take images of the cylinder's crossflow motion and analyze these separately. One setback to this last suggestion, and the main reason this was not attempted here, is that all cameras would need to be completely synchronized so that the motion tracking and wake data line up with each other correctly.

Finally, the structure of the VTK file format caused some difficulties in making MATLAB analysis more efficient. A potentially faster approach than the one used here would be to write in the data of each slice to the file as it is calculated; given the VTK organization, it was instead necessary to save all data points for every slice and every phase before writing the files for visualization in Paraview.

Overall, the phase-averaging techniques attempted here have potential to be extremely useful in studying the properties of Vortex-Induced Vibrations, though many important details will need to be worked through before a viable procedure is produced.

ACKNOWLEDGMENTS

Thank you to the National Science Foundation for providing funding for this as a Research Experiences for Undergraduates project, to the URI Graduate School of Oceanography for hosting the SURFO REU program, and to Amin Mivehchi for his assistance with the Paraview software and the phase-averaging code.

REFERENCES

Gedikli, E., and J. Dahl. 2014. Mode shape variation for a low-mode number flexible ccylinder subject to vertex-induced vibrations. *ASME 33rd International Conference on Ocean, Offshore and Arctic Engineering*.

Griffin, O., and S. Ramberg. 1974. The vortex-street wakes of vibrating cylinders. J. Fluid Mech. 66: 553.

Matsuzaki, K., M. Shingai, Y. Haramoto, M. Munekata, and H. Ohba. 2004. Visualization of 3D flow structures in the wake of an inclined circular cylinder. J Vis 7: 309-316.

SARPKAYA, T. 2004. A critical review of the intrinsic nature of vortex-induced vibrations. Journal of Fluids and Structures 19: 389-447.

Willert, C., and M. Gharib. 1991. Digital particle image velocimetry. Experiments in Fluids 10, doi:10.1007/bf00190388

Williamson, C., and A. Roshko. 1988. Vortex formation in the wake of an oscillating cylinder. Journal of Fluids and Structures 2: 355-381.

Xu, J., M. He, and N. Bose. 2009. Vortex modes and vortex-induced vibration of a long, flexible riser. Ocean Engineering 36: 456-467.

E. Thomas is at the University of Massachusetts, Amherst, MA. (ethomas@umass.edu)
Deniz Gedikli (egedikli@uri.edu)
Jason Dahl (dahl@egr.uri.edu)

An analysis of winter-spring diatom bloom variability in Narrangansett Bay

Amanda Van Buskirk, Theodore J. Smayda, and David Borkman
Graduate School of Oceanography, University of Rhode Island, Narragansett, RI 02882

Abstract

The winter-spring (WS) diatom bloom is a dominant feature of the phytoplankton annual cycle in temperate coastal zones globally. The accumulation and subsequent fate (benthic deposition or pelagic grazing) of WS bloom phytoplankton have important implications for higher trophic levels. Variability in the timing and abundance of WS diatom bloom is evident in review of weekly Narragansett Bay phytoplankton observations. A 38-year time-series was analyzed to identify the start, peak, duration, and magnitude of the WS blooms from 1959-1997. All of the WS bloom characters were highly variable. Along with a complete matrix of the bloom descriptors, a corresponding dataset of temperature, irradiance, and nutrient levels (Si, NH_4, NO_3 and PO_4) was analyzed to find patterns and correlations between environmental factors and WS bloom timing and magnitude. Environmental data from early in the WS bloom season (November-December) were used to predict bloom characteristics for the upcoming year. Nov-Dec irradiance, surface temperature, surface NH_4 and Si concentrations all showed statistically significant linear relationships with one or more bloom characters. WS blooms of shorter duration occurred during warm years and the bloom tended to start earlier during years having greater Nov-Dec irradiance. Pre-bloom nutrient concentration was positively related to WS bloom duration, with greater bloom duration during years having greater pre-bloom PO_4 and NH_4 concentrations. Association of WS bloom pattern with environmental data suggests that a combination of regional (climate control via temperature and light) and local (nutrient concentration) impacts are driving WS bloom timing and magnitude.

The winter-spring (WS) diatom bloom is a yearly occurrence that is pivotal to the health and productivity of organisms in temperate coastal waters. Phytoplankton produce over 50% of the world's oxygen output, with ~25% of global O_2 production from marine diatoms (Round *et al.*, 1990), so diatom growth and abundance patterns have important effects on global biogeochemical cycles and species at higher trophic levels. In addition, the significance of phytoplankton blooms with respect to the carbon cycle has gained a growing appreciation. Due to the profound impact these blooms have on marine ecosystems, understanding the drivers of WS bloom variability and the response to environmental change is essential.

The timing and accumulation of WS phytoplankton blooms is thought to be affected by environmental factors such as temperature and light that may be influenced by climate change. It is known that coastal waters have gotten warmer over time (Belkin, 2009) and this warming is impacting phytoplankton productivity in coastal systems including Narragansett Bay (Oviatt, 2004, Nixon, 2009). Since the fate of marine systems is dependent on WS phytoplankton (Townsend *et al.*, 1994), it is fundamental to study the effects of temperature and other ecological influences on WS blooms. Mixed responses of WS

bloom timing and magnitude to warming have been documented. An earlier onset of the WS bloom has been reported in freshwater systems (Peeters *et al.*, 2007), but the WS bloom in the coastal North Sea off Helgoland has showed little change during a warming period over the past ~50 years (Wiltshire *et al*., 2008). However, bloom initiation, duration, termination and magnitude are variable from year to year, and there are relatively few long-term (multidecadal) quantitative phytoplankton abundance datasets available to analyze the specific drivers of WS bloom variability.

A multidecadal (beginning in January 1959 and ongoing) time series of weekly phytoplankton species composition and abundance is available for lower NBay (Smayda, 1998). NBay has been extensively studied in terms of phytoplankton as well as its ecological components (temperature, light, nutrient concentration), and this provides strong insight into what has been occurring in the Bay over time. The NBay phytoplankton time series has documented considerable variation for phytoplankton blooms (Smayda, 1984), but mechanisms driving that variability remain obscure. Whereas most studies have focused primarily on the responses of specific species of phytoplankton to environmental changes, our purpose is to analyze how centric diatoms as a phytoplankton functional group have varied in abundance and bloom timing during the winter-spring bloom period (November to April) and to identify environmental variables that may be driving that change.

METHODS

Study site and data – From January 1959 to May 1997, surface water samples were collected weekly at a long-term monitoring station located in the lower West Passage of NBay and analyzed for phytoplankton species composition and numerical abundance (Borkman and Smayda, 2009). Surface water samples were returned to the lab within 1 hour of collection and counted live using a 1-mL Sedgwick-Rafter counting chamber and Zeiss or Olympus microscopes equipped with phase contrast illumination. Phytoplankton were counted at 250X magnification and the entire 1-mL chamber was counted yielding a 1 cell mL^{-1} detection limit.

Water temperature, salinity, Secchi depth, nutrients (NH_4, NO_3, $Si(OH)_4$, PO_4), light and zooplankton species composition, numerical abundance and biomass were also determined. Records of local meteorological variables including wind speed and precipitation (monitored at T.F. Green Airport by NOAA, 1959 to 1997), and river flow (monitored at various gauging stations; USGS, 1959-1997) were also compiled (Smayda, 1998; Pilson (1991)). The North Atlantic Oscillation Index (NAOI) of Hurrell (1995) was used as an indicator of winter weather pattern.

Identifying bloom initiation – In order to determine when a winter-spring bloom begins, a suite of WS bloom descriptors was developed. A similar approach has been applied to describe long-term changes in the WS bloom in Lake Windermere (Maberly et al. 1994). A rate of change (ROC) metric was developed to identify periods of diatom population increase and decrease. Since phytoplankton grow exponentially, the rate of increase or decrease was calculated using the growth rate equation:

$$\mu = \left[\ln\left(\frac{M}{M_o}\right) * \left(\frac{1}{t * \ln(2)}\right)\right] \qquad (1)$$

where μ = growth rate in divisions per day, M = final abundance (at time t) in cells per mL, M_o = initial abundance (at time t) in cells per mL, and t = duration of

increase/decrease ($t-t_o$) in days. This method estimates the apparent rate of change of diatom abundance in doublings per day. Since the time series is recorded weekly, the term ($t-t_o$) was multiplied by seven to transform our duration of increase/decrease into days and yield an apparent population change rate in units of divisions per day.

Before this metric was used to determine bloom initiation, the bloom peak was identified for each year. Bloom peak is simply the week of the year in which diatom abundance is greatest. Once all of the peaks have been recorded, and the ROC has been calculated for each week, bloom initiation was determined. Starting at the peak, we worked backwards, monitoring the ROC, to identify where it became negative (or alternatively, where the greatest change in ROC occurred). The week in which this change in ROC took place therefore was identified as the bloom initiation week for that WS bloom season.

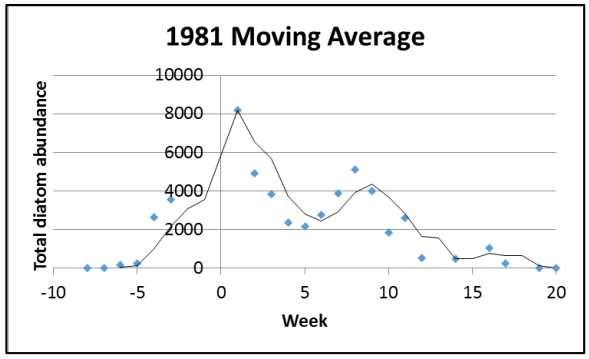

Fig. 1. Visual representation of the 3-period moving average for the year 1981 to illustrate WS bloom descriptors (initiation, peak, termination). Bloom initiation began in week -3 and bloom peak occurred in week 1. Bloom termination occurred in week 14, where the graph shows a steady decrease prior to that week and a subsequent leveling off afterwards.

Identifying bloom termination – Bloom termination was determined using a 3-week period moving average. This method took the weekly diatom abundance for each year and averaged a subset of three sets of abundances. A visual representation of the moving average was inspected to pinpoint the bloom termination week each year (Fig. 1). Once bloom initiation and termination were identified, bloom duration was calculated by subtracting the termination week by the initiation week. Abundances (i.e., abundance at bloom initiation, abundance at bloom peak and abundance at bloom termination) were recorded for each bloom character and all of the bloom descriptors were assembled into a matrix of 38 years (1959 to 1997) by 7 bloom characters.

Statistical Methods – Statistical analyses were carried out using JMP Pro 11 statistical software. Data were checked for the normal distribution prior to analysis. All bloom descriptors had normal distributions, with the exceptions of abundance criteria and rates of increase/decrease. Nov/Dec environmental factors all followed a normal distribution as well, with the exception of the amount of rainfall. Linear regression was used to find correlations between bloom characters and environmental factors as well as time and one another. Linear goodness of fit tests were run to identify significant relationships between the data.

RESULTS

Bloom variability – Bloom characters showed great variability (Table 1). There were no statistically significant relationships between bloom descriptors and time, suggesting that there were no trends in WS bloom characters during 1959-1997. The large range of weeks for bloom initiation, peak, termination and duration is evident (Fig. 2). “Big” and “small” bloom years, as well as “long” and “short” bloom years, are

not dependent on time. However, certain statistically significant relationships did occur between specific bloom characters. Bloom initiation, peak and termination all increased together, suggesting that later initiation weeks result in later peak and termination weeks. Furthermore, as these characters increased, bloom duration decreased, suggesting that, as bloom characters appear later in the season, a shorter overall bloom duration follows, i.e., blooms that started and peaked later were of shorter duration.

Table 1. Descriptive statistics for WS bloom characters in Narragansett Bay (1959-1997).

Bloom trait	Min	Max	Median	Mean
Initiation (week)	-5	17	3	4
Peak (week)	1	19	8	7.7
Termination (week)	7	20	13	13.0
Duration (weeks)	3	17	10	9.0
Peak abundance (cells mL^{-1})	2,142	101,391	13,511	19,468
Abundance at initiation (cells mL^{-1})	25	10,529	1,004	2,299
Abundance at termination (cells mL^{-1})	55	15,419	813	1,641

Bloom descriptors and environmental factors – Environmental factors were tested separately to find trends occurring over time. The only statistically significant trend over 1959-1997 occurred with temperature (p-value=0.0001). Average weekly temperature for week 44 to week 20 (the WS bloom period) increased over the 38-year period, specifically by 0.04°C per year (r^2=0.435). A 2°C temperature difference in mean WS bloom (November – April) temperature is evident between 1959 and 1997. To inspect this trend further, the temperature data and the corresponding diatom abundance data were separated into "warm" and "cold" years. Warm years were categorized as the top 25% of the WS temperature data and cold years were categorized as the bottom 25%. Total diatom abundance was averaged for each week for both warm and cold years to identify similarities and differences between the two clusters of years (Fig. 3). The results show how diatom abundance was much greater during cold years (mean = 4763 cells mL^{-1}), (t-stat=-3.42, df=38, p value=0.0015) as opposed to that observed during warm years (mean = 1971 cells mL^{-1}), suggesting that temperature influenced bloom variability with increased WS bloom centric diatom abundance during cold years.

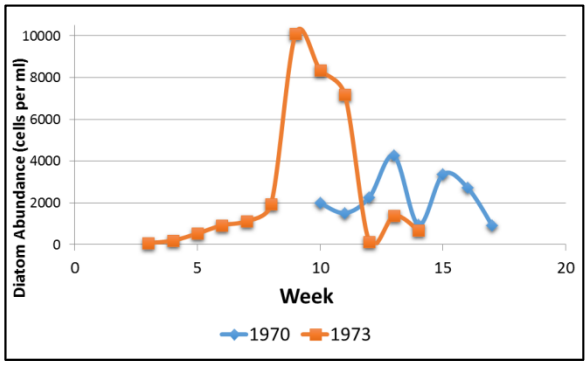

Fig. 2. Bloom variability for years 1970 and 1973. Year 1970 represents a relatively short WS bloom duration with a small peak and later initiation week. Year 1973 represents a relatively long WS bloom duration with a large peak and earlier initiation week.

No other such relationships existed between bloom characters and other environmental factors and/or time. Whereas temperature data provided insight into the variability of bloom characters, other approaches would be necessary to determine how the phytoplankton are responding to the changing Bay.

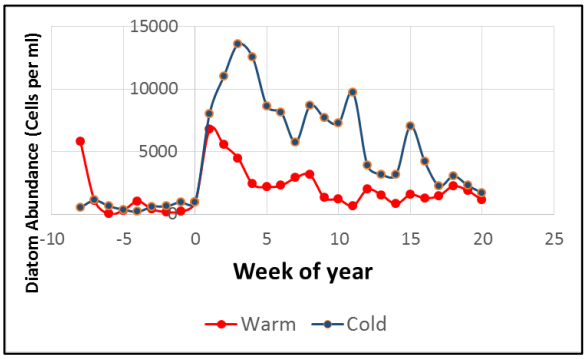

Fig. 3. Weekly averages of the total diatom abundances for warm versus cold years.

Table 2. Significant relationships between Nov/Dec environmental factors and bloom characters.

X	Y	Slope	r^2	p-value
Irradiance	Bloom duration (weeks)	+0.15	0.14	0.0402
Irradiance	Bloom peak week	-0.29	0.24	0.0060
Irradiance	Bloom start (week)	-0.27	0.19	0.0173
NAOI	Abundance at peak	-7,435	0.23	0.0076
NAOI	Abundance at end	-971.5	0.24	0.0063
NH_4	Bloom duration (weeks)	+1.17	0.46	0.0038
Si	Abundance at end	+220.7	0.35	0.0037
Surface Temp	Bloom duration (weeks)	-1.75	0.26	0.0055

Pre-bloom nutrients vs. bloom characters – We examined how pre-bloom nutrient concentrations could be used as a predictor for future bloom characters. Pre-bloom nutrient concentration was calculated by averaging nutrient levels for the two weeks prior to the bloom initiation week each year. We found that as surface PO_4 and NH_4 increased, bloom initiation began earlier (p-values=0.0010 and 0.0456, respectively). Furthermore, as surface PO_4 and Si increased, these earlier blooms tended to have earlier termination (p-values=0.0374 and 0.0059, respectively); early initiation blooms also tended to end early. However, bloom duration was longer as pre-bloom PO_4 and NH_4 increased (p-values=0.0224 and 0.0178, respectively). That is, WS blooms began earlier and were of longer duration during years having elevated PO_4 and NH_4 concentration. These results suggest that, as pre-bloom nutrient levels increase, WS blooms start earlier and have longer duration.

Nov/Dec environmental variables as WS bloom predictors – NBay diatom abundance has great variation, and a key factor in understanding this variation is to use previous data to predict future bloom characters. We specifically looked at the relationships between environmental data from early in the WS bloom period (November and December, (Nov/Dec)) of each year and WS bloom characters to predict what the WS bloom would look like for the upcoming year. Our results yielded five statistically significant predictors of WS bloom behavior: surface temperature, irradiance, NAOI, surface NH_4, and surface Si concentrations (Table 2; Fig. 4).

While the WS bloom characters were highly variable, several trends were evident. Years in which the Bay was colder tended to result in a WS bloom of larger magnitude and longer duration (1960s and 1970s) compared to warmer years (1980s and 1990s). Early season environmental predictors were related to WS bloom timing and magnitude, with the bloom starting earlier and lasting longer during years that were colder and brighter. When the NAOI was positive (the Northeastern United States having a warmer winter), the total diatom abundance at the peak and end of a bloom tended to be reduced. An increase in nutrient levels (surface NH_4 and Si) correlated with

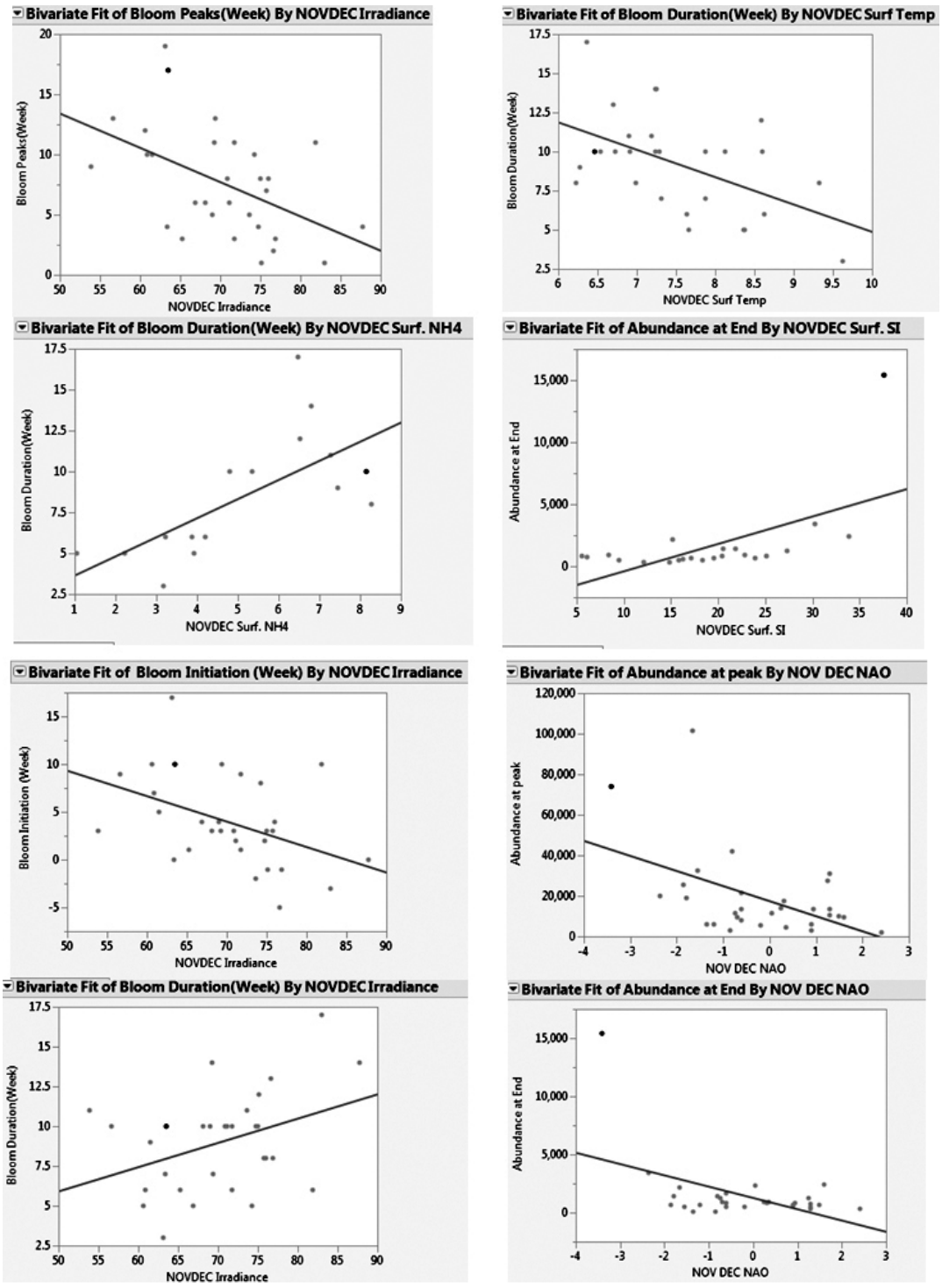

Fig. 4. Significant linear relationships between five environmental variables and WS bloom characters. Linear regression statistics in Table 2.

the bloom having a longer duration and increased diatom abundance at the end of the bloom. Increased pre-bloom nutrient concentration correlated with the WS bloom starting and peaking earlier and lasting longer.

DISCUSSION

The timing and abundance of the WS bloom in NBay is naturally variable, and since no specific technique has been developed to exactly calculate bloom characters, they are difficult to determine. However, the environmental factors that drive phytoplankton variability are well known (Townsend *et al.* 1994). Surface temperature has been increasing in the Bay (Oviatt 2004, Nixon 2009), and diatom abundance has been reduced, suggesting that the diatoms achieve greater abundance during colder winters. When predicting future WS bloom behavior, no strong correlations could be found between Nov/Dec environmental variables and bloom characters (all r^2 values were below 0.5). Despite five variables having significant relationships with one or more bloom characters, we are still unable to find any strong predictors of WS bloom behavior due to the lack of a strong goodness of fit.

While our results lack strong correlations, they do provide insight into how the changing Bay is affecting phytoplankton growth and abundance. We see a combination of regional (surface temperature, irradiance, and NAOI) and local (NH_4 and Si concentrations) control happening with the Nov/Dec environmental variables. Moreover, variability in WS bloom characters and lack of strong predictors are similar to the findings of Wilshire et al. (2008). Their study at Helgoland revealed that bloom variability was mainly dependent on temperature, however, no strong changes in WS bloom characters were found despite the vast environmental changes over time. Our data yielded comparable results, with temperature being one of the stronger predictors but overall failing to strongly identify outside influences to WS bloom behavior.

Pre-bloom nutrient levels (PO_4, NH_4 and Si) all contributed to the timing of the oncoming WS bloom. While these correlations are not strong, they are significant, and provide an understanding of how nutrients play a role in determining how a WS bloom will behave. Martin (1965) described how nutrient regeneration by zooplankton in NBay during the fall of each year contributes to the success of the WS bloom, and our results reflect these findings. The Nov/Dec nutrient levels correlate with these findings as well; surface NH_4 and Si concentrations showed significant positive relationships with certain bloom characters. For example, WS bloom duration increased by approximately one week for every 1 μMol increase in pre-bloom ammonium concentration (Table 2). Our study agrees with similar works in terms of determining environmental changes and possible effects on phytoplankton, but fails to pinpoint exactly how or why the WS bloom is so variable, and further study is needed to resolve this ongoing issue.

Only linear models used to find correlations among our data are presented here. Whereas linear models did not fit the data as strongly as we would like, no other models (exponential, logarithmic, etc.) provided any stronger fit. The data were too variable to be properly modeled by any goodness of fit line. Linear goodness of fit was chosen because it most clearly showed any increasing or decreasing trends happening over time or between two variables.

A probable explanation for the lack of strong findings is the fact that the study focused primarily on centric diatoms as a group instead of individual species. The centric diatoms present in NBay during the WS bloom period consist of hundreds of species (Hargraves, 1988), with only a few key species making up most of the community (Karentz and Smayda, 1984;

1998). When looking at a single species-complex, such as *Skeletonema* spp. in NBay, stronger patterns and predictors were found (Borkman and Smayda, 2009). A clear steady then declining trend of the species was observed over time and a negative influence of the NAOI and of increasing water temperature on winter-spring *Skeletonema* abundance was identified. *Thalassiosira nordenskioeldii*, another dominant winter-spring species, was also studied closely and showed an increased winter-spring abundance in colder winter-spring years (Davis, 2013). When grouping all of the species together, it is much more difficult to pinpoint what is driving the change of the community as a whole because individual species may be changing and reacting to environmental forces differently. That is, interspecific compensation may be occurring, with one species increasing to fill the winter-spring niche vacated by species on the decline. A possible alternative to resolve the issue could be to study the main species that make up the community separately and compare the findings of each species to one another to see if there are any similarities in their behavior or how they respond to their environment.

This study allowed us to further understand how diatoms in NBay behave and how they might be responding to their changing environment. The WS bloom is extremely variable, and the exact factors that drive this variability are still not well known. However, despite the lack of strong results, the observed patterns happening to the diatoms and the environmental variables over time allow for some possible future predictions. Due to the effects of temperature on centric diatoms that dominate the winter-spring diatoms phytoplankton community and how bloom characters correlate with one another, we could expect later bloom initiation and later bloom peaks, as well as shorter bloom durations and reduced abundances in response to warming coastal waters globally.

REFERENCES

Belkin, I.M. 2009. Rapid warming of Large Marine Ecosystems. Progress in Oceanography 81 207–213.

Borkman, D.G and Smayda, T.J. 2009. Multidecadal (1959–1997) changes in *Skeletonema* abundance and seasonal bloom patterns in Narragansett Bay, Rhode Island, USA. Journal of Sea Research 61 84–94.

Davis, M. 2013. Long-term bloom patterns of the diatom *Thalassiosira nordenskioeldii* Cleve in Narragansett Bay. 2013. Talk authored by M. Davis, D. Borkman and T. Smayda. Presented by M. Davis at the Association for the Sciences of Limnology and Oceanography National Meeting, New Orleans, LA 17-22 February 2013.

Hargraves, P.E. 1988. Phytoplankton of Narragansett Bay. In: R.G. Sheath and M.M. Harlin (Eds.), Freshwater and Marine Plants of Rhode Island, pp.136-142.

Hurrell, J.W. 1995. Decadal trends in the North Atlantic Oscillation: Regional temperatures and precipitation. Science 269: 676-679.

Karentz, D. & T.J Smayda. 1984. Temperature and seasonal occurrence patterns of 30 dominant phytoplankton species in Narragansett Bay over a 22-year period (1959-1980). Mar. Ecol. Progr. Ser. 18: 277-293.

Karentz, D. & T.J. Smayda. 1998. Temporal patterns and variations in phytoplankton community organization and abundance in Narragansett Bay during 1959 - 1980. J. Plankton Res. 20:145-168.

Maberly, S.C., M.A. Hurley, C. Butterwick. J.E. Corry, S.I. Heaney, A.E. Irish,

G.H.M. Jaworski, J.W.G. Lund, C.S. Reynolds and J.V. Roscoe. 1994. The rise and fall of *Asterionella formosa* in the south basin of Windermere: an analysis of a 45-year series of data. Freshwater. Biol. 31: 19-34

Martin, J.H. 1965. Phytoplankton-zooplankton relationships in Narragansett Bay. Limnol. Oceanogr. 10 (2): 185-191.

Nixon, S.W., Fulweiler, R.W., Buckley, B.A., Granger, S.L., Nowicki, B.L. and Henry, K.M. 2009. The impact of changing climate on phenology, productivity, and benthic–pelagic coupling in Narragansett Bay. Estuarine, Coastal and Shelf Science 82: 1-18.

Oviatt, C.A. 2004. The changing ecology of temperate coastal waters during a warming trend. Estuaries 27: 895-904.

Peeters, F., Straile, D, Lorke, A. Livingstone, DM. 2007. Earlier onset of the spring phytoplankton bloom in lakes of the temperate zone in a warmer climate. Global Change Biology 13: 1898-1909.

Pilson, M.E.Q. 1991. Aspects of climate around Narragansett Bay. Narragansett Bay Project Report # NBP-91-64. 29 pages plus appendices.

Round, F.E., R.M. Crawford and D.G. Mann. 1990. The Diatoms: Biology and Morphology of the Genera. Cambridge University Press. 747 pp

Smayda, T. J. 1984. Variations and long-term changes in Narragansett Bay: a phytoplankton-based coastal marine ecosystem: relevance to field monitoring for pollution assessment. In: White, H. H. (ed.), Concepts in marine pollution measurements. Univ. Maryland Sea Grant Publ., College Park, MD: 663-679.

Smayda, T.J. 1998. Patterns of variability characterizing marine phytoplankton, with examples from Narragansett Bay. ICES J. Mar. Sci. 55:562-573.

Townsend, D.W., Cammen, L.M., Holligan, P.M., Campbell, D.E., and Pettigrew, N.R. 1994. Causes and consequences of variability in the timing of spring phytoplankton blooms. Deep Sea Research I. 41: 747-756.

Wiltshire, K.H and 7 co-authors. 2008. Resilience of North Sea phytoplankton spring bloom dynamics: An analysis of long-term data at Helgoland Roads. Limnol. Oceanogr. 53: 1294-1302.

A. Van Buskirk is in the Department of Mathematics, Monmouth University, NJ (vnamanda@aol.com)
T. J. Smayda (tsmayda@uri.edu)
D. Borkman (dborkman@uri.edu)